Reactivity of crystalline slag phases in cementitious systems

by

Brian Traynor

B.A. Nanoscience, Physics and Chemistry of Advanced Materials
Trinity College Dublin, 2016

Submitted to the Department of Materials Science and Engineering
in partial fulfillment of the requirements for the degree of

Doctor of Philosophy in Materials Science and Engineering

at the

MASSACHUSETTS INSTITUTE OF TECHNOLOGY

September 2021

Author .....
Department of Materials Science and Engineering
July 20, 2021

Certified by .....
Elsa A. Olivetti
Associate Professor
Thesis Supervisor

Accepted by .....
Frances M. Ross
Chairperson, Department Committee on Graduate Studies

Reactivity of crystalline slag phases in cementitious systems

by

Brian Traynor

Submitted to the Department of Materials Science and Engineering
on July 20, 2021, in partial fulfillment of the
requirements for the degree of
Doctor of Philosophy in Materials Science and Engineering

Abstract

Portland cement manufacturing is thought to account for as much as 4-8% of global CO_2 emissions. Efforts to incorporate industrial wastes into concrete in order to offset the environmental burden of traditional cements have been growing in recent years. Reactive industrial wastes such as blast furnace slag and fly ash have been the subject of much research and have been successfully implemented in blended cements as partial replacements for Portland cement. Other wastes, such as steel and copper slags, have been largely neglected due to their lower reactivity. Concurrent with efforts at incorporating industrial wastes into concrete has been the development of alternative concretes with different chemistries, e.g. alkali-activated materials, blended Portland cements, and calcium sulfo-aluminate cements. This thesis focuses on improving our understanding of how the constituent phases of steel and copper slags interact with the aqueous phase of concrete, with the goal of identifying suitable applications in concrete. The focus on the constituent phases is recognition of the fact that steel and copper slags are too variable in composition to study on a case-by-case basis, and only through studies of their constituent phases can we identify opportunities for their use. First, I quantify the effect of aqueous chemical environment on the dissolution rate of the minerals calcio-olivine and fayalite, identified as primary phases of ladle furnace steel slag and copper slag, respectively. Calcio-olivine and fayalite were exposed to solutions of NaOH and $Ca(OH)_2$, chosen to mimic the pore solutions of alkali-activated and Portland-cement based binders. These results have significance for incorporating high olivine content steel and copper slags in concrete. Second, I elucidate the effect of aggregate surface chemistry on the type, morphology, and rate of reaction product formation in Portland cement-type systems. Polished surfaces of limestone, quartz, fayalite, and diopside were exposed to Ca and Si rich solutions and the resultant reaction products were characterized using scanning electron microscopy. The results of this study indicate that calcium silicate hydrate (the dominant reaction product of Portland cement concretes) nucleation and growth kinetics are accelerated on limestone surfaces relative to quartz, fayalite, and diopside surfaces, although no differences in the morphology of the precipitated C-S-H is observed. The relevance of this research is in the importance of the type and kinetics of reaction product for-

mation on the surface of an aggregate, which plays a crucial role in the development of hardened, load-bearing concrete. This experimental research is supplemented by extensive literature review of the composition and microstructure of steel and copper slags, as well as the dissolution rates and thermodynamics of dissolution in concrete pore solution of the relevant steel and copper slag phases. This work serves to contextualize the previous experimental research and to contribute towards the development of a kinetic model that accounts for the reaction kinetics of both Portland cement and crystalline slags (steel or copper slag). This thesis also presents a methodology for calibrating pH meters in highly alkaline solutions such as those relevant to cementitious systems.

Thesis Supervisor: Elsa A. Olivetti
Title: Associate Professor

Acknowledgments

To my advisor, Elsa, I owe a huge debt of gratitude. You have been the best advisor I could possibly have asked for and I will sorely miss working with you. Thank you for all of your sage advice, guidance, and patience over the years.

I would like to also thank my committee, Prof Antoine Allanore and Prof Shuhei Ono, for the hours they have spent listening to and reading about my research. I have huge respect for you both and value your expertise.

To my fellow brick mafioso, thank you for all the memories over the last 5 years. Thank you to Tuna, Hugo, and Piyush for the countless hours spent together in the lab and the office. Each of you made my research better and my days on campus more enjoyable. The last year of pandemic induced separation has really made me realize how much I valued you all. Thanks are also due to our UROPs for contributing to my research and for making me less cynical with your wide-eyed enthusiasm — thanks to Chris Eschler, Spencer Hu, and Ciara Mulcahy.

To the other members of the Olivetti group both past and present, thank you for all being such clever, inquisitive, curious, and thoroughly pleasant people. I really enjoyed the time I spent with you.

My research was greatly helped by all of the great technical staff who have been always been so generous with their time. In the Materials Research Laboratory, this includes Shiahn Chen, Patrick Boisvert, Charlie Settens, Tim McClure, and Libby Shaw. In the METLAB, I thank Shaymus Hudson for the many hours spent teaching me and fixing equipment I had broken.

For 4 out of my 5 years at MIT I lived with Richard Park and Edward Pang. Both have inspired me in very different ways with their distinct approaches to life and work. You have to live with them to understand.

To my family, thank you for your support the last 5 years. You are always there for me and I love you all.

And finally, to my finacée Mary, you have done more than anyone to support and motivate me the last 5 years. Thank you for always being my partner and teammate.

Contents

List of Figures

List of Tables

Chapter 1

Introduction

This chapter provides background on concrete and the chemistry of both incumbent and alternative cements. The properties of steel and copper slags are then discussed - the application of these materials in concrete is the basis for this thesis. The challenges associated with the application of steel and copper slags in building materials are then described. This chapter concludes by identifying of how this thesis serves to address those challenges, and the specific research questions which are tackled later in the thesis.

1.1 Concrete and its chemistry

Concrete has a long history as one of humanity's most important technological innovations. Modern cement manufacturing was born in 1824 when Joseph Aspdin took out a patent for Portland cement – so called because of its resemblance to Portland stone used on building facades of the time. Further improvements by his son, William Aspdin, who recognized the critical role of calcination temperature on reactivity, cemented his place as the inventor of "modern" Portland cement (PC). Optimization of processing conditions and feedstocks over the intervening years has not substantially changed the fundamental reaction processes. Initially, limestone ($CaCO_3$) is transformed into lime (CaO) and carbon dioxide (CO_2) through calcination at 1450°C in a kiln. The presence of siliceous clays in the kiln results in the formation of calcium

silicates, primarily alite (C_3S) [1] and belite (C_2S). Finally, gypsum ($C\bar{S}H_2$) is added to the cement to control setting time of the concrete. Upon mixing with aggregate and water, the reaction of the cement with water (a process is known as cement hydration) results in a complex series of reactions that harden the composite over time, endowing concrete with strength. Calcium silicate hydrate (C-S-H), the primary reaction product of the cement, is the 'glue' that binds together the aggregates of the concrete to provide good compressive strength. C-S-H is a poorly defined, amorphous, gel-like reaction product with a Ca/Si ratio of anywhere between 0.7 and 2.3. The basic molecular building block of the C-S-H phase is the linear silicate dreierketten unit, which has a repeating unit of three silica tetrahedra, with every third tetrahedra being kinked. C-S-H forms a layered structure, with a layer consisting of calcium oxide sandwiched by chains of dreierketten units forming silicate chains.

The global average CO_2 emissions per ton of cement manufactured is estimated to be anywhere from 0.6 - 1 tons [12]. When used to manufacture concrete, the presence of aggregates and water – which have low associated CO_2 emissions – dilutes the CO_2 emissions per ton of concrete by a factor of 5-10. Thus, concrete is a relatively low-CO_2 construction material, at least in comparison to the production of another widely used construction material, steel about 3 tons of CO_2 emitted per ton of steel produced [13]. However, the sheer scale of concrete manufacturing and its growing demand in developing countries means its production is thought to account for as much as 4-8% of global CO_2 emission (Figure 1-1).

Cement production has been identified as a sector in which wide-scale reductions in greenhouse gas emissions will be difficult to achieve due to existing economies of scale [1]. An analysis by the United Nations Environment Program Sustainable Building and Climate Initiative concluded that increased use of supplementary cementitious materials (SCMs) as replacement for Portland cement clinker and more efficient use of Portland cement clinker in concretes represent the best strategies for reduction of CO_2 emissions [14]. Providing a sufficient supply of SCMs to the cement industry

[1] C_3S is here expressed in cement notation, where C=CaO, S=SiO_2, H=H_2O, A=Al_2O_3, F=Fe_2O_3, c=CO_3, M=MgO, $\bar{S}$=SO_3, K=K_2O, and N = N_2O

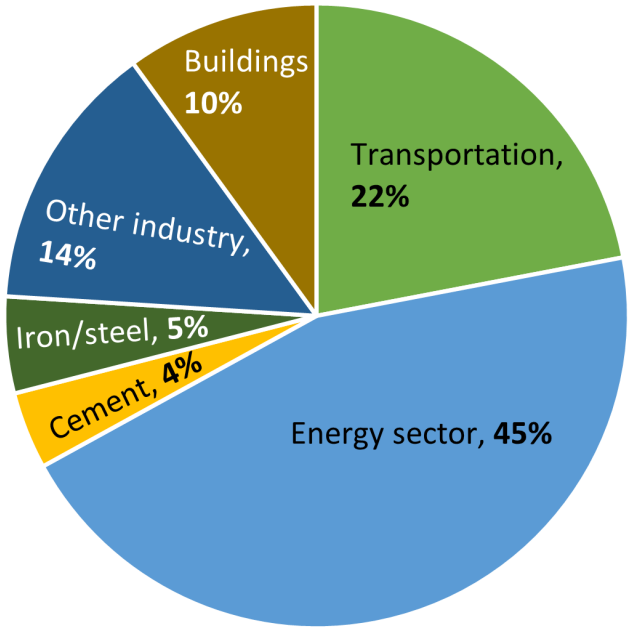

Figure 1-1: Global CO_2 emissions by sector. Adapted from [1].

is a challenge as the traditionally used SCMs, fly ash and blast furnace slag, are either well-used [15] or have threatened supply chains [16]. The range of potential SCMs has been broadened by the research community to meet this growing demand, encompassing calcined clays, biomass ashes, steel slags, non-ferrous slags, and bauxite residues.

Partial replacement of Portland cement with SCMs results in a blended Portland cement. The most commonly used SCMs — blast furnace slag, fly ash, and calcined clay — all have high alumina content. Hydration of blended Portland cements results in a modified main reaction product - an aluminum substituted C-A-S-H type gel with a disordered tobermorite-like C-S-H structure [17]. Complete replacement of Portland cement with SCMs is also possible and has been demonstrated by alkali-activation of blast furnace slag, fly ash, and calcined clay. These cements are known as alkali-activated materials (AAMs) or geopolymers. Precursors deficient in calcium but rich in silica and alumina are more reactive in aqueous alkaline environments and react to form highly disordered, highly crosslinked aluminosilicate gels known as N/K-A-S-(H). Alkali-activation relies on the fact that the dissolution rate of aluminosilicates generally increases with increasing pH, which would otherwise be too slow to be useful

in concrete. Comparisons between the structure of geopolymers and zeolites have been made noted in numerous publications [18, 19] — zeolites are aluminosilicate minerals composed of a dense 3-dimensional network of alumina and silica tetrahedrons with loosely bound alkali cations charge balancing the AlO^{4+} in tetrahedral coordination [20]. Another promising set of binders are based on calcium sulfo-aluminate cements. In calcium sulfo-aluminate cements, precursor phases such as ye'elemite ($C_4A_3\bar{S}$), C_4AF, and C_2S react to form monosulfate ($C_3A.CS.12H$), ettringite ($C_3A.3C\bar{S}.32H$), and strätlingite (C_2ASH_8) reaction products. Empirical determinations of the amount of reactive sulfate that results in the optimum mortar strength have been developed [21]. These binders are promising due to their lower embodied energy relative to Portland cement based binders.

It is worth noting that there are no specific hard delineations among what is called Portland cement, blended Portland cement, alkali-activated material, geopolymers, or calcium sulfo-aluminate cements. These terms represent points along a continuum of cements whose chemistry varies from the Ca and Si rich composition of Portland cements, to the Na, Al, Si rich composition of geopolymers. For example, C-S-H, N-A-S-H and C-(N-)A-S-H gels may coexist as reaction products in the presence of both a calcium source and an aluminosilicate source in alkaline medium. This concept is depicted in Figure 1-2, in which precursors and reaction products are represented within a SiO_2, CaO, Al_2O_3 ternary phase diagram.

This thesis is focused on using steel and copper slags in building materials for 2 reasons: they are replete with crystalline phases whose composition makes them good candidates for cementitious systems; and they are currently produced in large quantities but with only sporadic existing use.

1.2 Metallurgical wastes

As described above, steel slag and copper slag are produced in large volume but have minimal existing use as SCMs [22]. Steel and copper slags are produced in massive and increasing quantities; steel slag production is estimated to be equal to 10-15% of

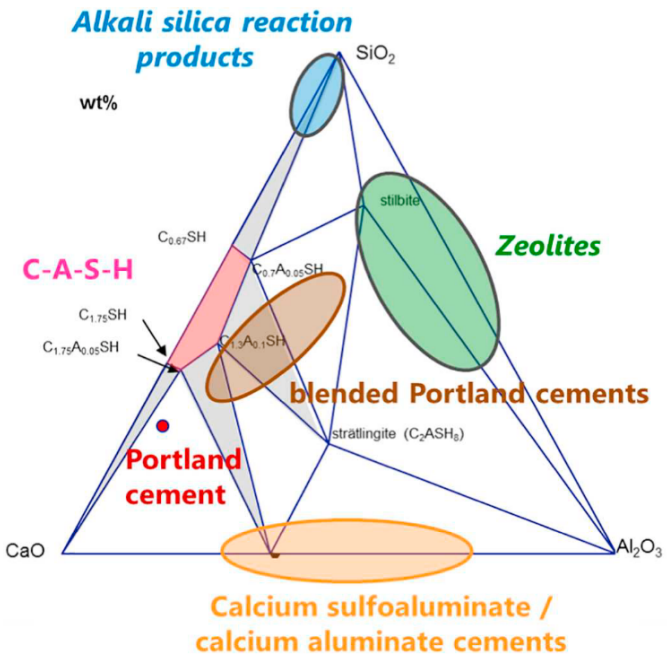

Figure 1-2: Ternary phase diagram depicting the chemistry of the precursors and reaction products of different cements. The underlying phases are reaction products, while precursors are overlaid. Adapted from [2].

total steel production, putting global steel slag production at 190-290 million metric tons in 2018 [23], while global copper slag production is 35-40 million metric tons in 2018 [24] (based on 2.2-2.5 tons of copper slag for every ton of copper [25, 26]). The scale of global steel and copper slag production has prompted research efforts aimed at identifying suitable concretes in which to use these materials.

1.2.1 Steel slag

The properties of steel slag vary depending on the steel-making process. There are 3 main classes of steel slag; basic oxygen furnace slag, electric arc furnace slag, and ladle furnace slag. Basic oxygen furnaces (BOF), also known as Linz-Donawitz (LD) furnaces, and variations on BOF furnaces account for 72% of global crude steel production [27]. The BOF takes primarily molten iron as its input, with a minority of steel scrap. The oxides CaO, MgO, FeO, and SiO_2 typically account for 90% of BOF slag composition. β-C_2S, dicalcium ferrite, RO phase, and lime are most commonly reported in BOF slag. Electric arc furnace (EAF) slag accounts for 28% of global

crude steel production [27]. The EAF typically takes steel scrap as its primary input. The higher variability in the composition of the inputs to the EAF translates to slags with higher compositional variability compared to BOF slags. Ladle furnace (LF) slags are used to produce steel alloys and take steel from BOFs or EAFs as input. Due to the wide variation in the composition of steel alloys, slags from LFs are highly variable in their composition. The physical and chemical properties of LFS, as well as its applications in construction materials, have been reviewed, and interested readers are referred to [28]. LFS has been identified as weakly cementitious when used in Portland cement based concretes or blended with blast furnace slag [29, 30]. Alkali activation of LFS has also been investigated, where increases in activator concentration resulted in mortars with higher compressive strength [31, 32].

The most commonly cited challenge associated with the use of steel slag in concrete is the reaction of free-CaO or free-MgO in BOF slags. The reaction of free-CaO or free-MgO with water to produce hydroxides causes volume expansion and loss of strength in the concrete. The free-CaO content of BOF slag used in asphalt is limited to a maximum of 4% in Germany for this reason [33]. In China, similar limits exist on the maximum allowed expansion of the slag due to the reaction of free-CaO [34]. Weathering of slags allows the conversion of free-CaO and free-MgO to their respective hydroxides prior to their application in concrete [33]. However, there are drawbacks to this pre-treatment: weathering takes time, particularly for the hydration of MgO; weathering requires storage space; and weathering may allow heavy metals present in the slag to leach into the groundwater. The free-CaO and free-MgO content may also be reduced through treatment of the molten slag in a separate slag pot. This process involves maintaining the slag in its molten state after its removal from the furnace and introducing additional oxygen and dry sand to chemically bind the free-CaO and free-MgO [35]. Another method for removing free lime involves heating the slag to 1673 K in air [36]. This results in the oxidation of wüstite to hematite, which in turn reacts with free-CaO to precipitate brownmillerite ($Ca_2Fe_2O_5$). Heavy metal leaching should also be considered with regard to the use of steel slags in concrete. The concentration of heavy metals in the slag is highly

dependent on the type of steel being produced during formation of the slag. For example, stainless steel LF slags contain higher concentrations of Cr than BOF or EAF slags. However, Proctor et al. tested the extent of toxic metal leaching of 58 slags from steel mills throughout the US and concluded that none of the slag types (blast furnace slag, BOF, and EAF) are hazardous, as defined by the USEPA [37]. A review of slag leaching data, performed by Piatak et al., identified As, Cr, and Mn from steel slag and As, Co, Cr, Cu, Pb, and Zn from copper slag as elements of environmental concern [38]. Leaching of these elements from their respective slags results in their concentrations commonly exceeding the maximum allowable USEPA soil screening levels. However, the encapsulation of slag in concrete inhibits mass transfer of toxic metals from the slag to the environment. Roslan et al. demonstrated that EAF may be effectively stabilized in concrete and observed concentration of leached metals are within acceptable limits [39]. Given the differences environmental standards from jurisdiction to jurisdiction, variability in slag composition, and the uncertainty in the extent to which a slag is encapsulated in concrete, there is a considerable range in assessing the toxicity of a given slag.

1.2.2 Copper slag

The production of copper slag involves two processes which produce slag as a byproduct; matte smelting and converting. Slags from both processes are typically rich in FeO, SiO_2, Fe_2O_3 with minor quantities of Al_2O_3, CaO, and MgO [38]. The dominant reaction during the smelting phase is the formation of fayalite (Fe_2SiO_4) due to the reaction of FeO with SiO_2. Slags with high SiO_2 content are acidic and highly viscous. An acidic slag makes the removal of acidic impurities (As_2O_3, Bi_2O_3, Sb_2O_3) more difficult and higher viscosity makes handling of the slag more challenging. Additionally, the formation of magnetite - through the reaction of FeO with Fe_2O_3 - can hinder the slag formation process. For these reasons, the introduction of the basic oxide CaO can be used to: reduce the acidity of the slag, thereby ameliorating the removal of impurities; lower the viscosity of the molten slag; and disfavor the formation of magnetite in favor of calcium ferrite. However, SiO_2 solubility is lower in

$CaO\text{-}FeO_x$ slags, and calcium ferrite slags corrode the refractories typically used in copper smelting furnaces. In practice, slags may be: acidic, silica-rich, and fayalitic; basic, calcium ferritic; or a balance between the two [40].

The type of slag depends on the type of furnace used during matte smelting and converting. Historically, copper matte smelting was achieved using blast furnaces and reverberatory furnaces, although these have been largely supplanted by newer technologies, such as the flash furnace. Flash furnace smelting accounts for about half of copper matte production. An SiO_2/Fe mass ratio of 0.7-1.0 is typically used through control of the quantities of flux used [41]. Copper matte is also produced via the Ausmelt and Isasmelt processes [42]. The quantity of magnetite in the molten slag during these processes is important and is typically around 5 wt% of the total slag. Finally, submerged Tuyere furnaces, variations of which include Noranda, Teniente, and Vanyukov, produce an estimated 15% of copper matte. The SiO_2/Fe ratio in the submerged Tuyere slags is typically 0.65, which results in a magnetite content of 15-20% [43]. Regardless of the type of furnace used, slags from copper matte smelting are predominantly composed of iron silicates – fayalite or fayalitic glass – with lesser quantities of magnetite. Copper matte is converted to blister copper most commonly in Peirce-Smith converters. In Peirce-Smith convertors, SiO_2/Fe slag ratios of 0.5 are desirable, corresponding to magnetite quantities of 12-18%. More recent converting technologies include Noranda converting and flash converting. Noranda slags are SiO_2-rich fayalitic slags and flash converting slags are more basic, calcium ferrite slags [44]. Calcium ferrite slags are found only in flash convertors and in Mitsubishi continuous converting furnaces.

The properties and utilization of copper slag have been reviewed before and interested readers are referred to [25, 45, 46]. In general, copper slag is characterized as an inert material with good performance as an aggregate with little to no cementitious properties [45]. Much research into copper slag usage has centered around its use as a fine aggregate replacement, with studies generally observing improved technical performance at low replacement [47, 48, 49]. Efforts have been made to chemically activate copper slags in the same manner as has been successfully implemented for

fly ash and blast furnace slag, although with limited success [50, 51]. Studies using amorphous copper slags have reported the synthesis of load-bearing inorganic polymers formed with the aid of an activating solution [52, 53].

1.2.3 Challenges with crystalline slag use

There are 2 major challenges associated with incorporating alternative precursors like steel and copper slags into building materials.

The first challenge of using crystalline slags in building materials is the effect the slag has on the kinetics of cement hydration. The kinetics of cement hydration is a key aspect of the formation of an initially flowable, but ultimately hardened concrete. Slow cement hydration will result in a concrete that takes to long to reach the prescribed strength, while rapid cement hydration formation prevents the pouring and settling of fresh concrete. In designing concretes which use alternative precursors or SCMs, the cement hydration kinetics are necessarily different from the incumbent system and understanding these differences is crucial to ensure the desired concrete properties are achieved. The relevant processes involved in cement hydration are precursor dissolution, mass transport of ions through aqueous or solid phases, and nucleation and growth of reaction products. Given the high number of phases in cementitious precursors, the high number of potential reaction products, and the simultaneous progression of each of the aforementioned processes, it is unsurprising that models of cement hydration kinetics are highly simplified descriptions of real systems. The presence of a crystalline slag affects 2 of these processes; precursor dissolution and the nucleation and growth of reaction products. A common assumption in cement hydration models is that dissolution kinetics are not the rate limiting step - nucleation and growth of reaction products or mass transport of ions away from a dissolving surface are usually assumed to be rate limiting [54]. However, many of the phases present are expected to dissolve much slower than the phases in incumbent cements, meaning that dissolution may be the rate-limiting for many slag phases. The presence of a crystalline slag may also have an effect on the kinetics of reaction product formation. The surface chemistry of different minerals have been shown to

change the nucleation rate of C-S-H [55].

The second challenge is variation in both the crystalline phases present in a given slag and in the aqueous phase chemistry to which the slag is exposed. Crystalline slag phases have different chemical and physical properties – some may dissolve rapidly, others may dissolve slowly but be mechanically sound. Mix proportions for a concrete which incorporates a given crystalline slag and has good mechanical properties are not necessarily appropriate for other crystalline slags, even if both are ostensibly the same slag, e.g. both slags are BOF slags. The variation in steel and copper slags phase composition has many sources – the chemistry of the furnace feedstock, the fluxes introduced to the furnace for slag formation, the cooling procedure for slags, and the extent of weathering which the slag undergoes. The result of this is that rarely are 2 slags identical. Finally, dissolution rates and rates of reaction product nucleation on a surface are also a function of the aqueous environment to which the slag is exposed. Dissolution rates are typically a function of pH, temperature, and the concentrations of other aqueous ions. All of these solution properties vary from concrete to concrete. Alkali-activated materials have highly alkaline, aluminum and silicon rich aqueous phases, while Portland cement based binders have contents of sulfur, calcium, and silicon. A mineral surface (e.g. limestone) which is observed to accelerate nucleation rates of one reaction product type (e.g. C-S-H) may not have the same effect on other reaction products (e.g. N-A-S-H). The importance of this phenomenon rests on the observation that the region of the concrete in the vicinity of the aggregate surface (up to 100 μm from the surface) is typically the mechanically weakest region of the concrete through which cracks form [56]. The formation of a dense microstructure in this region is critical to the development of a mechanically sound concrete. This goal of this thesis is to identify beneficial use pathways for steel and copper slags by addressing the above mentioned challenges, as discussed below.

1.3 Research Questions and Thesis Plan

As discussed above, there exists variability in both the composition of steel and copper slags, and in the aqueous phase of the concrete to which they are exposed upon mixing. This variability makes case-by-case studies of specific slags under specific aqueous conditions un-scalable. Rather, we require an approach that furthers our understanding of how the crystalline phases present in steel and copper slags interact with the aqueous solutions typical of cementitious systems. In this way, the overall behavior of the whole slag can be approximated as the sum of the behavior of its constituent phases. There are 2 ways in which the crystalline phases of a slag may interact with the aqueous phase of the concrete in which they are incorporated; through dissolution of ions from the crystalline phases into solution, and by precipitation of ions out of solution onto the surface of the crystalline phases.

With regard to dissolution rates of crystalline phases from steel and copper slags, it is not possible to measure the dissolution rates of all possible slag phases, and here I focus on 2 olivine minerals - calcio-olivine and fayalite. These phases are of interest for their abundance in steel and copper slags, respectively. The abundance of these phases in steel and copper slags is examined further in Chapter 5. The research questions with regard to the dissolution of these phases can be summarized as follows;

- What is the dissolution rate of these phases in basic solution?
- How does the dissolution rate change as a function of pH and Ca^{+2} concentration?
- What are the properties of the surface that determine the dissolution dependencies of these phases?

These research questions are designed to address gaps in the literature surrounding these phases. Firstly, measuring the previously unmeasured dissolution rate of both phases under high pH conditions allows the reactivity of these phases to be assessed in the context of cementitious systems. Secondly, determining the dissolution rate as

function of pH and Ca^{+2} concentration informs the usefulness of these phases in alternative binders with different aqueous environments. For example, NaOH dominated solutions are typical of alkali-activated materials and $Ca(OH)_2$ dominated solutions are typical of Portland cement based binders. Thirdly, elucidating how the surface properties of a phase influence its dissolution behavior offers opportunities to better understand the dissolution rate of chemically and structurally similar phases. These research questions are addressed in Chapter 3.

The influence of the surface properties of crystalline phases on reaction product formation was identified above as a key consideration for crystalline slag use in concrete. In this thesis I investigate the effect of aggregate surface chemistry on reaction product formation in Portland cement-type systems. The primary research question of this study is; how does aggregate surface chemistry affect the type, morphology, and kinetics of reaction product formation? The effect of aggregate surface chemistry is investigated on 4 surfaces; limestone, quartz, fayalite, and diopside. The first two of these phases are chosen because of their existing widespread use as aggregates in concrete. The latter two are chosen because of their abundance in steel and copper slags (see Chapter 5). The secondary research question of this study is; which properties of the surface account for observed differences between the surfaces? These research questions address gaps in the literature around the effect of surface chemistry on reaction product formation. Previous investigations have focused on imaging aggregate surfaces in mortars which are subject to physical constraints and local heterogeneity in reaction product formation [57, 58, 55]. These research questions are important for understanding the kinetics of reaction product formation, which profoundly influences the overall kinetics of cement hydration [54]. The type, morphology, and extent of reaction product formation also influences the density of the microstructure in the vicinity of the aggregate surface. The microstructure in this region is critical to the development of a mechanically sound concrete. This study is contained in Chapter 4.

Chapter 5 returns to the central theme of this thesis; how can we best identify beneficial uses for steel and copper slags in building materials? As discussed previously, knowledge of the kinetics of each process (dissolution of precursors, mass transport,

and nucleation and growth of reaction products) would allow for the development of more sophisticated and flexible cement hydration models. However, there is scant existing data measuring the kinetics of these processes. The experimental work in Chapters 3 and 4 goes some way to rectifying this. In this chapter, I attempt to build a model that accounts for the kinetics of both cement hydration and crystalline slag, with a focus on the dissolution rates of the latter. These efforts serve primarily to compile existing data of the kinetics of dissolution of these phases, to highlight gaps in this data, and to demonstrate a highly simplified hydration model for these systems. First, I complete a sweeping literature review to compile data on reported phase compositions and microstructures of copper, BOF, EAF, and LF slags. Second, dissolution kinetics for the most commonly observed phases in steel and copper slags are collected. The thermodynamics of dissolution in cementitious systems for these phases is also considered. Finally, the incorporation of crystalline slags into a cement hydration model is discussed. The framework offers a framework for identifying suitable or synergistic mix designs in which to incorporate a given crystalline slag.

In Chapter 6, I outline a previously unpublished methodology for calibrating pH meters in highly alkaline solutions such as those relevant to cementitious systems. The relevance of this work stems from the requirement for accurate aqueous phase characterization throughout the experimental work of this thesis. This methodology uses an extended form of the Debye-Hückel equation to generate a calibration curve of pH vs. the measured electrochemical potential (mV) based on a series of aqueous alkali hydroxide solutions of known concentrations.

This thesis concludes with recommendations for future work and my outlook on critical challenges faced by the research community in this field.

Chapter 2

Experimental methods

2.1 Inductively Couple Plasma Optical Emission Spectroscopy (ICP-OES)

An Agilent 5100 Vertical Dual View ICP-OES with an autosampler was used to analyze elemental concentrations of relevant elements during dissolution. Calibration standards were prepared from two standard solutions: one containing 1000 mg/L Si in H_2O and one containing 1000 mg/L each of Ca, Al, Na, K, Mg, Fe, and S in 4% HNO_3 (Elemental Scientific, Omaha, NE).

2.2 pH meter measurements

Solution pH values were measured using a Thermo Orion Ag/AgCl combination triode with Automatic Thermal Correction probe stored in KCl solution. Alkali error from measurements of highly alkaline solutions was accounted for by calibration of the pH meter using NaOH solutions of known concentration, discussed in Chapter 6.

2.3 X-ray photoelectron spectroscopy (XPS)

Surface chemistries were measured using a Thermo Scientific K-Alpha+ XPS with an Al K-alpha X-ray source and a beam spot size of 400 μm. Samples were filtered, washed in ethanol and dried under vacuum for several hours at ambient temperature. Powders were packed onto Cu tape for analysis. Elemental concentrations were calculated using the Avantage program.

2.4 Scanning Electron Microscopy and Energy Dispersive X-ray Spectroscopy (SEM & EDS)

Two different instruments were used for scanning electron microscopy. The first was used in Chapter 3. Powders were packed onto carbon tape and imaged on a JEOL 6610 Low Vacuum SEM equipped with an EDAX detector and energy-dispersive X-ray spectrometer (EDS). The second of these was a Zeiss Merlin High Resolution Scanning Electron Microscope which was used for imaging in Chapter 4.

2.5 X-ray diffraction (XRD)

Phase composition of the materials was determined by X-ray powder diffraction (XRPD). XRPD data was collected using high speed Bragg-Brentano optics on a PANalytical X'Pert Pro MPD operated at 45 kV and 40 mA. HighScore Plus software was used for quantitative X-ray diffraction (QXRD) using Rietveld analysis [59].

2.6 BET surface measurements

Krypton adsorption measurements at 77K were carried out using a Micromeritics 3Flex surface characterization analyzer (Micromeritics Instruments Corporation) to assess the specific surface area of the samples. Prior to the measurements, the samples were activated under secondary vacuum at 200°C for 12 hours. The Kr adsorp-

tion isotherms collected were interpreted using multi-point Brunauer-Emmett-Teller (BET) analysis for surface area determination [60] over the range 0.06–0.20 relative pressure (P/P_0) and with a Kr cross-sectional area of 0.210 nm^2. The determination of the minimum amount of sample needed was based on previous calibration of the instrument published in the Supplemental information of [61]. This calibration was achieved by varying the amount of an alumina reference material provided by the manufacturer that exhibits a calibrated surface area of 0.22 $\pm$ 0.03 m^2 g^{-1}. A minimum absolute sample area of 0.04-0.05 m^2 in the sample cell was needed in order to obtain reliable results.

Chapter 3

Dissolution rates of olivines

This chapter explores the effect of aqueous chemical environment on the dissolution rate of the minerals γ-C_2S and fayalite, identified as primary phases of ladle furnace steel slag and copper slag. γ-C_2S and fayalite were exposed to solutions of NaOH and $Ca(OH)_2$, chosen to mimic the pore solutions of alkali-activated and Portland-cement based binders respectively. While both from the olivine mineral group, γ-C_2S and fayalite displayed opposing dissolution trends with respect to pH. The rates of γ-C_2S dissolution were observed to decrease with higher pH, while fayalite dissolution rates increased with pH, and both relationships were described via empirical functions of the form $R = ka_{H^+}^n$. The contrasting dependence of dissolution rate on pH for both minerals was attributed to the formation of chemically distinct surface layers on both minerals during dissolution: the formation of an iron hydroxide layer on the surface of the fayalite altered the pH dependence. These results have significance for blending of slags with high olivine contents in binders with a range of aqueous chemical environments.

This chapter is adapted from the following publication:

> Brian Traynor, Ciara Mulcahy, Hugo Uvegi, Tunahan Aytas, Nicolas Chanut, and Elsa Olivetti. Dissolution of olivines from steel and copper slags in basic solution. Cement and Concrete Research, 133(March):106065, 2020 [62].

3.1 Introduction

Despite the work done to date on the performance of copper and steel slags in various concretes (see Section 1.2), there remains an important gap in the understanding of their reactivity in the aqueous chemical environments typical of Portland-cement or alkali-activated pore solutions. As dissolution of a precursor is the first step in the development of strong, load-bearing binder, understanding how these materials dissolve and how dissolution rates are affected by the aqueous environment is key to their effective use [63].

Dissolution rates are rarely measured in cement science. Geochemists have, however, been measuring the dissolution rates of geologically important minerals for decades. Much experimental data has been collected on dissolution rates of olivines, pyroxenes, and feldspars for the purpose of better understanding the weathering of the earth's crust. These studies seek to clarify the mechanisms of dissolution and the dependency of dissolution rate on variables such as pH, temperature, and saturation state. Many rate equations have been developed to described dissolution rates as a function of other variables. The most widely adopted and applied rate equation was developed by Aagard and Helgeson [64], shown in Equation 3.1;

$$r_{\phi_r} = k_{\phi_r} \sum_i a_i^{-\hat{n}_{i,j}} \left(1 - exp\left(-\frac{A}{\sigma RT}\right)\right) \tag{3.1}$$

where r_{ϕ_r} (mol cm^{-2} s^{-1}) is the dissolution rate of reactant mineral ϕ_r, k_{ϕ_r} (mol cm^{-2} s^{-1}) is the rate coefficient for the hydrolysis of reactant mineral ϕ_r, $a_i^{-\hat{n}_{i,j}}$ is the activity of the ith aqueous species raised to the power of the stoichiometric reaction coefficient for the ith aqueous species in the jth reaction, A (J mol^{-1}) is the chemical affinity for the overall dissolution reaction, σ is Temkin's stoichiometric number, R (J mol^{-1} K^{-1}) is the gas constant, and T (K) is the temperature of the solution. This rate equation combines both microscopic and macroscopic features of the dissolution process — the chemical affinity term links thermodynamics and kinetics, while the activity product links surface chemistry to kinetics via transition state theory. Equation 3.1 has been interpreted and expanded by many researchers to explicitly include

temperature dependences (through an activation energy term), and pH dependencies. Lasaga offered the most general form of a dissolution rate equation, shown in Equation 3.2;

$$Rate = k_0 A_{min} e^{-\frac{E_a}{RT}} a_{H^+}^{n_{H^+}} g(I) \sum_i a_i^{n_i} f(\Delta G_r) \tag{3.2}$$

where k_0 (mol cm^{-2} s^{-1}) is the rate constant, A_{min} (cm^2) is the reactive surface area, E_a is the apparent activation energy of the overall reaction, $a_{H^+}^{n_{H^+}}$ is the activity of aqueous hydrogen ions in solution raised to an empirical exponent, n_{H^+}, $g(I)$ is a function which describes the dependence on ionic strength, $\sum_i a_i^{n_i}$ is the activity of aqueous ions other than hydrogen raised to an empirical exponent, n_i, and $f(\Delta G_r)$ is a function which describes the dependence of rate on the distance from equilibrium (solution saturation in the terminology of dissolution reactions). A great deal of experimental work has been devoted to determining the values of n_{H^+} and E_a, as well as the form of $f(\Delta G_r)$. Determining values for n_{H^+} or E_a requires measuring rates at different pH values or temperatures while keeping all other variables constant. It should be noted that many models describing the form of $f(\Delta G_r)$ exist, but experimental difficulties in conducting dissolution rate experiments as a function of ΔG_r mean that the precise form of $f(\Delta G_r)$ remains elusive. Further complicating the matter is the fact that not all terms in Equation 3.2 are independent. For example, E_a depends on $a_{H^+}^{n_{H^+}}$, $g(I)$ depends on $a_{H^+}^{n_{H^+}}$ and $\sum_i a_i^{n_i}$, and ΔG_r is a function of $\sum_i a_i^{n_i}$ and $a_{H^+}^{n_{H^+}}$. Ultimately, this confusion stems from difficulties in describing series of elementary dissolution reaction steps, as well as large uncertainties in experiments. However, no single set of experiments attempts to probe every term in Equation 3.2.

At far from equilibrium conditions, dissolution rates generally show no dependence on ΔG_r for small changes in solution composition. For this reason, the vast majority of dissolution experiments are conducted at far from equilibrium conditions. The majority of experiments are also performed in acidic or neutral conditions. Experiments in which dissolution rates are measured as a function of pH or temperature are relatively simple, while dissolution rate experiments as a function of the concen-

tration of other aqueous ions or saturation state are experimentally more challenging. Saturation states are calculated on the basis of the difference between the ion activity product (IAP, denoted by Q) and the equilibrium constant (K) for the dissolution reaction. The IAP is related to the Gibbs free energy of the dissolution reaction (ΔG_{diss}) through the law of mass action, shown in Equation 3.3;

$$\Delta G_{diss} = RT \times ln\frac{Q}{K} \tag{3.3}$$

The relationship between dissolution rate and ΔG_{diss} is non-trivial. Thermodynamics dictates that the dissolution rate must go to zero as ΔG_{diss} goes to zero. Understanding the form of $f(\Delta G_r)$, as shown in Equation 3.2 is fundamental in understanding dissolution rate laws. Many functionals form for $f(\Delta G_r)$ have been proposed. These functions normally are derived from either transition state theory or crystal growth theory and contain parameters that are determined empirically.

While steel slag and copper slag are heterogeneous materials, the primary mineral phases of both come from only a few mineral groups. Here, we focus on the primary mineral phases of LFS and copper slag; γ-C_2S (calcio-olivine, γ-Ca_2SiO_4) and fayalite (Fe_2SiO_4), respectively. The reasons for studying the dissolution kinetics of these two minerals are twofold. First, γ-C_2S and fayalite are the primary phases of their respective slags, meaning that the dissolution kinetics of these mineral phases will have a major impact on the dissolution of the overall slag [29]. Second, γ-C_2S and fayalite are both members of the same mineral group; the olivines. While these two minerals have been the subject of limited research, a third mineral in the olivine mineral group, forsterite (Mg_2SiO_4), has been widely studied by geochemists due to its prominence in the earth's crust. As members of the same mineral group, γ-C_2S, fayalite, and forsterite are all expected to exhibit similar properties and reactivity in solution. Past work on forsterite is therefore pertinent to this work on γ-C_2S and fayalite. Most studies of forsterite dissolution are in acidic solutions and previous studies [65] have shown the mechanism of olivine dissolution at low pH to proceed through ion exchange of metal cations with H^+ ions in solution. In this region, the

rate of dissolution has been described as a function of H^+ ion activity, described in Equation 3.4;

$$R = ka_{H^+}^n \tag{3.4}$$

where R is the rate of dissolution of olivine, k is the rate coefficient, a_{H^+} is the activity of H^+ in solution, and n is an empirically determined constant. Equation 3.4 is typically plotted in the form of $log(R) = log(k) - n \times pH$, meaning that a positive value of n implies that dissolution rates decrease with higher pH. For forsterite dissolution in acidic solutions, n has been reported in the range 0.46 to 0.54 [66]. Equation 3.4 has also been used to describe the dependence of dissolution rate as a function of pH in basic solutions. The value of n for forsterite dissolution in basic solutions has been the subject of fewer studies, but has been variously proposed to be 0.22 [67], 0.25 [66] and -0.39 [68]. Decreasing rates of dissolution at higher pH is a behavior contrary to the majority of silicates [69]. Despite extensive studies of forsterite at low pH, γ-C_2S and fayalite, while common in slags, are comparatively understudied. Westrich et al. calculated a value for n of 0.42 for γ-C_2S in acidic solutions, but to the best of our knowledge no studies have reported rates of γ-C_2S as a function of pH in basic solutions. Several studies have investigated the hydraulicity of γ-C_2S by means of calorimetry [70, 71, 72]. Fayalite has been studied both in acidic and basic solutions, often with conflicting conclusions. In acidic solution, positive values of n have been reported (0.69 and 0.74) [73, 74]. An increase in dissolution rate at higher pH (n of -0.39 [75] and -0.31 [73]) has been proposed based on comparison with other iron silicates, but not experimentally confirmed.

In this study, we explore the effect of the aqueous environment on the rate of dissolution of γ-C_2S and fayalite. The dependence of dissolution rate on pH are measured in NaOH and $Ca(OH)_2$ solutions designed to mimic the aqueous environments typical of Portland-cement (moderate pH, high Ca) and alkali-activated (high pH, low Ca) binders. By understanding how these minerals react in basic solutions, the reactivity of slags with high olivine content can be anticipated for a range of aqueous chemical environments typical of traditional and alternative binders.

3.2 Materials and Methods

3.2.1 Materials

LFS consists of multiple calcium silicate minerals (including diopside, merwinite, wollastonite and larnite), with γ-C_2S often present as the major phase. In order to focus on this dominant phase, a synthetic γ-C_2S was used to study γ-C_2S dissolution kinetics in this work. Fayalite is typically the only silicate phase present in copper slag. For this reason, both a synthetic fayalite and a fayalitic copper slag (referred to as fayalite slag) were used to study the dissolution kinetics of fayalite.

All γ-C_2S powders were synthesized using the modified Pechini synthesis method, based on the method described by Nettleship et al. [76, 77]. Stoichiometric quantities of $Ca(NO_3).4H_2O$ (19.543 g) (>99.995%, Alfa Aesar) and colloidal silica (7.421 g of 34 wt% colloidal silica) (LUDOX TMA, Sigma Aldrich) were combined in a beaker with 150 mL of deionized water. The solution was stirred at 240 rpm, and brought to a boil in a water bath. Citric acid (91.3 g) (ACS reagent, >99.0%, Sigma Aldrich) was added to the solution, which was then covered using aluminum foil. The solution was stirred for 30 minutes, after which the foil was removed and ethylene glycol (60.876 g) (Fisher Scientific) was added. Throughout the process, the water bath was repeatedly replenished until the solution started to turn viscous (several hours), at which point the solution (now gel) was poured into silicone molds. The gel was dried out completely in a drying oven at 170°C for 24 hours before being ground up in a mortar and pestle and calcined at 1400°C for 6 hours. The powder was calcined 4 times to achieve a pure γ-C_2S phase. The product was washed repeatedly in isopropanol to remove smaller particles (<1 μm) from the surface of the γ-C_2S powder.

A fayalite copper slag was used as the primary fayalite source (source: Hindalco Industries, Mumbai, India). The chemical composition as determined by XRF is shown in Table 3.1. Chemical composition was determined on an Axios PANalytical XRF (based on dry material in its most stable oxidation state). Fe is reported as Fe_2O_3 although is present as Fe(II) in fayalite. The fayalite slag was ground in a

Oxide	wt%	mol% (excl. LOI)
Na_2O	0.34	0.61
MgO	1.13	3.12
Al_2O_3	2.83	3.09
SiO_2	21.68	40.20
SO_3	1.91	2.66
K_2O	0.78	0.92
CaO	1.76	3.50
TiO_2	0.24	0.33
Fe_2O_3	59.94	41.82
CuO	0.83	1.16
MoO_3	0.31	0.24
PbO	0.24	0.12
ZnO	0.86	1.18
LOI	6.25	0

Table 3.1: XRF composition of fayalitic copper slag.

SPEX tungsten carbide grinding vial set and washed repeatedly with isopropanol to remove smaller particles (<1 μm) prior to dissolution tests.

Fayalite was synthesized using Fe (<212 μm, Acros Organics, 99%), Fe_2O_3 (30-50 nm, Alfa Aesar, 98%) and SiO_2 (<0.5 μm, Alfa Aesar, 99.9%) precursors. Precursor powders were subjected to 30 minutes of high energy ball milling under argon atmosphere in a SPEX tungsten carbide grinding vial set. The powder was heated to 750°C under argon atmosphere for 24 hours. The heating cycle was done 3 times and the powder ball milled under argon atmosphere between each heating cycle. Phase composition was determined by X-ray powder diffraction (XRPD), as described in Section 2.5. γ-C_2S was synthesized to a purity of >98%, with the remainder β-C_2S impurities, shown in Figure 3-1.

The major mineral phase of the fayalite slag was fayalite. Minor phases of sodium sulfate, hematite and copper metal were detected through a combination of XRPD and SEM-EDS analysis. A sample SEM-EDS image is shown in Figure 3-2. While phases other than fayalite were detected in XRPD and SEM-EDS analysis, no other phases containing Si were detected. The fact that Si appears to reside entirely in fayalite is the basis for the assumption that dissolved Si is derived solely from fayalite dissolution.

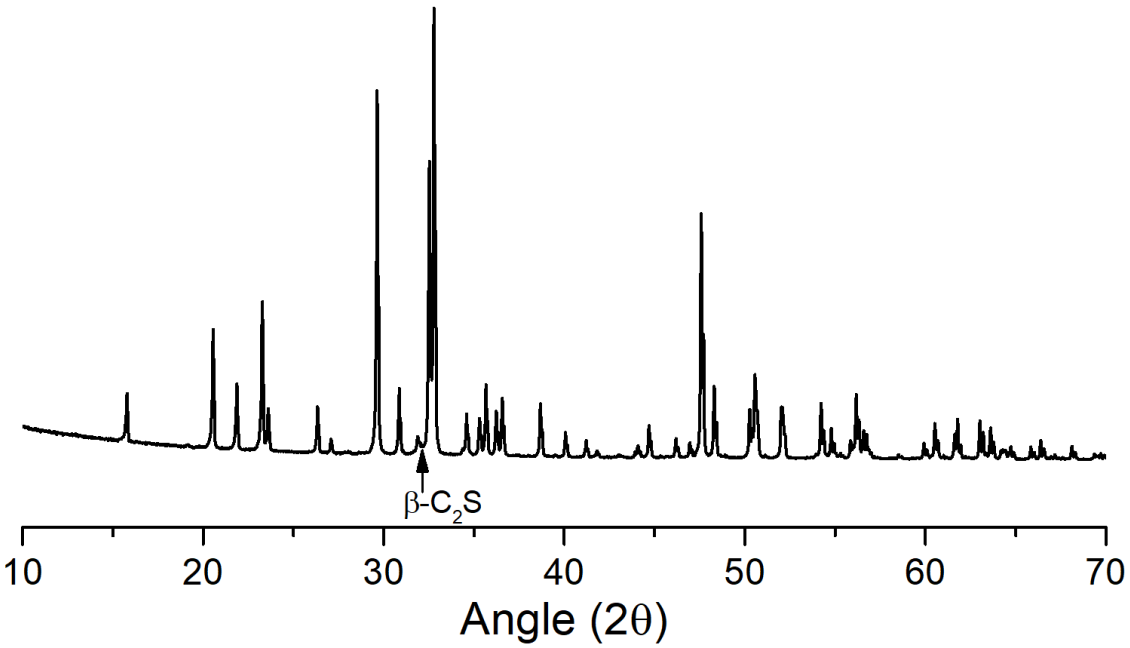

Figure 3-1: XRPD pattern for γ-C_2S. Rietveld analysis indicated a pure γ-C_2S powder. β-C_2S was identified as the main impurity on previous calcinations but is present in negligible quantities here. The arrow indicates the strongest β-C_2S diffraction peak and all other peaks belong to γ-C_2S.

XRPD Rietveld analysis of the synthetic fayalite is depicted in Figure 3-3. Only metallic iron was detected as an impurity. Unreacted precursor amorphous silica was not detected but may exist in small quantities ($<$5 wt%). Detecting amorphous silica is complicated by the high background in the diffraction pattern due to Fe fluorescence (Co x-ray source is used). SEM imaging of the synthetic fayalite revealed clusters of nano-particles, shown in Figure 3-4. Small particle precursors were used to promote a complete reaction to fayalite. While fayalite was synthesized to a high purity, particles were not sintered.

The surface areas of the powders used were determined as described in Section 2.6. To ensure the reliability of the results obtained, 300-400 mg have been used for each sample.

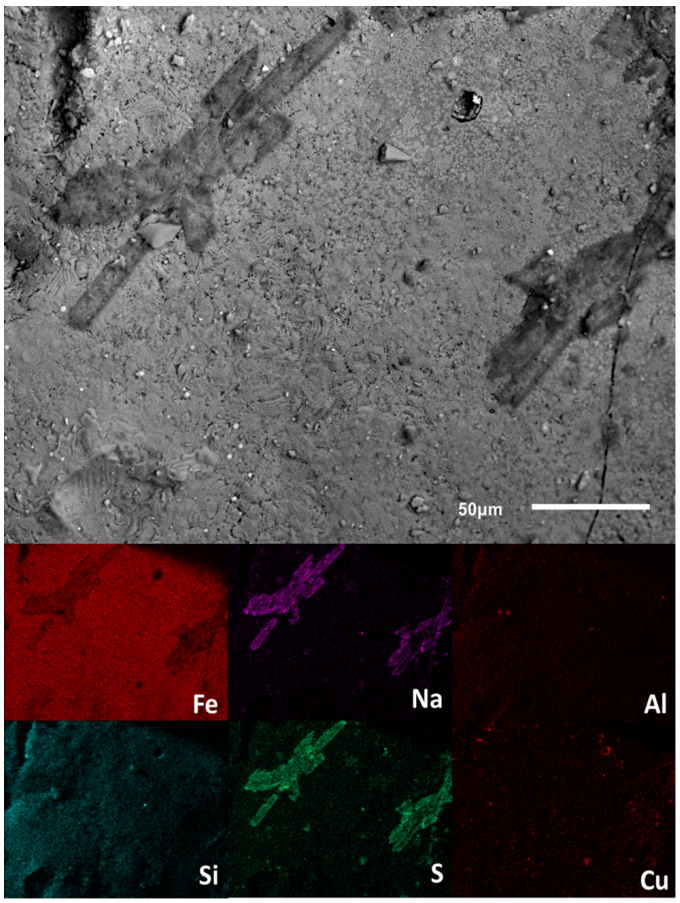

Figure 3-2: SEM-EDS analysis of fayalite slag surface. There are 3 distinct identifiable regions: high iron and silicon concentration, attributed to fayalite; high sodium and sulfur concentration region, attributed to sodium sulfate salt; and small regions of high Cu (attributed to Cu metal) and Al concentration.

3.2.2 Dissolution

The dissolution behavior of the powders was investigated in different aqueous environments: γ-C_2S in 0.0001 M (mol Na/L), 0.0005 M, 0.001 M, 0.005 M, 0.01 M, 0.05 M, 0.1 M, 0.5 M NaOH solutions and 0.001 M (mol Ca/L), 0.0017 M, 0.0038 M, and 0.012 M $Ca(OH)_2$ solutions; and fayalite in 0.0001 M (mol Na/L), 0.001 M, 0.01 M, and 0.1 M NaOH solutions. The dissolution experiments were performed at liquid:solid ratios of 10,000:1 in batch reactors to prevent precipitation of reaction products, e.g. calcium silicate hydrate (CSH). 0.05 g of powder was added to 500 mL of solution to initiate dissolution. 5 mL of solution was removed at specified intervals for further analysis and the solution was immediately replenished with 5 mL of pure

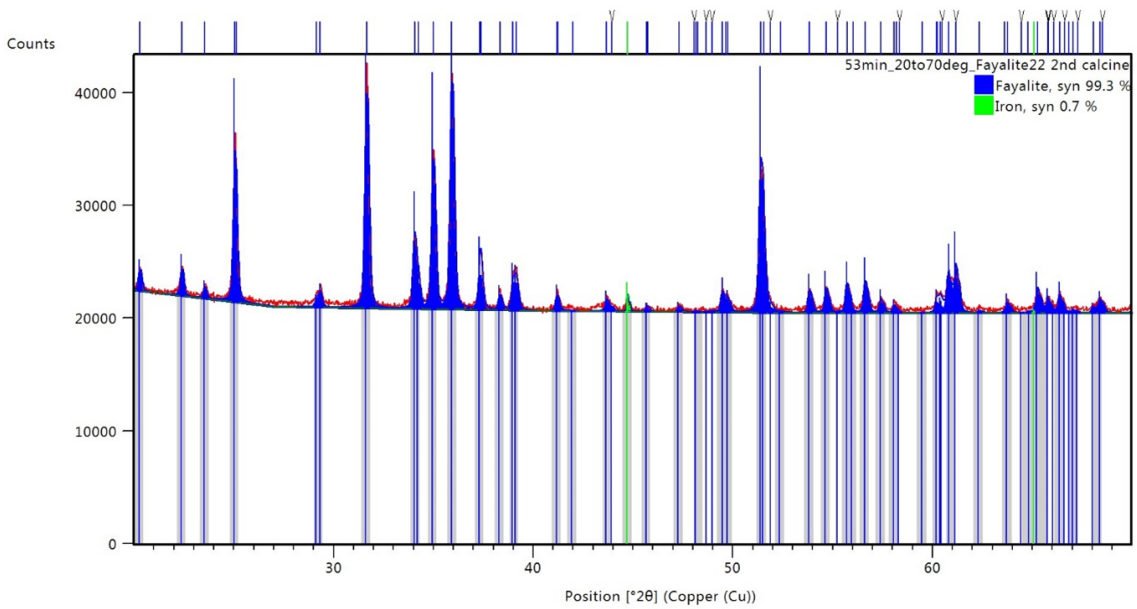

Figure 3-3: XRPD Rietveld analysis of the synthetic fayalite. Metallic iron is detected as a minor phase.

solution. Samples were not stirred to avoid particle abrasion.

An Agilent 5100 Vertical Dual View ICP-OES with an autosampler was used to analyze elemental concentrations of relevant elements during dissolution. Calibration standards were prepared from two standard solutions: one containing 1000 mg/L Si in H_2O and one containing 1000 mg/L each of Ca, Al, Na, K, Mg, Fe, and S in 4% HNO_3 (Elemental Scientific, Omaha, NE). Solution pH values were measured, as described in Section 2.2. The morphologies and particle sizes of the powders were imaged using scanning electron microscopy (SEM), as described in Section 2.4. Characterization of surface chemistries is described in Section 2.3.

GEM-Selektor v3.3 (http:// gems.web.psi.ch/) [9, 10] with PSI-Nagra [4] and Cemdata18 [11] databases were used to calculate ion activity products. The aqueous electrolyte model used to determine the activity of ions in solution was the extended Helgeson form of the Debye-Hückel equation with ion size and extended term parameters of NaOH background electrolyte ($\dot{a}$ = 3.31 Å and b_γ = 0.098 kg mol^{-1}) [78]. The osmotic coefficient and the Debye-Hückel extended term were used to calculate the activity of water and neutral species respectively.

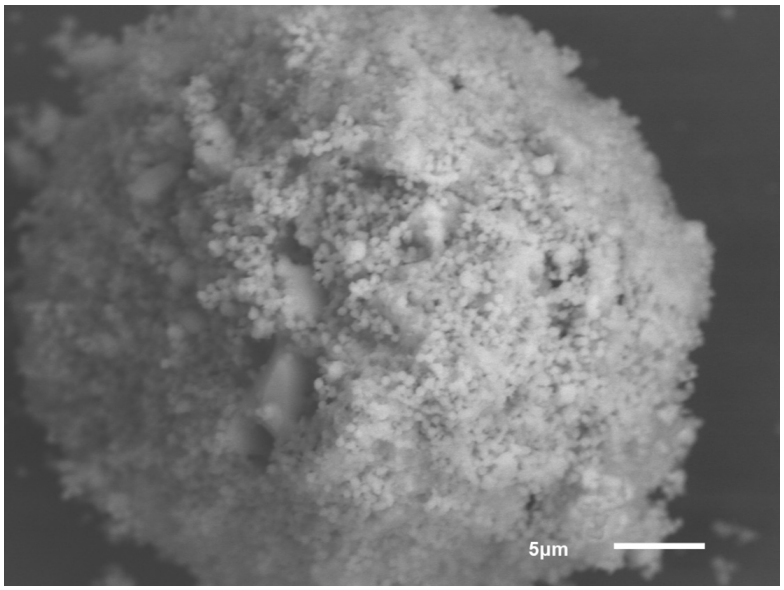

Figure 3-4: SEM image of synthetic fayalite particle.

3.3 Results

3.3.1 γ-C_2S

The effect of pH on the dissolution rate of γ-C_2S in NaOH and $Ca(OH)_2$ is shown in Figure 3-5. Dissolved Si (Figure 3-5A) and Ca (Figure 3-5B) concentrations are reported in NaOH solution. The high background concentration of Ca in $Ca(OH)_2$ solutions resulted in an insignificant change in overall Ca concentrations from dissolved Ca, and only Si concentrations are reported for $Ca(OH)_2$ solutions.

At higher pH in both NaOH and $Ca(OH)_2$ solutions, the dissolution of γ-C_2S is slower. For all NaOH molarities, dissolution is rapid up to 6 hours. Dissolution slows to a constant rate between 6 hours and 96 hours and rates appear to decrease beyond 96 hours. In $Ca(OH)_2$ solutions, Si concentrations did not increase rapidly up to 6 hours as in NaOH solutions. The rate of Si dissolution in $Ca(OH)_2$ reaches a steady-state between 6 and 48 hours, before decreasing slightly. We refer here to the constant rate of dissolution as the "steady-state" regime. Dissolution proceeds congruently within the uncertainty of the ICP-OES measurements. The rapid dissolution up to 6 hours in NaOH solutions is likely due to one or both of: dissolution of small particles with very high specific surface area that completely dissolve within the first few hours;

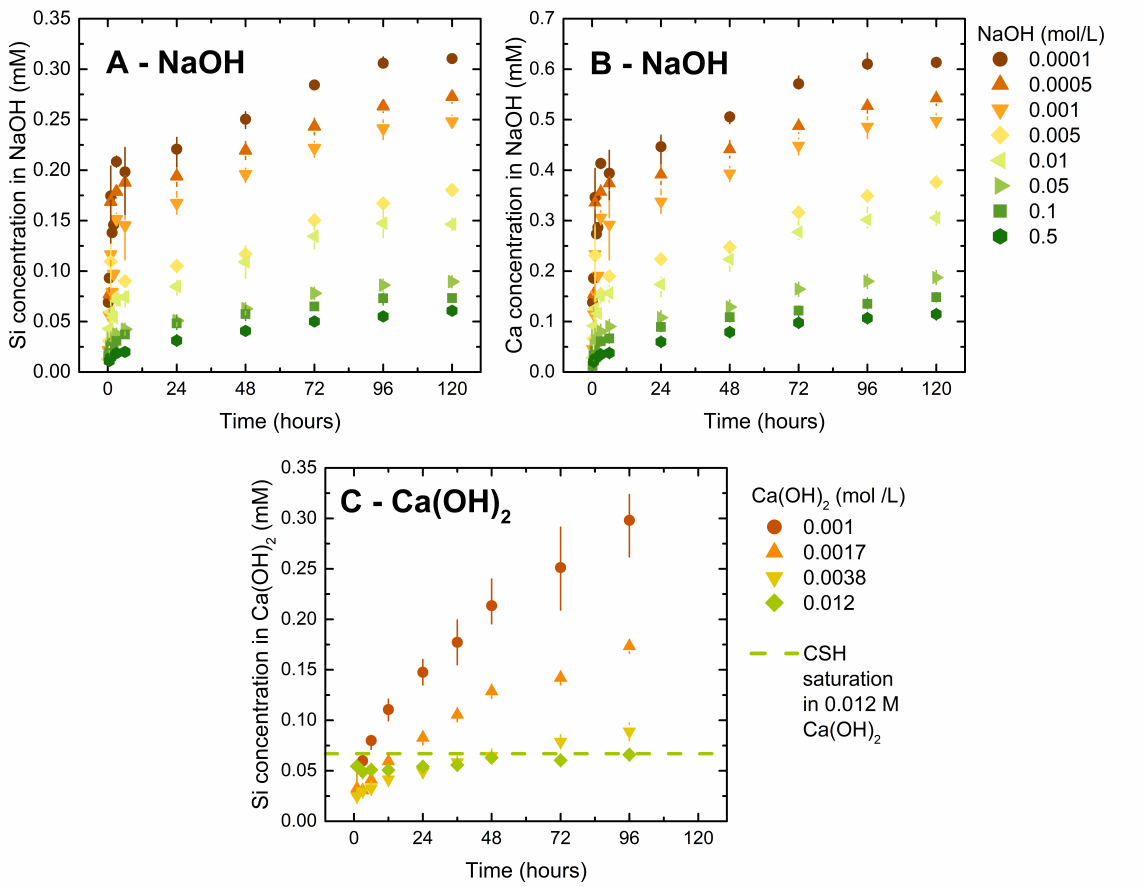

Figure 3-5: Dissolution kinetics of γ-C_2S in solutions of NaOH (A and B) and $Ca(OH)_2$ (C) at liquid:solid ratios of 10,000:1. Dissolved Si and Ca concentrations (milli-molarity) are shown as a function of time for different solution molarities. Saturation states for calcium silicate hydrate (CSH) are represented by the horizontal dotted lines. As CSH was only predicted to precipitate in the 0.012 M $Ca(OH)_2$ experiment, it is the only solution for which the CSH saturation is shown. Error bars represent maximum and minimum values of triplicate experiments.

dissolution of impurity β-C_2S which dissolves orders of magnitude more rapidly than γ-C_2S. The reason for the apparent decrease in rate at late age (96 hours in NaOH, 48 hours in $Ca(OH)_2$) is not clear as no phases are expected to precipitate at these concentrations based on calculated saturation states of relevant phases (as calculated in GEMSelektor). Growth of a surface layer, either through formation of a leached layer or a precipitated secondary mineral, that slows dissolution at later ages is the most likely explanation for this trend — this is discussed below. Only in 0.012 M $Ca(OH)_2$ after 48 hours are reaction products in the form of calcium silicate hydrate (based on the solid solution model of [79]) expected to precipitate. Otherwise, no

reaction products are expected in the other NaOH or $Ca(OH)_2$ solutions. The pH of the 0.0001 M, 0.0005 M and 0.001 M NaOH solutions rose from values of 10, 10.85, and 11.11 to 10.93, 11.07, and 11.21, respectively, by 6 hours of dissolution due to formation of OH^- ions in solution following Ca^{2+} dissolution from the γ-C_2S. There was no discernible change in the pH over time for the other NaOH and $Ca(OH)_2$ solutions.

Scanning electron micrographs of γ-C_2S particle surfaces after 120 hours of exposure to NaOH and $Ca(OH)_2$ solutions are shown in Figure 3-6. Powders exposed to lower pH solutions are more etched, indicating greater extent of dissolution in agreement with the ICP-OES data discussed above. The formation of etch pits on a dissolving surface is well documented in the literature as a mechanism for mineral dissolution at far from equilibrium conditions [80, 81, 82, 83, 84]. The smaller extent of pitting on the particles at higher pH suggests weaker driving force for dissolution, and lower extent of dissolution than in low pH solutions. There is also no evidence of formation of reaction products at this length scale.

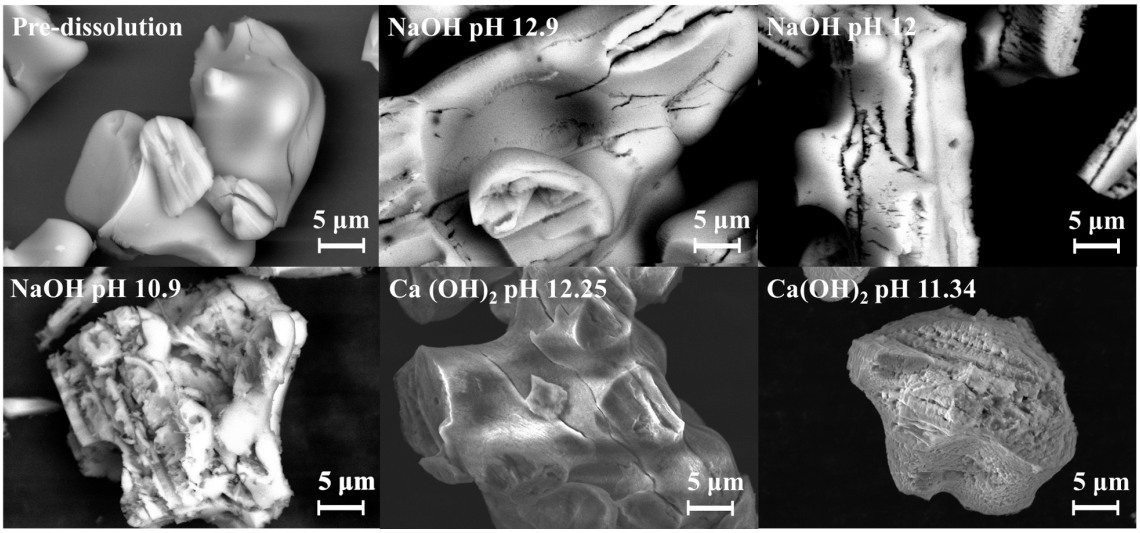

Figure 3-6: Scanning electron micrographs of γ-C_2S pre- and post-exposure to NaOH or $Ca(OH)_2$ solutions of varying pH.

Changes in the surface chemistry of the calcium silicate particles as a function of time were monitored using X-ray photoelectron spectroscopy. Table 3.2 shows the Ca/Si ratio at the surface of calcium silicate powders exposed to pH 10 and pH 11

	Ca/Si atomic ratio (pH 10 NaOH)	**Ca/Si atomic ratio (pH 11 NaOH)**
Pre-dissolution	2.00±0.07	2.00±0.07
1 day exposure	1.85±0.03	1.96±0.02
7 days exposure	1.54±0.04	1.74±0.04

Table 3.2: Ca/Si ratios at the surface of the sample as measured by XPS. Errors are based on the range observed from 10 measurements.

NaOH. The Ca/Si ratio for the pristine powder has been normalized to 2 and all other Ca/Si ratios scaled accordingly. The Ca/Si ratio decreases over time and the change is more pronounced in lower pH solutions with greater extents of dissolution. The electron escape depth for SiO_2 is on the order of 2.6 nm [85], and Zakaznova-Herzog et al. estimated the analysis depth for olivines and pyroxenes to be on the order of 7.8 nm (x3 the electron escape depth) for an Al K-alpha source [86]. This analysis depth represents tens of monolayers at the surface a depth which is likely to partly obscure surface specific chemistry. Further interpretation of these results will be discussed below.

3.3.2 Fayalite dissolution

The effect of pH on the dissolution rate of fayalite is shown in Figure 3-7. Dissolved Si concentrations in NaOH are reported. Goethite (α-FeO(OH)) is known to precipitate at very low Fe concentrations in basic solutions, and no meaningful kinetic information can be discerned from Fe concentrations. Fe data is therefore not reported.

While the rate of fayalite dissolution is pH dependent, the trend is opposite to that of γ-C_2S with fayalite apparently experiencing faster dissolution at higher pH. Approximately steady-state dissolution occurs between 12 and 72 hours at each NaOH molarity. The reason for initial decreases in Si concentration from 3 to 6 hours for 0.0001 M, 0.001 M, and 0.01M solutions is not known. At later age, the most likely reason for the decline in dissolution rate is the growth of a goethite precipitate layer on the surface of the fayalite slag particles which inhibits dissolution. The surfaces of the fayalite slag particles were imaged using SEM pre- and post-dissolution, although

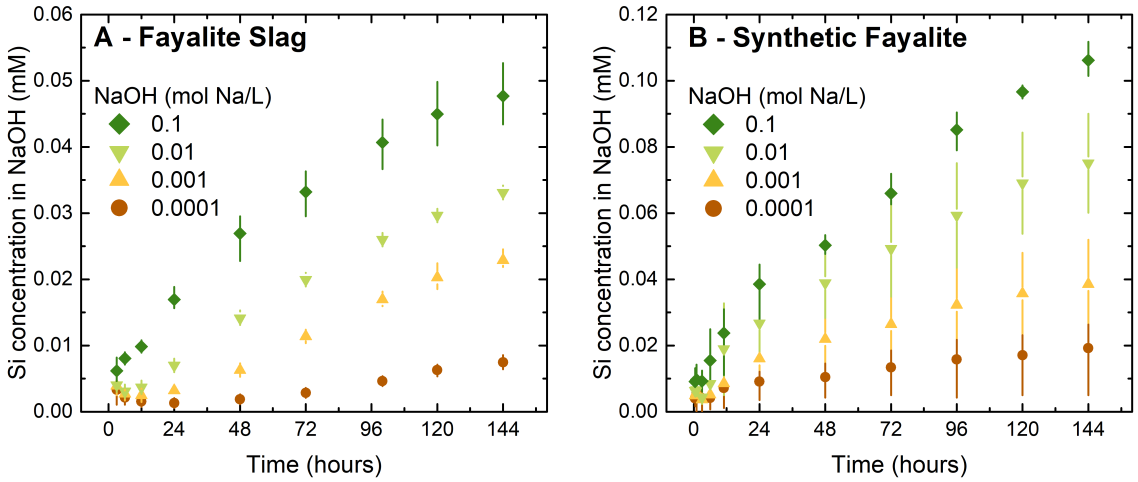

Figure 3-7: Dissolution kinetics of; A - fayalite slag and B - synthetic fayalite, in solutions of NaOH at liquid:solid ratios of 10,000:1. Dissolved Si concentrations (millimolarity) are shown as a function of time for different solution molarities. Error bars represent maximum and minimum values of triplicate experiments.

no discernible difference was observed. Possible reasons for the different dissolution behavior of γ-C_2S and fayalite are discussed below.

3.4 Discussion

3.4.1 Rate of dissolution in basic media

The rate of dissolution of γ-C_2S, R (moles cm^{-2} s^{-1}) was calculated from the steady-state dissolution regime using Equation 3.5;

$$R = \frac{\Delta C_i}{\Delta t} \frac{V_{soln}}{A_{BET}\, m\, \nu_i} \tag{3.5}$$

where ΔC_i (mol L^{-1}) is the change in element i concentration over change in time $\Delta t(s)$, $V_{soln}(L)$ is the volume of the solution, A_{BET} (cm^2 g^{-1}) is the specific surface area of the powder from BET, $m(g)$ is the mass of powder in solution, and ν_i is stoichiometry of element i in the dissolving olivine ($\nu_{Ca} = 2$, $\nu_{Si} = 1$). BET specific surface areas of γ-C_2S and fayalite slag were measured to be 0.42±0.01 (cm^2 g^{-1}) and 0.59±0.01 (cm^2 g^{-1}), respectively.

Rates of dissolution of γ-C_2S as a function of pH in NaOH, $Ca(OH)_2$ and acid

are shown in Figure 3-8A. Rates of dissolution of in NaOH and $Ca(OH)_2$ solutions are from this study while rates in acid are from Westrich et al [6], the only other study that reported γ-C_2S dissolution rates, to the authors' knowledge. Linear fits are based on the form of Equation 3.4, where n describes the slope. Calculated rates use Si concentrations in solution. The average value of n for NaOH solutions across all experiments was 0.24, although values from 0.18 to 0.33 were calculated from repeat experiments. This result agrees with reported forsterite dissolution rates as a function of pH in basic solution, where values of n=0.25 are typically reported [66]. For $Ca(OH)_2$ solutions, the average value of n was 1.2, with values from 1.17 to 1.25 being measured. γ-C_2S rates are fitted with a slope of 0.5 in acidic pH [6] in line with the vast majority of experimentally determined values of $n = 0.5$ for forsterite dissolution [66]. The rates of the dissolution in acid and NaOH solutions approximately converge at neutral pH. In contrast to γ-C_2S dissolution rates, fayalite dissolution was faster at higher pH. Rates of fayalite dissolution are complicated by the redox chemistry of iron, as has been reported previously in the literature [73, 75, 87, 88]. Rates of fayalite slag dissolution as a function of pH are shown in Figure 3-8B. The model of Wogelius and Walther [73] shown in Figure 3-8B is not based on experimentally measured rates and is an extension of a model for fayalite dissolution in acidic solution. This extension assumed that the rate as a function of pH in basic solution follows a rate law of the form of Equation 3.4, where $n = —0.31$. No value of n is proposed here due to the sparsity and uncertainty of the data, and the previously proposed $n = —0.31$ appears to fit adequately. Although the dependence of dissolution rates on pH for fayalite is opposite to that of γ-C_2S, absolute rates of Si dissolution from fayalite are 3 orders magnitude faster than γ-C_2S dissolution rates.

The stronger pH dependence of dissolution rates in $Ca(OH)_2$ solution is due to the common-ion effect. High concentrations of Ca already in solution slow dissolution of γ-C_2S by lowering the thermodynamic driving force for dissolution. Dissolution proceeds via the chemical reaction shown in Equation 3.6;

$$Ca_2SiO_4(s) + 3H_2O(aq) \rightarrow 2Ca^{2+}(aq) + H_3SiO_4^-(aq) + 3OH^-(aq) \qquad (3.6)$$

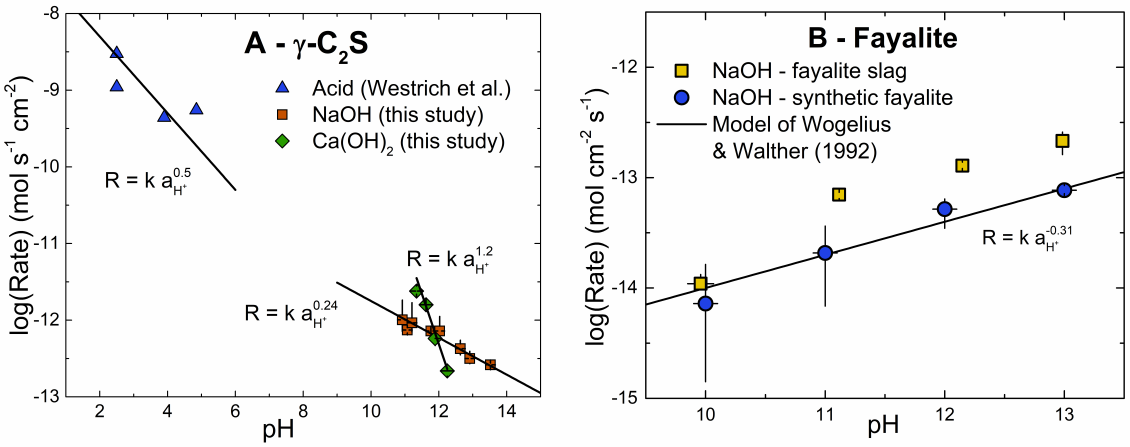

Figure 3-8: A: Rates of dissolution of γ-C_2S in NaOH, $Ca(OH)_2$ and acid solutions as a function of pH. B: Rates of dissolution of fayalite slag in NaOH solution as a function of pH. The error bars represent minimum and maximum rates of triplicate experiments, where the major source of error is in measured Si concentrations across experiments.

Equation 3.6 is irreversible under far from equilibrium conditions such as those described in this study. The affinity for the reaction to occur is defined in Equation 3.7;

$$A = RT \times ln\left(\frac{IAP}{K_{sp}}\right) \tag{3.7}$$

where R is the gas constant, T is the temperature, IAP is the ion activity product, and K_{SP} is the solubility product of the dissolution reaction. Larger affinities correspond to a system further from equilibrium with a stronger driving force for dissolution. In highly dilute systems, such as the ones in this system, the chemical affinity is assumed to remain constant during dissolution as the dissolved aqueous species do not significantly change the ion activity product of the solution over the course of the experiment. However, the ion activity product for Equation 3.6 ($\{Ca^{2+}\}^2\{H_4SiO_4^-\}\{OH^-\}^3$, where {X} is the activity of aqueous species X in solution) is greater in $Ca(OH)_2$ solutions due to the large background concentration of Ca ions already in solution. This is illustrated in Figure 3-9, where the ion activity product of each solution (calculated in GEM-Selektor) is plotted as a function of pH. NaOH solutions have lower ion activity products and therefore greater affinities for dissolution than $Ca(OH)_2$ solutions of the same pH. Although Oelkers et al. re-

ported rates of forsterite (Mg_2SiO_4) to be independent of Mg and Si concentration [89]. However, their study was performed in acidic media and at lower cation and Si concentrations (<1.5 mM) than in this study.

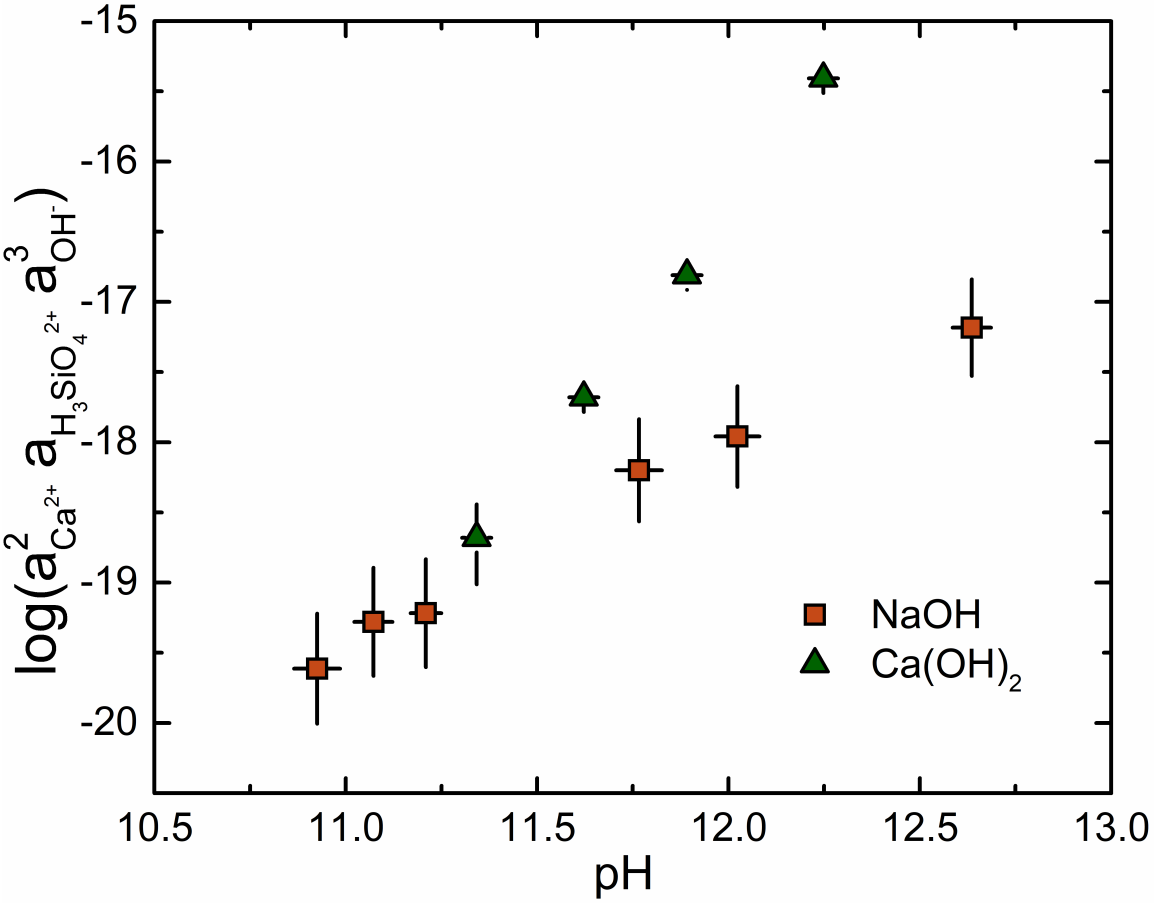

Figure 3-9: Ion activity products (based on Equation 3.6) as a function of pH for NaOH and $Ca(OH)_2$ solutions. The error bars represent the minimum and maximum values of triplicate experiments.

3.4.2 Surface Chemistry

Surface chemistry, as probed by XPS, provides insight into what limits dissolution of γ-C_2S and fayalite [88]. As described above, γ-C_2S powders were Ca deficient at the surface following exposure to NaOH solution. The Ca deficiency was more pronounced at lower pH and at later ages. There are two possibilities for this Ca deficiency. The first possibility is Ca leaching from the surface, leaving behind a Si-rich skeleton.

XPS studies of forsterite have shown a surface enriched in Mg in basic solutions, and surfaces deficient in Mg in acidic solutions [86, 90, 91, 92, 93]. These studies concluded that below pH 9, the surface is depleted in Mg due to an ion exchange reaction involving H^+ ions from the solution, while in more alkaline solution, selective leaching of Si from olivine surfaces occurs. In this study, Si-rich surfaces are observed in basic solution, meaning selective surface leaching is not the mechanism being observed here. A related phenomenon involves formation of an Si-rich layer at the surface of olivines and other calcium silicate minerals following exposure to solution. This phenomenon, first reported by Hellman et al. [94], is described as a coupled dissolution-precipitation reaction in which silica phases precipitate on the surface of the dissolving mineral. These porous layers do not necessarily hinder dissolution and can form in solutions in which anhydrous amorphous silica is undersaturated in the bulk solution, as is the case for the aqueous systems in this study [95, 96]. Transition electron microscopy and energy dispersive X-ray analysis has identified a Si-rich surface layer of thickness <5 nm on weathered forsterite [97]. Si-rich layers have also been reported on the surface of other calcium silicate minerals, including wollastonite, β-C_2S, anorthite, and diopside [95, 97, 98]. This phenomenon most likely accounts for the observed Ca/Si ratios in this study. The decrease in the Ca/Si ratio with time suggests continued growth of an amorphous silica layer on the surface of the particles over the timescale of the experiment. Additionally, at lower pH, there is more Si in solution available for the formation of such a layer resulting in a thicker layer than for particles exposed to higher pH solution. The leached layer and coupled interfacial dissolution-precipitation mechanisms need not be mutually exclusive — Maher et al. developed a framework that described mineral dissolution proceeding through formation of a leached layer and newly precipitated amorphous layer on top of the leached layer [99]. Further analysis of the surfaces through transmission electron microscopy is required to clarify this point.

XPS of the fayalite slag surface is shown in Figure 3-10. The oxidation state of iron pre-dissolution is shown as a function of depth into the surface in Figure 3-10A and the effect of exposure to NaOH is shown in Figure 3-10B. In both cases, argon

milling into the surface successively removes surface material allowing the oxidation state of Fe beneath the surface to be revealed. In Figure 3-10A, deeper milling reveals a transition from Fe(III), characteristic of an oxidized surface layer, to Fe(II), characteristic of bulk fayalite. The intensities of the $Fe2p_{1/2}$ and $Fe2p_{3/2}$ shift from Fe(III) binding energies (710.8 eV in hematite) to lower binding energies associated with Fe(II) bonding (709.5 eV in wüstite) [100]. Similar shifts are seen in the satellite peaks of $Fe2p_{1/2}$ and $Fe2p_{3/2}$ as a function of depth. Figure 3-10B shows the XPS spectra of fayalite slag pre-dissolution, and fayalite slag after 7 days of NaOH exposure as a function of depth into the material. Post exposure to NaOH, $Fe2p_{1/2}$ and $Fe2p_{3/2}$ peaks shift to the left, indicating more Fe(III) bonding. This is understood to be due to the precipitation of goethite (Fe(III)O(OH)), which precipitates at very low Fe concentrations in basic solution. Argon milling of the NaOH exposed surface results in a shift back towards Fe(II) bonding, characteristic of bulk fayalite. The presence of an Fe(III) oxidized surface, in combination with a rapidly precipitating Fe hydroxide surface layer in basic solutions, results in a surface that has little resemblance to that of bulk fayalite. This difference manifests itself in a different dissolution rate dependence on pH than that of γ-C_2S. The formation of iron-containing precipitates on the surface of iron-bearing olivines has been identified previously. Comparing rates of dissolution of Mg_2SiO_4 with $Mg_{1.8}Fe_{0.2}SiO_4$, Golubev found the dissolution rate of the iron containing mineral to be an order of magnitude slower which was attributed to precipitation of Fe(III) containing phases at the surface of the dissolving mineral [101]. Schott and Berner described cation depletion at the surface of fayalite in oxic and anoxic acidic solution [102, 103]. In anoxic conditions, XPS revealed the surface to be deficient in iron after 30 days of exposure to pH 6 solution due to ion exchange of H^+ ions for Fe^{2+} ions in the crystal structure. Under oxic conditions, the surface appeared to be enriched in iron.

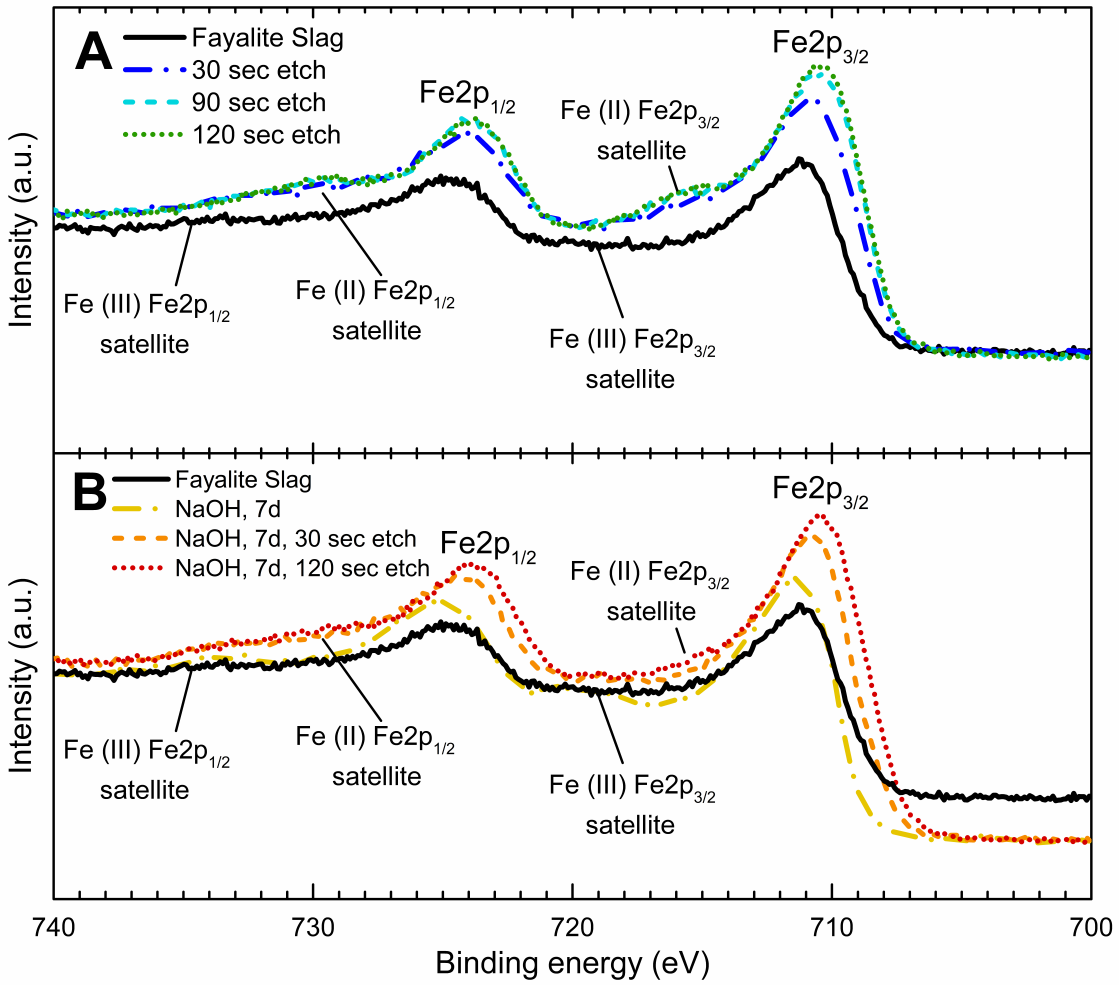

Figure 3-10: X-ray photoelectron spectra of $Fe2p_{1/2}$ and $Fe2p_{3/2}$ binding energies of fayalite slag surface. A: Argon milling into fayalite slag. B: Argon milling into fayalite slag following exposure to NaOH for 7 days.

3.5 Chapter Summary

Quantifying the rates of dissolution of ladle furnace steel slag and copper slag as a function of their aqueous environment offers insight into their expected reactivity in conventional or alternative concrete. Here, we quantify the reactivity of these slags through kinetic studies of their major phases from the olivine mineral group - γ-C_2S and fayalite. γ-C_2S dissolution rates decreased with increasing pH, while fayalite dissolution rates increased with increasing pH. The reasons for the differing behavior was attributed to differences in the surface layers of the two minerals. γ-C_2S developed

a Si-rich surface layer which did not inhibit the overall dissolution. In contrast, an oxidized Fe(III) surface pre-dissolution combined with an iron hydroxide precipitate formed during dissolution to alter the form of the dependence of dissolution rate on pH.

These results have strategic implications for the re-use of steel slags with high γ-C_2S contents and fayalitic copper slags in concrete systems. One typical strategy to increase the dissolution rate of precursors in such systems is raising the pH of the aqueous phase of the binder, a process normally achieved through alkali activation. However, alkali activation of steel slags where γ-C_2S is the major phase will not improve the reactivity of the overall slag. Similarly, alkali activation of fayalitic copper slags will improve the reactivity of the slag but iron hydroxide will precipitate more quickly at higher pH, and gains in reactivity are unlikely to be sufficient to justify the use of an alkali activator. It is also worth acknowledging the absolute dissolution rates of these phases – γ-C_2S dissolved several orders of magnitude more quickly than fayalite, despite its pH dependence. Improving our understanding of the reactivity of the major crystalline phases of alternative SCMs provides insight into strategies to derive benefit from their use.

3.6 Acknowledgments

I would like to acknowledge financial support for this research, without which none of this would have been possible. I would like to thank the Environmental Solutions Initiative, Massachusetts Institute of Technology, Cambridge. I also acknowledge support from NSF CAREER #1751925. This work made use of the MRSEC Shared Experimental Facilities at MIT, supported by the National Science Foundation under award number DMR-1419807, and facilities at the Institute for Soldier Nanotechnologies (ISN) at MIT. This work was performed in part at the Harvard University Center for Nanoscale Systems (CNS), a member of the National Nanotechnology Coordinated Infrastructure Network (NNCI), which is supported by the National Science Foundation under NSF award no. 1541959. I also gratefully acknowledge Hindalco

Industries for supplying the copper slag used in this study.

Chapter 4

Reaction product formation on mineral surfaces

This chapter explores the effect of aggregate surface chemistry on the type, morphology, and rate of reaction product formation in Portland cement-type systems. Reaction product formation on the surface of an aggregate plays a crucial role in the development of hardened, load-bearing concrete. Surfaces of limestone, quartz, fayalite, and diopside were polished and then exposed to Ca and Si rich solutions and the resultant reaction products were characterized using SEM. Experiments were designed to ensure that the only variable between experiments is the composition of the aggregate surface. The key results of this study indicate that C-S-H nucleation and growth kinetics are accelerated on limestone surfaces relative to quartz, fayalite, and diopside surfaces, although no differences in the morphology of the precipitated C-S-H is observed. In the case of static solution experiments, there were no differences in reaction product type, morphology, or kinetics among any of the 4 surfaces of interest. Flow reactor experiments allowed for more controlled and protracted reaction product formation, and revealed the accelerating affect of limestone surfaces but again showed no differences in the type or morphology of reaction product. The results of this study have implications for concretes which incorporate limestone, quartz, fayalite, or diopside containing aggregates, with a particular importance identified for the kinetics of the nucleation and growth of C-S-H on limestone surfaces.

4.1 Background

Steel and copper slags are composed primarily of crystalline phases which are not reactive [29]. While these phases may not be suitable as direct substitutes for Portland cement, they possess physical properties which make them suitable for use as aggregates [29]. Additionally, steel and copper slags are composed of crystalline phases (such as olivines and pyroxenes) that are more reactive than traditional aggregates (such as quartz).

The interfacial transition zone (ITZ) is the region in concrete between the hydrated cement particles and the aggregate [56]. The ITZ is defined by fewer cement grains due to the poor packing in the vicinity of the aggregate surface. The ITZ has higher porosity which has a major influence on the mechanical properties of the concrete due to the tendency for cracks to form in this region of the concrete. The chemical properties of the aggregate surface influences reaction product formation at the aggregate surface and, subsequently, the mechanical properties of the ITZ. There are both physical and chemical properties of the aggregate surface which may influence reaction product formation. Physical properties encompass the roughness of the surface, which may promote heterogeneous nucleation, and space constraints due to the packing of aggregate and cement particles, which may limit the growth of reaction product grains. There are chemical properties of the aggregate surface which may influence reaction product formation: (1) dissolution rate of the aggregate and; (2) propensity for ion adsorption onto the aggregate surface leading to precipitation of reaction products, also known as "templating". In the case of (1), the reaction products forming at the surface of the aggregate may be chemically different due to the presence of an aqueous ion which may not otherwise be present in the dissolving cement. In the case of (2), the morphology or extent of reaction product formation may be different due to the influence of the surface in promoting epitaxial growth, or due to faster nucleation on the surface accelerated by preferential bonding of reaction products with the surface [55]. These 2 effects are discussed in the following paragraphs.

An aggregate with a higher dissolution rate will have a higher concentration of aqueous ions in the vicinity of the aggregate surface than a corresponding aggregate with a slow dissolution rate. Higher concentrations of ions is more likely to result in precipitation of reaction products. In OPC systems with inert aggregates, there is initially a high concentration of Ca^{2+} ions close to the aggregate surface due to rapid release and diffusion of Ca^{2+} ions from cement grains towards aggregate surfaces. The high concentration of Ca^{2+} leads to formation of portlandite at the aggregate surface. However, in the presence of a more reactive silicate aggregate, the dissolution of the aggregate and availability of aqueous Si may result in the formation of calcium silicate hydrate (C-S-H) being favored over the formation of portlandite. The formation of C-S-H in this scenario can lead to a denser microstructure in the ITZ. This phenomenon is not well-studied. Nie et al. studied the effect of a pozzolanic reaction involving lighweight fine aggregate (LWFA) on the nucleation and growth of hydration products [57]. Hydration products in the vicinity of the LWFA were observed to be different from bulk reaction products. C-S-H and C-A-S-H reaction products were identified as having formed due to the partial dissolution of the aluminosilicate LWFA.

An aggregate surface may also promote reaction product formation through preferential adsorption of aqueous ions. Preferential adsorption of aqueous ions onto a surface can serve as a precursor step in the precipitation of a reaction product. Ca^{2+} has a higher affinity for adsorbing onto calcite surface than SO_4^{2-}. Pourchet et al. observed 7-fold greater adsorption capacity of Ca^{2+} over SO_4^{2-} onto calcite [104]. The greater affinity of Ca^{2+} is corroborated by experimental observations of Ca^{2+} being the potential determining ion for calcite surfaces [105]. Ouyang et al. studied the adhesion mechanisms between C-S-H and limestone or quartz fillers [55]. They concluded that the chemically adsorbed Ca^{2+} on the calcite surface interacts strongly through ionic-covalent bonds with the C-S-H lamellae. This results in a strong bond between the calcite surface and the C-S-H lamellae. This stronger bonding is manifested in a higher number of C-S-H nuclei on limestone surfaces than on quartz surfaces, as observed by scanning electron microscopy.

In spite of these previous studies, the role of surface chemistry on the the rate and

types of reaction products formed at the surface is poorly studied. In previous studies, reaction product formation has been tracked in mortar systems for which physical properties of the aggregate surfaces, i.e. surface roughness and space constraints, also play a role. Additionally, these studies have not extended beyond limestone, quartz, and aluminosilicate phases [55, 57].

Therefore, this study seeks to examine the role of surface chemistry in reaction product formation on limestone, quartz, fayalite, and diopside surfaces. Limestone and quartz surfaces are of interest due to their ubiquity as aggregates in incumbent concretes. Fayalite and diopside are of interest as major components of copper and steel slags. The motivation for using of steel and copper slags in concrete is discussed in Chapter 1. The two research questions of this study are;

- Can we design an experiment to study the influence of aggregate surface **chemistry** on the type, extent, and morphology of reaction products?
- How does the surface chemistry influence the type, morphology, and kinetics of reaction product formation on limestone, quartz, diopside, and fayalite surfaces?

The chemistry of Portland cement systems is dominated by Ca and Si and C-S-H is the dominant reaction product. For this reason, the systems studied here are limited to solutions of Ca and Si. This allows C-S-H formation to be easily identified using microscopy without the complication of minor reaction products. Throughout this study, "reaction products" and "C-S-H" are therefore effectively interchangeable.

4.2 Experimental Methods

Distinguishing surface hydration products of different type and morphology in a mortar is challenging. This is due to the microscopic and spectroscopic limitations in characterizing hydration products precipitated on surfaces of the length scales required (10 nm - 100 μm). These challenges are compounded in mortar systems in which destructive sawing, casting, and polishing is often required. Furthermore, variability in the particle size, composition, and morphology of precursor cement and

aggregate can lead to local variations in the observed hydration products. This study aims to isolate the influence of mineral surface chemistry on C-S-H precipitation by addressing the aforementioned sources of variability. To do this, we polish mineral surfaces and expose them to prepared Ca and Si solutions with known concentrations. By polishing the mineral surfaces, we remove the influence of surface morphology on the precipitation rate. By using solutions of known concentration, we remove the potential for variability in concentration of the pore solution in contact with the mineral. This experimental design ensures that the only variable between experiments is the composition of the aggregate surface. The concentrations of Ca and Si in the solution were chosen to mimic the concentrations of these elements in hydrated Portland cement pore solutions [106].

4.2.1 Materials

Four mineral surfaces were investigated; limestone, quartz, diopside, and fayalite. Limestone, quartz, and diopside chunks of natural origin were purchased from Ward's Scientific. A fayalite copper slag was used as the primary fayalite surface (source: Hindalco Industries, Mumbai, India).

4.2.2 Sample preparation

In order to investigate reaction product formation on the surfaces of these materials, polished surfaces were created. Mineral chunks were initially sawed using a diamond band saw to make a roughly flat surface. The sawed chunks were then cast in epoxy (EpoThin 2 resin and hardener, Buehler). The mounted samples were ground using 12 μm grit SiC grinding paper until enough epoxy had been removed such that the mineral surface was exposed. The surfaces were then polished using TexMet C (JH Technologies) polishing cloths and oil-based diamond suspensions on an auto-polisher with a disc speed of 150 s^{-1} and a head speed of 60 s^{-1}. Surfaces were polished at 15 N for 20 minutes using 9 μm diamond suspension, 20 N for 20 minutes using 3 μm diamond suspension, and 25 N for 20 minutes using 1 μm diamond suspension.

Surfaces were sonicated for 5 minutes in isopropanol between each polishing step.

The polished surfaces were exposed to Ca and Si solutions using 2 experimental set-ups, a static solution set-up and a flow reactor set-up, described below. For reaction product formation in static solutions, the experiments were performed under N_2 atmosphere in a glove box to limit the formation of carbonates. Solutions of $Ca(OH)_2$ were prepared using $Ca(OH)_2$ (98% purity, Acros Organics) and deionized (DI) water. Solutions of sodium silicate were prepared using $Na_2SiO_3.5H_2O$ (crystalline/technical, Fisher Chemical). Polished samples were positioned inside 1.125" diameter silicone mold cups (Electron Microscopy Sciences). The polished sample surfaces were exposed to 2 different solutions; 15 mM $Ca(OH)_2$ solutions, and a mixture of 9 parts 15 mM $Ca(OH)_2$ solution with 1 part 1 mM or 10 mM $Na_2SiO_3.5H_2O$ solution (referred to here as the "mixed solution"). The concentrations of Ca and Si in the solution were chosen to mimic the concentrations of these elements in hydrated Portland cement pore solutions [106]. Immediately prior to deposition on the polished surface, the solution of interest was filtered through a 0.2 μm disposable filter. In the case of the mixed solution, filtration followed immediately after the mixing of the 2 solutions. 10 μL of solution was then deposited onto the polished surface within 1 minute of the 2 solutions being initially mixed together using a precision pipette. A small amount of DI water was added to the bottom of the mold cup, which was then sealed in Parafilm to provide a high humidity environment and prevent evaporation of the deposited 10 μL drop. After a specified interval of time, the sample was removed from the mold cup, immersed in isopropanol, and agitated gently to stop the reaction. The sample was then dried gently with compressed air. For SEM analysis, the sample was immediately coated in 10 nm Au. SEM imaging was performed on a Zeiss Merlin High Resolution Scanning Electron Microscope.

For reaction product formation in flowing solutions, experiments were performed in a 3D printed, mixed flow reactor. A schematic of the flow reactor is shown in Figure 4-1. The key design features of this flow reactor include; 2 input barbs in the reactor cap to allow 2 solution inputs, 2 output tubing barbs in the reactor to remove solution, a suspended stirrer and stir mount to ensure a well-mixed reactor, and a wire

mesh to hold the polished surfaces in place without interrupting the flow of solution. This experimental set-up allowed $Ca(OH)_2$ and $Na_2SiO_3.5H_2O$ solutions to be flowed over the polished surfaces, thereby maintaining a constant C-S-H supersaturation in the solution. In contrast to the static solution, this experimental set-up prevents the depletion of Ca and Si in solution. Flow rates of 10 mL min^{-1} were used for both inputs for all experiments. An IPC-N 8 channel peristaltic pump (Ismatec) was used for pumping the solutions. $Ca(OH)_2$ solutions were passed through a 0.2 μm disposable filter immediately prior to the beginning of the experiment.

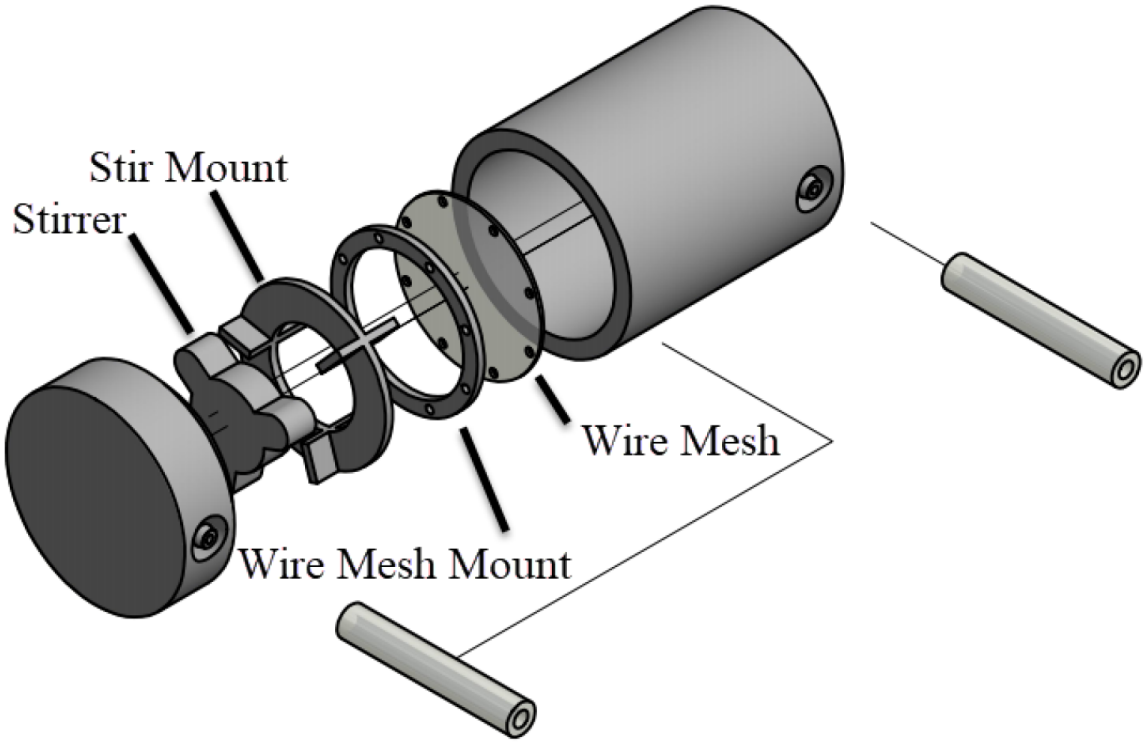

Figure 4-1: Exploded schematic of flow reactor components.

4.3 Results and Discussion

4.3.1 Static solution

In all cases, observed reaction products may be formed from; precipitation of the aqueous ions in the prepared solutions, dissolution of the mineral surface and re-precipitation of the dissolved ions, or precipitation due to the interaction between

aqueous ions in the prepared solutions and ions dissolved from the mineral surfaces.

Exposure to the mixed solution in the static solution setup did not result in a significant difference in either the extent nor type of reaction product formation on limestone and quartz surfaces. The similarity in the extent of reaction product formation between the 2 surfaces is illustrated in Figure 4-2A (limestone) and 4-2C (quartz) at low SEM magnification (x1,000). The percentage of the surfaces covered by reaction products was calculated using ImageJ. Surface coverage was calculated in ImageJ using the 'Find Edges' routine, converting the image to binary, and adjusting the binary threshold such that all reaction products were represented by white pixels and the mineral surface was represented by black pixels. Following this procedure the average surface area covered by reaction products was estimated to be 33.1±2% for limestone and 32.5±3% for quartz. Averages are based on 6 images of each surface and uncertainties are based on the standard deviation of the 6 images. High magnification (x20,000) images of the surfaces reveal the presence of 2 main reaction products. The first of these consists of hexagonal plates, recognised as portlandite [107, 108]. The origin of this portlandite is most likely the 15 mM $Ca(OH)_2$ starting solution in which portlandite crystals are already present prior to the experiment. These crystals most likely pass through the 0.2 μm pore size filter. The second reaction product is more abundant than the portlandite and has a globular morphology. This reaction product is not seen on surfaces exposed to only $Ca(OH)_2$. On the basis of the available aqueous ions and the high supersaturation with respect to C-S-H precipitation in solution, this reaction product is understood to be C-S-H. The presence of this reaction product on both limestone and quartz surfaces in equal quantities lends further credence to this assumption. Observed C-S-H morphologies are typically one of; reticular/honeycomb shaped [109, 110, 111, 112], or needle-like [109, 113, 58, 110, 111]. Globular C-S-H has also been observed, however [110, 114]. There does not yet exist a clear correlation between solution conditions and C-S-H morphology, and it is unclear why the C-S-H in these images possesses a globular morphology, although it may be related to homogeneous C-S-H nucleation (discussed further below).

Surfaces exposed to only $Ca(OH)_2$ solution were also imaged. Limestone surfaces

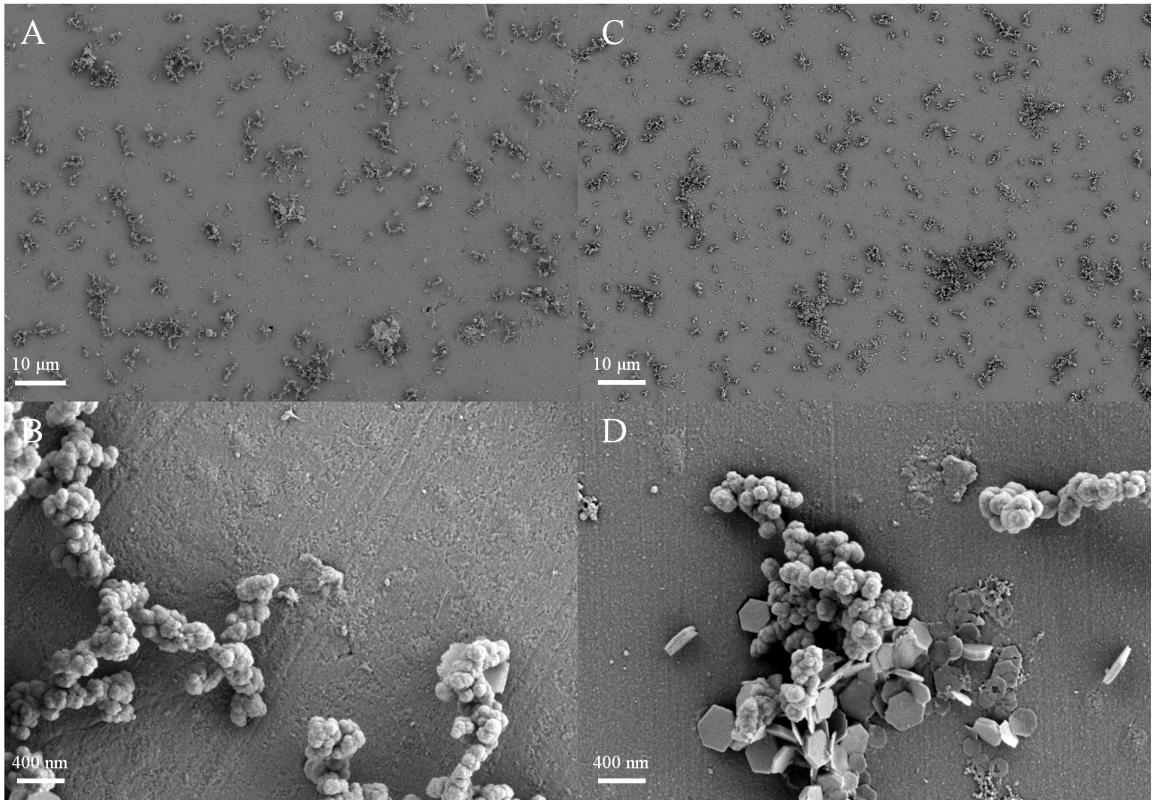

Figure 4-2: Static solution SEM images of reaction products on limestone at low magnification (A), limestone at high magnification (B), quartz at low magnification (C), and quartz at high magnification (D). Surfaces were exposed to a solution of 15 mM $Ca(OH)_2$ and 0.1 mM $Na_2SiO_3.5H_2O$ for 60 minutes.

showed 2 reaction products. The first of these has a rhombohedral morphology that is attributable to portlandite [107, 108]. The second reaction product consists of a large number of finger-like crystals. This reaction product is most likely calcium carbonate. Calcium carbonates with very similar morphology have been reported by [115, 116]. Additionally, this reaction product was observed on the majority of limestone surfaces, but never on quartz surfaces. It stands to reason that the reactivity of the limestone surface results in the liberation of carbonate ions into solution which react with aqueous Ca and precipitate on the surface in the form of aragonite or calcite. In fact, the dissolution rates of limestone, quartz, fayalite, and diopside at pH 13 can be estimated to be approximately 10^{-10} mol cm^{-2} s^{-1}, [117], 10^{-14} mol cm^{-2} s^{-1} [118], 10^{-15} mol cm^{-2} s^{-1} [119, 101, 120, 121], and 10^{-13} mol cm^{-2} s^{-1} [62], respectively. The limestone dissolution rate is 3 orders of magnitude more

rapid than the next fastest dissolution rate and, in this context, the formation of additional reaction products unique to limestone is unsurprising. Quartz surfaces only show evidence of portlandite crystals. The surface is largely unchanged relative to its appearance pre-exposure, and nanometer sized grooves from polishing are still visible.

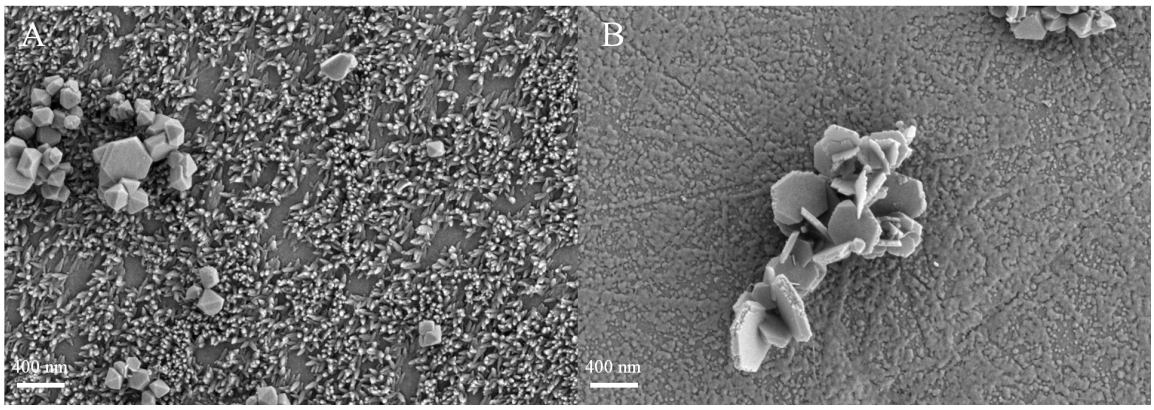

Figure 4-3: Static solution SEM images (x20,000 magnification) of limestone (A) and quartz (B) surfaces exposed to 15 mM $Ca(OH)_2$ for 60 minutes.

The absence of any difference in the type or extent of reaction products between the limestone and quartz surfaces exposed to the same mixed solution (15 mM $Ca(OH)_2$ and 0.1 mM $Na_2SiO_3.5H_2O$ for 60 minutes (Figure 4-2)) does not correspond with the results of Ouyang et al., who observed a greater number of C-S-H nuclei on limestone surfaces than on quartz surfaces [55]. This implies that the surface in these experiments is not driving the precipitation of the reaction products in our experiments. This may be due to the fact that the reaction products are undergoing homogeneous nucleation in solution. This would also serve to explain the unusual globular morphology of the C-S-H, which stands in contrast to typical C-S-H morphologies. Alternatively, precipitation may occur faster on limestone surfaces but 60 minutes is sufficient time for the reaction to run to completion and the concentration of ions to reach an equilibrium, regardless of which surface is present. In any case, the identical behavior of the limestone and quartz surfaces implies that differences in surface chemistry are not being investigated in this experimental setup. For this reason, fayalite and diopside surfaces are not investigated using the static solution

experimental design.

Other observed products

Other reaction product were observed on limestone and quartz surfaces using the static solution setup, and 4 notable examples are compiled in Figure 4-4. These surfaces were exposed to different solutions for varying lengths of time and are not necessarily representative of the whole surface. They are not included for comparative purposes and are included rather as a point of reference and to highlight some of the more frequently encountered reaction products with interesting morphologies. Figure 4-4A, 4-4B, and 4-4D, show what appears to be the same reaction product at increasing extent of formation. The morphology of the reaction product in each of these images closely matches an increasing extent of C-S-H formation with honeycomb morphology, as reported by [109, 110, 111, 112]. C-S-H with a honeycomb morphology is also known as Type 2 C-S-H [109]. The greater extent of C-S-H formation is due to the availability of a greater quantity of aqueous ions in solution. In the case of Figure 4-4A this is due to a higher $Na_2SiO_3.5H_2O$ concentration in solution. In the case of Figure 4-4B, this is due to the solution being un-filtered and a greater quantity of portlandite available to supply Ca ions into solution. For Figure 4-4D, the solution has both a higher $Na_2SiO_3.5H_2O$ concentration and is unfiltered. Figure 4-4C shows a limestone surface exposed to un-filtered 15 mM $Ca(OH)_2$ and 1 mM $Na_2SiO_3.5H_2O$ for 30 minutes. The reaction product in this image shows a needle- or finger-like, dense, reaction product. This reaction product was only observed on limestone surfaces that had been exposed to a solution with a high Ca/Si ratio. Quartz surfaces exposed to the same solution did not show this reaction product. Furthermore, reductions in the concentration of Ca in the solution resulted in only the dense, honeycomb reaction product being formed. Given the criteria under which this reaction product forms, it is suggested here that this is C-S-H which precipitates on and grows outward from the carbonate fingers described in Figure 4-3A. C-S-H with this morphology has previously been reported by [109, 113, 58, 110, 111]. He et al. investigated the effect of C-S-H morphology on Ca/Si ratio and reported a

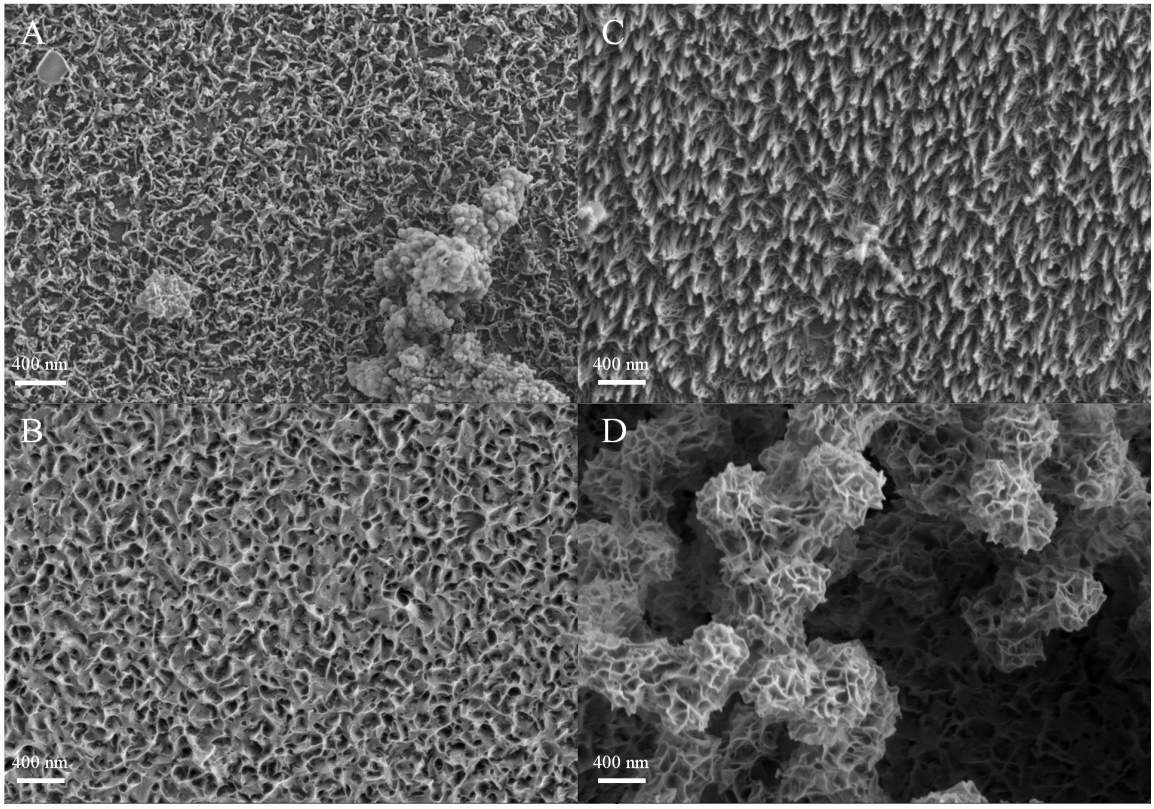

Figure 4-4: Static solution SEM images of reaction products on (A) quartz surface exposed to 15 mM $Ca(OH)_2$ and 1 mM $Na_2SiO_3.5H_2O$ for 60 minutes, (B) limestone surface exposed to un-filtered 15 mM $Ca(OH)_2$ and 0.1 mM $Na_2SiO_3.5H_2O$ for 30 minutes, (C) limestone surface exposed to un-filtered 15 mM $Ca(OH)_2$ and 1 mM $Na_2SiO_3.5H_2O$ for 30 minutes, and (D) limestone surface exposed to 15 mM $Ca(OH)_2$ and 1 mM $Na_2SiO_3.5H_2O$ for 60 minutes.

fibrous C-S-H morphology at higher Ca/Si ratios and sheet-like morphology at lower Ca/Si ratios [113], broadly in agreement with the results presented here. C-S-H with a needle-like morphology is also known as Type 1 C-S-H [109].

4.3.2 Flow reactor

In contrast to the static solutions, surfaces in a flow reactor are exposed to a solution of constant Ca and Si concentration. This prevents the solution from reaching equilibrium over the course of the experiment, as was hypothesized to have occurred in Section 4.3.1. Figures 4-5 to 4-8 illustrate the evolution of limestone, fayalite, diopside, and quartz surfaces when exposed to a solution 13.5 mM $Ca(OH)_2$ and

150 μM $Na_2SiO_3.5H_2O$ (A-B) or a solution of 27 mM $Ca(OH)_2$ (C-D). A few key points merit discussion. First, for surfaces exposed to 13.5 mM $Ca(OH)_2$ and 150 μM $Na_2SiO_3.5H_2O$, limestone shows the greatest extent of reaction product formation at 60 minutes and 180 minutes. Limestone surfaces show a partial but extensive coverage of C-S-H at 60 minutes which gives way to a much denser honeycomb C-S-H at 180 minutes. Fayalite, diopside, and quartz surfaces show nuclei of an unknown reaction product, likely C-S-H, particularly at 180 minutes. Second, portlandite crystals are frequently observed on all surfaces due to their presence in the $Ca(OH)_2$ solutions. A higher number of portlandite crystals in a given image is not representative of the entire surface - portlandite crystals may cluster together and be randomly deposited in greater concentrations in a given location on the surface. Third, surfaces exposed to 27 mM $Ca(OH)_2$ (C-D) show no evidence of reaction product formation. Limestone surfaces appear to have undergone partial dissolution, evidenced by slight etching around the polishing grooves.

Given the lack of extensive reaction product formation on the surfaces of fayalite, diospide, and quartz, limestone and quartz surfaces were exposed to a mixed solution with a higher Si concentration. This provides a solution which is more strongly supersaturated solution with respect to C-S-H, which resulted in a greater extent of C-S-H formation. This is illustrated for limestone surfaces and quartz surfaces in Figures 4-9 and 4-10 respectively. Limestone surface show a greater a greater extent of C-S-H formation at all time-points, although there is no difference in the morphology of the C-S-H. Fayalite and diopside surfaces showed similar extent of reaction to quartz and are not shown here.

The experiments performed using the flow reactor demonstrate no significant differences in the type or morphology of C-S-H on the surfaces at equivalent times. However, clear differences in the kinetics of C-S-H nucleation and growth were observed amongst the 4 surfaces of interest: C-S-H nucleation and growth is more rapid on limestone than on quartz, fayalite, or diopside. No significant difference in the rate of nucleation and growth of C-S-H was identified among quartz, fayalite, and diopside. Measurements of the rates of nucleation and growth of C-S-H on these

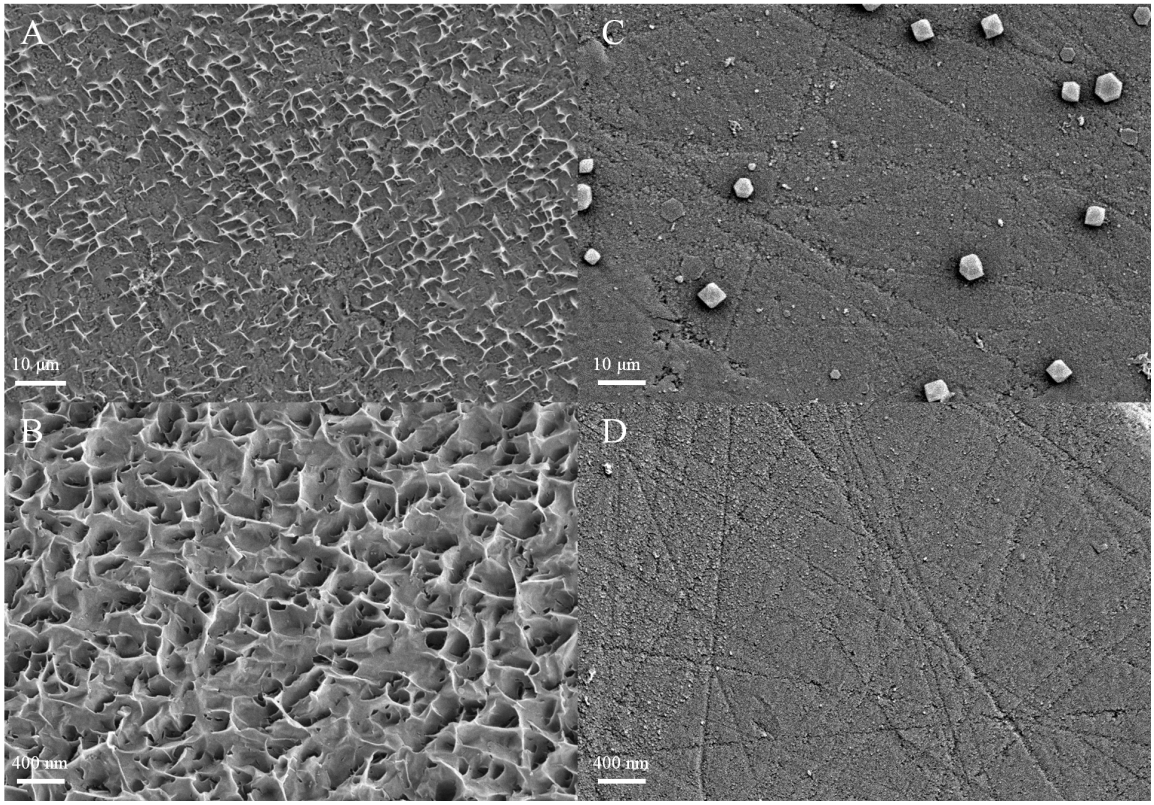

Figure 4-5: Flow reactor SEM images of limestone surfaces exposed to; (A) 13.5 mM $Ca(OH)_2$ and 150 μM $Na_2SiO_3.5H_2O$ for 60 minutes, (B) 13.5 mM $Ca(OH)_2$ and 150 μM $Na_2SiO_3.5H_2O$ for 180 minutes, (C) 27 mM $Ca(OH)_2$ for for 60 minutes, or (D) 27 mM $Ca(OH)_2$ for for 180 minutes.

surfaces represents an important direction for future work given the importance of C-S-H nucleation and growth on the properties of a binder.

The reasons for the greater extent of C-S-H formation on limestone are not known. As described in Section 4.1, the dissolution rate of the aggregate surface can influence reaction product formation. The dissolution rate of limestone, quartz, fayalite, and diopside at pH 13 can be estimated to be approximately 10^{-10} mol cm^{-2} s^{-1}, [117], 10^{-14} mol cm^{-2} s^{-1} [118], 10^{-15} mol cm^{-2} s^{-1} [119, 101, 120, 121], and 10^{-13} mol cm^{-2} s^{-1} [62], respectively. The higher dissolution rate of limestone surfaces was evident in the formation of $CaCO_3$ when exposed to $Ca(OH)_2$ solutions. In the case of the static solutions, this $CaCO_3$ appeared to result in C-S-H with a morphology different from the other surfaces. The constant replenishment of aqueous ions in the flow reactor more closely resembles the pore solution of concrete in which the precursors are

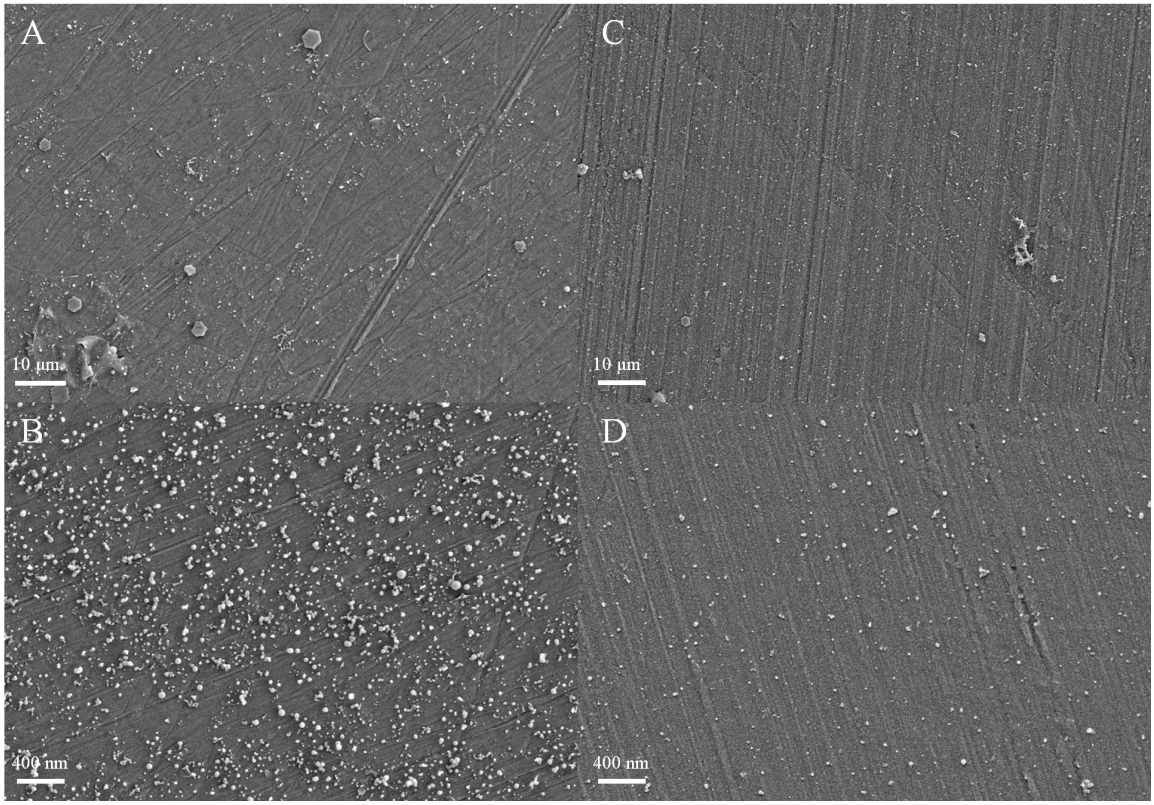

Figure 4-6: Flow reactor SEM images of fayalite surfaces exposed to; (A) 13.5 mM $Ca(OH)_2$ and 150 μM $Na_2SiO_3.5H_2O$ for 60 minutes, (B) 13.5 mM $Ca(OH)_2$ and 150 μM $Na_2SiO_3.5H_2O$ for 180 minutes, (C) 27 mM $Ca(OH)_2$ for for 60 minutes, or (D) 27 mM $Ca(OH)_2$ for for 180 minutes.

continually dissolving, and the differences among the surfaces observed in the static solutions are not anticipated to be relevant to real cement systems. Understanding the role of surface adsorption in the acceleration of C-S-H nucleation and growth on limestone surfaces is also an important direction for future work. It is hypothesized that the faster C-S-H nucleation and growth rates on limestone surfaces observed here are due to either preferential ion adsorption or faster surface dissolution rates.

4.4 Chapter Summary

This chapter investigates the influence of surface chemistry on the morphology and extent and of C-S-H formation. In short, the key finding of this chapter is that C-S-H nucleation and growth kinetics are accelerated on limestone surfaces relative to

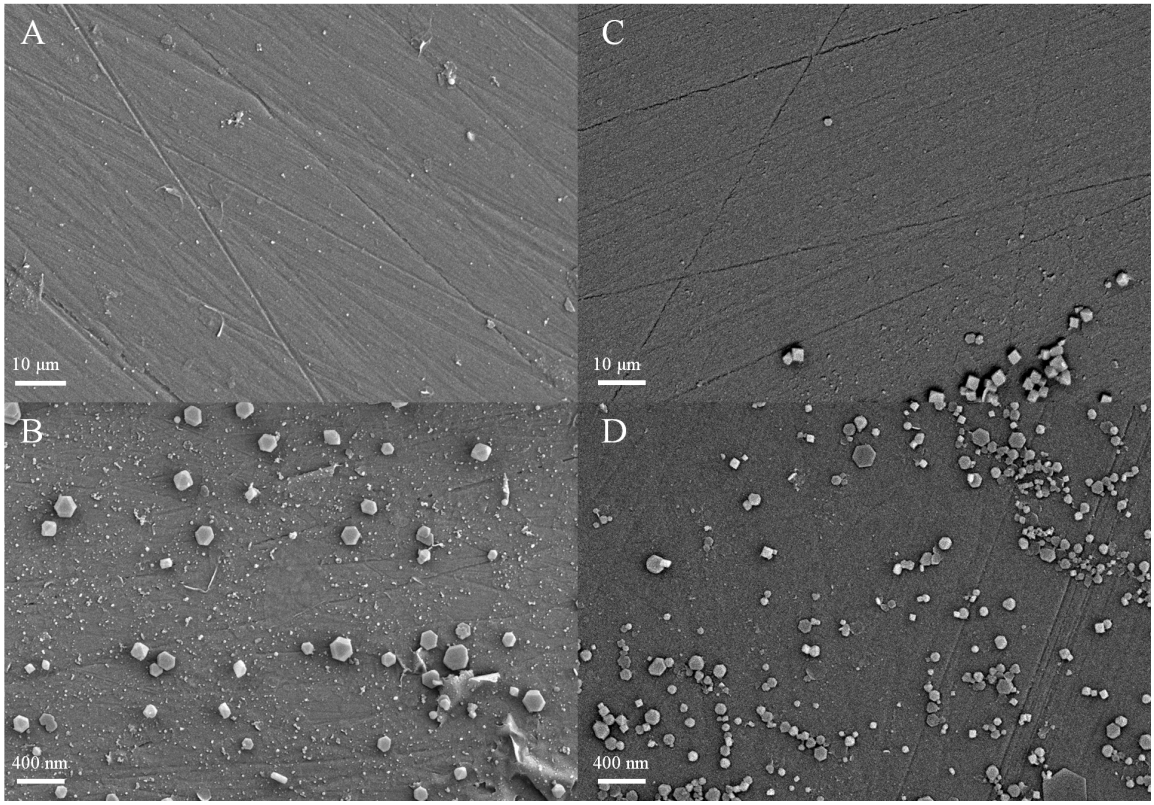

Figure 4-7: Flow reactor SEM images of diopside surfaces exposed to; (A) 13.5 mM $Ca(OH)_2$ and 150 μM $Na_2SiO_3.5H_2O$ for 60 minutes, (B) 13.5 mM $Ca(OH)_2$ and 150 μM $Na_2SiO_3.5H_2O$ for 180 minutes, (C) 27 mM $Ca(OH)_2$ for for 60 minutes, or (D) 27 mM $Ca(OH)_2$ for for 180 minutes.

quartz, fayalite, and diopside surfaces, although no differences in the morphology of the precipitated C-S-H is observed. These finding are important in the context of the formation of the ITZ: the type, morphology, and extent of the reaction products formed can influence the mechanical properties of the ITZ. In the context of using slags with high fayalite or diopside contents, these particular phases function in the same way as quartz - they have no observable influence on the type, morphology, or rate of reaction product formation.

Two experiment designs were used to study the influence of aggregate surface chemistry on the type, extent, and morphology of reaction products. The flow reactor was found to offer a better comparison of the reaction kinetics than the static solution setup. The constant replenishment of aqueous ions in the flow reactor setup more closely resembles the pore solution of concrete in which the precursors are contin-

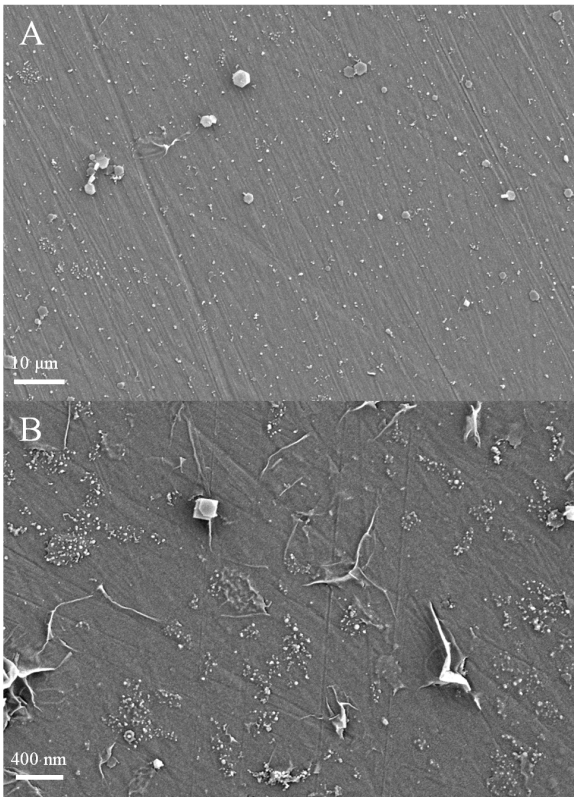

Figure 4-8: Flow reactor SEM images of quartz surfaces exposed to; (A) 13.5 mM $Ca(OH)_2$ and 150 μM $Na_2SiO_3.5H_2O$ for 60 minutes, (B) 13.5 mM $Ca(OH)_2$ and 150 μM $Na_2SiO_3.5H_2O$ for 180 minutes.

ually dissolving. Furthermore, the similarities between surfaces in the static solution experiments implies that the surface is not driving the precipitation of the reaction products in that setup. From the flow reactor experiments, it was concluded that the nucleation and growth of C-S-H was accelerated on limestone surfaces relative to quartz, fayalite, and diopside surfaces. It is hypothesized that the faster C-S-H nucleation and growth rates on limestone surfaces observed here are due to one of: preferential adsorption of Ca^{+2} ions which leads to more nucleation sites from which C-S-H nuclei can grow; faster surface dissolution rates which contribute to greater availability of aqueous ions in the vicinity of the surface; or a combination of both.

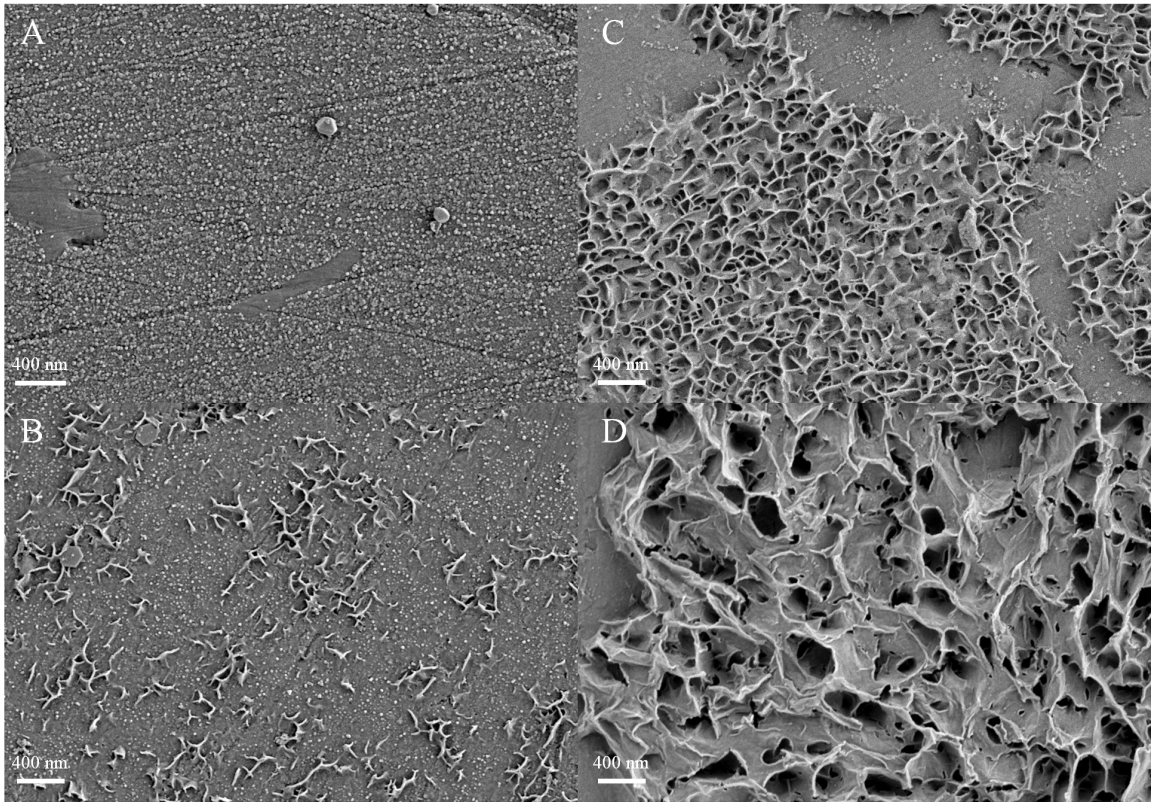

Figure 4-9: Flow reactor SEM images of limestone surfaces exposed to 13.5 mM $Ca(OH)_2$ and 200 μM $Na_2SiO_3.5H_2O$ for (A) 20 minutes, (B) 40 minutes, (C) 60 minutes, and (D) 180 minutes.

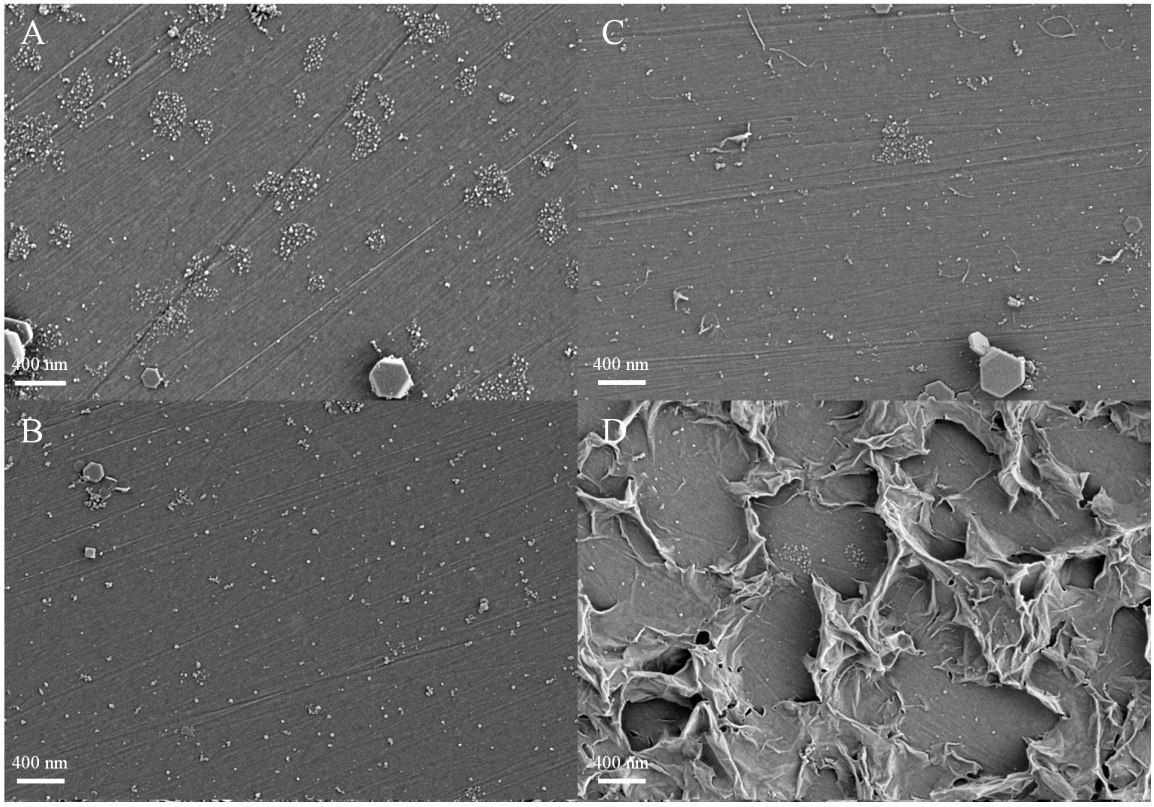

Figure 4-10: Flow reactor SEM images of quartz surfaces exposed to 13.5 mM $Ca(OH)_2$ and 200 μM $Na_2SiO_3.5H_2O$ for (A) 20 minutes, (B) 40 minutes, (C) 60 minutes, and (D) 180 minutes.

Chapter 5

Framework for concrete mix design using crystalline slags

In this chapter, a framework for rational concrete mix design incorporating Portland cement and complex crystalline slags is proposed. The phase composition and microstructure of steel and copper slags are reviewed, resulting in the most comprehensive compilation of the composition of these complex materials. Dissolution rates for all relevant phases at pH 13 are determined using various strategies. In combination with an empirical hydration model for Portland cement hydration, a kinetic model for steel slag consumption based on dissolution rates is used to simulate the kinetics of dissolution of a blended Portland cement-steel slag binder. The quantities of Portland cement and steel slag consumed at various binder ages are used as inputs into thermodynamic simulations in which the reaction product assemblage of the system is determined. A case study on a 20 wt% steel slag, 80 wt% Portland cement binder shows the preferential formation of AFm-phases over ettringite at later binder ages, due to the presence of excess Al_2O_3 in the binder. The binder is redesigned to incorporate additional gypsum: the presence of gypsum returns increases the quantity of ettringite formed relative to AFm-phases. The implications of this model in predicting the mechanical properties of the binder through the porosity of the binder is discussed. This model represents an important first step in the development of a flexible model for steel slag concrete mix design.

5.1 Introduction

The variability in steel slags is a challenge to their use in concrete. Case-by-case studies of steel slag use in concrete have made progress in understanding how the properties steel slags translate to the performance of the concrete in which they are used. A model that describes the evolution of the microstructure and reaction products of a concrete based only the input materials to the concrete would represent a powerful tool, allowing for rapid and flexible concrete mix design. A prerequisite of a model of this kind would be information about the constituent phases of the input materials as well as the kinetics of dissolution of those phases.

However, the dissolution rate of the input materials is not the only process that determines the evolution of the concrete. If the solution into which a phase is dissolving is saturated with respect to that phase, dissolution will not occur. This scenario arises when the rate of consumption of aqueous ions is slower than the rate of dissolution. There are two processes which hinder the consumption of aqueous ions and cause a saturated solution with respect to the dissolving phase. First, the rate of nucleation and growth of reaction products may be rate limiting. This is hypothesized to be the cause of the induction period in Portland cement hydration which occurs in the hours after the introduction of water. Initially rapid dissolution of the cement slows down as the solution reaches saturation with respect to the dissolving cement phases due to the slow rate of nucleation and growth of C-S-H. Second, mass transport of dissolving ions may limit the consumption of dissolved ions. Mass transport is may be the rate limiting mechanism at later ages of cement hydration (days to years), although this is not well quantified [54]. In this hypothesis, the formation of reaction products in the first hours and days of cement hydration covers precursor materials in a reaction product through which dissolving ions must then diffuse in order to produce further reaction product.

Hydration models are kinetic models that attempt to describe the extent of consumption of the primary Portland cement phases (60% C_3S, 15% β-C_2S, 8% C_3A, 8% C_4AF) as a function of time. Calorimetry curves describe the rate of heat evo-

lution during cement hydration, and hydration models are typically designed to fit experimentally measured heat profiles. These models often attempt to describe the hydration process through the use of physical models that describe the kinetics of nucleation and growth (e.g. the Avrami equation), and mass transport (e.g. the shrinking core model [122]). Fitting calorimetry curves in this manner is heavily reliant on tuning parameters that result in a good fit for the experimental data. Hydration models generally focus on timescales from hours to months during which it is assumed that dissolution is never the rate-limiting reaction, and either mass transport or nucleation and growth is. This assumption is valid over these timescales for highly reactive cement phases. However, the introduction of slower reacting phases could conceivably lead to dissolution acting as a rate limiting step.

In addition to kinetic considerations, the availability of aqueous ions must produce an assemblage of reaction products that are not too expansive (leading to mechanical instability), thermodynamically stable (or metastable), and durable. For this to occur, there must be a balance amongst the available aqueous ions. While finding this balance may at times be a limitation in designing concretes with a suitable balance of available aqueous ions, it can also represent an opportunity for synergy by combining precursors which are rich in different elements. One example of this is the pozzolanic reaction involving alumino-silicates and Portland cement. The high concentration of Ca in solution at early ages of Portland cement hydration results in an excess of Ca relative to Si, and portlandite ($Ca(OH)_2$) precipitates as a result. The presence of an Al and Si species in solution due to the dissolution of the alumino-silicate precursor results in the reaction of surplus Ca with Al and Si species to produce C-A-S-H, an aluminum substituted calcium silicate hydrate (written in cement notation);

$$AS_2 + 3CH + 6H \rightarrow C - A - S - H + C_2ASH_8 \tag{5.1}$$

Related to this example is the synergy between precursors seen in limestone-calcined clay-cement (LC3) systems [123]. LC3 systems are a promising alternative to purely Portland cement based systems due to their lower environmental impact. In LC3 sys-

tems, not only is the pozzolanic reaction present through the reaction of the aluminosilicate calcined clay and the portlandite, there are further reactions between alumina from C_3A and limestone to produce hemicarboaluminate (written in cement notation, where c = CO_3);

$$C_3A + 0.5Cc + 0.5CH + 11.5H \rightarrow C_4Ac_{0.5}H_{12} \tag{5.2}$$

and between the aluminates from the calcined clay and the limestone, leading to further formation of hemicarboaluminate;

$$AS_2 + 0.5Cc + 3.5CH + 8.5H \rightarrow C_4Ac_{0.5}H_{12} \tag{5.3}$$

The formation of these additional phases results in dense microstructure and extensive pore-filling, resulting in an LC3 binder with good mechanical properties and resistance to corrosion. For precursors with a high quantity of available alumina, the pozzolanic reaction may not consume all of the available alumina. In this case, introduction of additional sulfate into the system can promote the reaction of alumina with sulfate. This reaction serves as the basis for calcium sulfo-aluminate cements, in which precursor phases such as ye'elemite ($C_4A_3\bar{S}$), C_4AF, and C_2S react to form monosulfate ($C_3A.CS.12H$), ettringite ($C_3A.3C\bar{S}.32H$), and strätlingite (C_2ASH_8). Empirical determinations of the amount of reactive sulfate that results in the optimum mortar strength have been developed [21].

The literature has demonstrated effective use of industrial wastes in building materials by following the principle of identifying synergistic reactions between precursors. The pozzolanic reaction involving ground granulated blast furnace slag or fly ash has been the focus of much attention, as has the geopolymeric reaction of these precursors in the presence of an alkali-activator [124]. A synergy has also been identified for ladle slags with high calcium and alumina content mixed with gypsum, or any other calcium sulfate rich material [125, 126]. In fact, most EAF and LF slags contain high Ca and Al contents, making them attractive precursors for calcium sulfo-aluminate systems. This is illustrated in the model slags shown in Tables 5.6 and 5.8. In 5.6,

Slag B has a high gehlenite ($Ca_2Al(AlSiO_7)$) content and Slag C has a high mayenite content ($Ca_{12}A_{14}O_{33}$). In table 5.8, Slag A has high gehlenite content and Slags B and C high mayenite content. These particular model slags represent a high content of available Ca and Al, suitable for reaction with sulfate containing precursors. Slags with high contents of Ca and Si bearing phases are most appropriate for use in C-S-H or C-A-S-H binders, i.e. Portland cement or blended Portland cement based binders. In tables 5.6 and 5.4, all six model slags have significant β-C_2S content. The high dissolution rate of β-C_2S makes these slags promising candidates to for inclusion in Portland cement or blended Portland cement based binders, where Ca and Si are involved in the formation of C-S-H and/or C-A-S-H. Efforts at using high Fe-content slags have also met with some success. The formation of F-S-H type binders has been reported through alkali-activation of fayalitic slags [127, 52, 128, 129]. This represents a promising avenue of research for steel and copper slags given the ubiquity of high Fe content in these slags.

The purpose of this chapter is to contribute towards the development of a framework that accounts for the reaction kinetics of both Portland cement and crystalline slags (steel or copper slag). There are 3 main research questions that are answered in this chapter;

- What is the phase composition and microstructure of copper, BOF, EAF, and LF slags?
- To what extent can the dissolution rates of these phases be estimated from existing literature?
- How can cement hydration kinetics and dissolution rates be used to model the reaction product assemblage of mixed Portland cement-slag binders?

The first research question seeks to address a gap related to the lack of steel and copper slag phase composition compilations. Answering this research question allows the second research question to be answered. Once the most prevalent phases in these slags have been identified, we develop a database for the dissolution rates of these

phases. Finally, the dissolution rates of the slag phases are used to develop a kinetic model for slag dissolution, which in turn is used to determine the evolution of the reaction product assemblage of the Portland cement-slag binder.

5.2 Copper and steel slag composition

5.2.1 Phase composition

For each slag type (copper, basic oxygen furnace, electric arc furnace, and ladle furnace), a comprehensive review of reported slag phases is compiled. Based on this data, 3 model slags for each slag type are proposed. The purpose of these model slags is to summarize the large number of reported slag compositions in a way that illustrates the range of phase compositions within a given slag type. The model slags are also used as a basis for modeling slag dissolution and reaction product formation in Section 5.4.1.

Copper slag

Background on the production of copper slag is given in Section 1.2.2. In short, the production of copper slag involves two processes which produce slag as a byproduct; matte smelting and converting. Slags from both processes are typically rich in FeO, SiO_2, and Fe_2O_3,and have minor quantities of Al_2O_3, CaO, and MgO [38]. The dominant reaction during the smelting phase is the formation of fayalite (Fe_2SiO_4). An extensive literature review of reported copper slag phase composition was performed in order to identify the most commonly reported phases. The results of this literature review are summarized in Table 5.1, and the full literature review is included in the Appendix. The predominance of fayalite, an amorphous phase, and an iron rich spinel (reported as magnetite) is apparent.

In the context of the above background and literature review, it is possible to propose 3 model slags whose compositions reflect the variation in of typical slag compositions. This is shown in Table 5.2, whereby each of the 3 model slags is

Phase	Chemical formula	Times reported/ Number of slags
Fayalite	Fe_2SiO_4	23/28
Spinel/magnetite	Fe_3O_4	22/28
Glass	N/A	21/28
Pyroxene	$(Ca,Fe,Mg)(Ca,Fe,Mg)Si_2O_6$	8/28
Quartz	SiO_2	6/28
Melilite	$(Ca,Na)_2(Al,Mg,Fe^{2+})(Al,Si)SiO_7$	2/28
Leucite	$KAlSi_2O_6$	2/28
Pyrite/Sphalerite	FeS/(Fe,Zn)S	5/28
Copper/iron sulfides	N/A	8/28
Copper metal	Cu	7/28

Table 5.1: Summary of reported phase composition of copper slags.

similar to the typical phase composition from a given copper-making process The difference between Slag A and Slag B is the abundance of olivine over glass – this is a consequence of the cooling rate of the slag.

	Olivine (wt%)	Glass (wt%)	Spinel (wt%)	Pyroxene (wt%)	Process
Slag A	60	20	10	10	Matte smelting/Peirce-Smith converting, slow cooled
Slag B	20	60	10	10	Matte smelting/Peirce-Smith converting, quenched
Slag C	30	30	30	10	Flash converting

Table 5.2: Phase composition of model copper slags.

Basic oxygen furnace (BOF) slag

Basic oxygen furnaces (BOF), also known as Linz-Donawitz (LD) furnaces, and variations on BOF furnaces account for 72% of global crude steel production [27]. The oxides CaO, MgO, FeO, and SiO_2 typically account for 90% of BOF slag chemical composition. β-C_2S, dicalcium ferrite, RO phase, and lime are most commonly reported in BOF slag. The presence of these phases is consistent both over the decades and across countries, as illustrated in Table 5.3. The full literature review is included in the Appendix. Three theoretical slags were designed to illustrate the variation in the phase composition of BOF slags, shown in Table 5.4. BOF A has high RO phase content, moderate quantities of β-C_2S and dicalcium ferrite, and minor quantities of

Phase	**Chemical formula**	**Times reported/ Number of slags**
β-C_2S	Ca_2SiO_4	39/42
Dicalcium ferrite	$Ca_2Fe_2O_5$	35/42
RO phase/Wüstite	(Fe,Mg,Mn)O	35/42
Lime	CaO	28/42
Periclase	MgO	12/42
Magnetite	Fe_3O_4	17/42
Hematite	Fe_2O_3	5/42
Calcio-olivine	Ca_2SiO_4	5/42
Fayalite	Fe_2SiO_4	5/42
Wollastonite	$Ca_2Si_2O_6$	7/42
Ferrosilite	$Fe_2Si_2O_6$	4/42
Enstatite	$Mg_2Si_2O_6$	4/42
C_3S	Ca_3SiO_5	16/42
Gehlenite	$Ca_2Al(AlSiO_7)$	2/42
Glass	N/A	5/42
Quartz	SiO_2	4/42
C_4AF	$Ca_4Al_2Fe_2O_{10}$	2/42
Mayenite	$Ca_{12}Al_{14}O_{33}$	2/42
Corundum	Al_2O_3	2/42
Portlandite	$Ca(OH)_2$	18/42
Brucite	$Mg(OH)_2$	5/42
Calcite	$CaCO_3$	16/42

Table 5.3: Summary of reported phase composition of BOF slags.

magnetite, lime, and C_3S similar to slags reported by [130] and [131]. BOF B has high β-C_2S content, moderate quantities of dicalcium ferrite and RO phase, and minor quantities of lime, C_3S, and magnetite, similar to slags reported by [131]. BOF C has high dicalcium ferrite and lime, moderate quantities of β-C_2S and γ-C_2S, and minor quantities of RO phase, C_3S, and magnetite, similar to slags reported by [132] and [133].

	β-C_2S (wt%)	**Dicalcium ferrite (wt%)**	**RO phase (wt%)**	**Lime (wt%)**	**C_3S (wt%)**	**Magnetite (wt%)**	**γ-C_2S** (wt%)
Slag A	30	15	30	5	5	10	0
Slag B	50	15	20	5	5	5	0
Slag C	20	35	5	15	5	5	15

Table 5.4: Phase composition of model BOF slags.

Electric Arc Furnace (EAF) Slag

Electric arc furnace (EAF) slag accounts for 28% of global crude steel production [27]. The EAF typically takes steel scrap as an input. The higher variability in the composition of the inputs to the EAF corresponds to slags with higher compositional variability compared to BOF slags. This is illustrated in Table 5.5 and the full literature review is included in the Appendix. P associates with calcium silicate phases, stabilizing the β phase of Ca_2SiO_4, and Mn and Al substitutes with Fe in dicalcium ferrite.

Phase	**Chemical formula**	**Times reported/ Number of slags**
β-C_2S	Ca_2SiO_4	15/24
RO phase/Wüstite	(Fe,Mg,Mn)O	16/24
Spinel	$(Fe,Mg,Mn,Ca)(Fe,Al,Cr)_2O_4$	9/24
Calcio-olivine	Ca_2SiO_4	3/24
Kirschsteinite	$CaFeSiO_4$	3/24
Gehlenite	$Ca_2Al(AlSiO_7)$	9/24
Merwinite	$Ca_3MgSi_2O_4$	6/24
Bredigite	$Ca_7MgSi_4O_{16}$	4/24
Akermanite	$Ca_2MgSi_2O_7$	2/24
Cuspidine	$Ca_4Si_2O_7(F,OH)_2$	2/24
Quartz	SiO_2	3/24
Brownmillerite	$Ca_2(Fe,Al)O_5$	6/24
Hematite	Fe_2O_3	4/24
Mn oxides	N/A	3/24
Mayenite	$Ca_{12}Al_{14}O_{33}$	4/24
Periclase	MgO	3/24

Table 5.5: Summary of reported phase composition of EAF slags.

Three theoretical slags were designed to illustrate the variation in the phase composition of EAF slags, shown in Table 5.6. EAF A has high RO phase and β-C_2S content and minor quantities of magnetite, olivine, and brownmillerite, similar to slags reported by [134] and [135]. EAF B has high gehlenite ($Ca_2Al(AlSiO_7)$) content, moderate quantities of β-C_2S and RO phase, and minor quantities of magnetite and brownmillerite, similar to slag reported by [136]. EAF C has moderate quantities of β-C_2S, RO phase, and mayenite, and minor quantities of magnetite and olivine, similar to slags reported by [137], [138], and [139].

	β-C_2S (wt%)	RO phase (wt%)	Magnetite (wt%)	Olivine (wt%)	Brownmillerite (wt%)	Gehlenite (wt%)	Mayenite (wt%)
Slag A	35	50	5	5	5	0	0
Slag B	20	20	5	0	5	50	0
Slag C	25	45	5	5	0	0	20

Table 5.6: Phase composition of model EAF slags.

Ladle Furnace (LF) slag

Ladle furnaces (LF) are used to produce steel alloys and take steel from BOFs or EAFs as input. Due to the wide variation in the composition of steel alloys, slags from LFs are highly variable in their composition. Reported phases in LF slags are compiled in Table 5.7 with the full literature review included in the Appendix.

Phase	Chemical formula	Times reported/ Number of slags
β-C_2S	Ca_2SiO_4	11/18
Calcio-olivine	Ca_2SiO_4	14/18
Periclase	MgO	13/18
Mayenite	$Ca_{12}Al_{14}O_{33}$	12/18
C_3A	$Ca_3Al_2O_6$	7/18
Wollastonite	$Ca_2Si_2O_6$	3/18
Diopside	$CaMgSi_2O_6$	4/18
Glass	N/A	5/18
Gehlenite	$Ca_2Al(AlSiO_7)$	4/18
Bredigite	$Ca_7MgSi_4O_{16}$	4/18
Merwinite	$Ca_3MgSi_2O_4$	4/18
C_3S	Ca_3SiO_5	3/18
Quartz	SiO_2	2/18
Jasmundite	$Ca_{11}(SiO_4)_4O_2S$	3/18
Fluorite	CaF_2	7/18
Spinel	$(Fe,Mg,Mn,Ca)(Fe,Al,Cr)_2O_4$	3/18
Wüstite	FeO	3/18
Portlandite	$Ca(OH)_2$	6/18
Dolomite	$(Ca,Mg)CO_3$	3/18

Table 5.7: Summary of reported phase composition of LF slags.

Three theoretical slags were designed to illustrate the variation in the phase composition of LS slags, shown in Table 5.8. LF A has high γ-C_2S content and minor quantities of β-C_2S, periclase, gehlenite ($Ca_2Al(AlSiO_7)$, fluorite, and merwinite, sim-

ilar to slag reported by [140]. LF B has high quartz content, moderate quantities of γ-C_2S and mayenite, and minor quantities of periclase, similar to slag reported by [126]. LF C has high quantities of pyroxene, moderate quantities of γ-C_2S and mayenite, and minor quantities of β-C_2S and periclase, similar to slags reported by [28, 141].

	β-C_2S (wt%)	**γ-C_2S (wt%)**	**Periclase (wt%)**	**Mayenite (wt%)**	**Gehlenite (wt%)**	**Fluorite (wt%)**	**Merwinite (wt%)**	**Pyroxene (wt%)**	**Quartz (wt%)**
Slag A	10	60	10	0	10	5	5	0	0
Slag B	0	20	5	20	0	0	0	0	50
Slag C	5	20	5	20	0	0	0	40	0

Table 5.8: Phase composition of model LF slags.

5.2.2 Slag microstructure

In real heterogenous slags, the distribution of phases may result in certain reactive phases being completely surrounded by less reactive phases. A mineral that is inaccessible in this way is "locked". Given that slag phases solidify in a sequence as successive melting temperatures are reached during cooling, the probability of certain phases being "locked" should be accounted for. Certain phases could be considered to have a lower effective concentration in the slag due to this phenomenon. A process for calculating "mineral locking" has been developed elsewhere and is not used here [142]. Rather, microstructures of the relevant slag types are reviewed here in order to identify which phases are more typically found as inclusions in a slag matrix and may be more prone to mineral locking.

Copper slags

The microstructure of copper slag is dominated by 2 phases; Fe-rich olivine and Fe-rich spinel. Depending on the thermal history, phases such as glass, pyroxenes, melilite, and leucite may form. Vitkova et al. identify 6 solidification pathways depending on the composition of the slag: in all cases a spinel phase is the first phase to form at high temperature and a glassy matrix is the last phase to form with olivine, pyroxene, leucite, and plagioclase identified as phases that may form at intermediate

temperatures [143]. Spinel phases are the first phases to solidify (commonly identified as the iron rich spinel end-member, magnetite), with grains that are typically spherical or rectangular in shape [143, 144, 145, 146, 147], although dendritic morphologies have been observed in rapidly cooled slags [143, 145, 148]. Grain sizes are in the range 10 - 100 µm. Wüstite may also form during initial solidification [145]. Grains of olivine are formed following initial solidification. Olivine grains are typically described as either lath-like [143, 144, 145], skeletal [146, 149], or spherical [150, 151], large melilite (akermanite) grains [145], and spherical leucite grains [150]. A glassy matrix forms last, locking other phases in place, as well as unreacted precursors such as metal sulfides or metals.

BOF slags

The microstructure of BOF slag appears to be quite predictable due to the relatively consistent thermal history and composition of all BOF slags. In fact, the mineralogy has been reported to be largely independent of the cooling rate, although grain size and shape is not [152, 153]. Cooling of slag initially forms phase composed of the basic oxides CaO, MgO, and FeO. These oxides form phases such as lime, periclase, or wüstite. The inclusion of Mn in a solid solution with Mg and Fe is common, resulting in RO phase, or magnesio-wüstite, while lime typically appears as a separate phase. Grains of residual lime are due to unreacted flux and are typically globular and range in size from several microns to tens of microns [133, 152, 154, 155, 156]. Grains of MgO from furnace refractory materials have also been reported [155, 157]. RO phase or magnesio-wüstite grains are also globular but more angular than grains of lime and range in size from 10 - 100 μm [132, 133, 137, 138, 152, 153, 155, 156, 158, 159, 160, 161, 162, 163]. β-Ca_2SiO_4 solidifies around 1300°C. The β phase of dicalcium silicate is stabilized by the presence of P is BOF slag and forms a solid solution with $Ca_3P_2O_8$ [161]. β-Ca_2SiO_4 grains are typically globular and range in size from 10 - 100 μm [132, 133, 138, 154, 156, 158, 160, 162]. Calcium ferrite begins to solidify at temperatures $<$ 1100°C and frequently forms as a matrix around calcium silicate and basic oxide phases, although calcium ferrite "laths" have been reported [132].

EAF slags

The microstructure and phases of EAF slag are more variable than either copper slag or BOF slag due to the greater variation in EAF feedstocks. Spinel phases and other basic oxide phases (wüstite, magnesio-wüstite) are the first phases to solidify. Wüstite (magnesio-wüstite, RO phase) grains are typically globular inclusions on the order of 10 - 100 μm [137, 139, 164, 165, 166, 167, 168] although dendritic wüstite is also observed [139, 167]. Spinel grains are either euhedral [157, 169] or globular inclusions [137, 168, 169, 170] and range in size from 10 - 100 μm, similar to wüstite grains. The spinel phase forms a solid solution which varies in composition predominantly from magnetite (Fe_3O_4) to jacobsite ($Fe(Fe,Mn)_2O_4$) to magnesio-ferrite ($MgFe_2O_4$) [169]. Cr associates with the spinel phase, and chromite ($FeCr_2O_4$) is also commonly observed. V may also be associated with the spinel phase [167]. The final phase to solidify forms the slag matrix, and various slag matrices have been observed: gehlenite and brownmillerite [166]; monticellite [170]; larnite [137]; gehlenite and kirschsteinite [168]; gehlenite and larnite [168]; olivine [167]; merwinite [171]; and akermanite [171]. There is a wide range in the type and morphology of phases that form at intermediate temperatures. There is no systematic manner in which these phases form due to variation in slag composition and cooling rates.

LF slags

The variability in LF slag composition translates to a corresponding variability in microstructure and microstructure characterization is sparse in the literature. Spinel-like MgO in a silica, calcia, alumina glass matrix was reported [157]. Adolfsson et al. also reported a spinel like RO phase containing Mg, Fe, and Mn contained within a calcium silicate matrix [30]. Brand et al. imaged a slag with a β-C_2S matrix containing wüstite and mayenite inclusions [137].

5.3 Dissolution modeling

5.3.1 Rates of individual phases

On the basis of the above literature review of copper and steel slags, the following crystalline phases have been identified as prevalent and deserving of further attention; β-C_2S (Ca_2SiO_4), RO phase ((Fe,Mg)O), γ-C_2S (Ca_2SiO_4), fayalite (Fe_2SiO_4), dicalcium ferrite/brownmillerite ($Ca_2Fe_2O_5$/Ca_2(Fe,Al)O_5), magnetite (Fe_3O_4), pyroxenes ((X)(Y)$(Si,Al)_2O_6$; X= Mg, Ca, Fe; Y = Mg, Ca, Fe), gehlenite/akermanite ($Ca_2Al(AlSiO_7)$/$Ca_2Mg(Si_2O_7)$), mayenite ($Ca_{12}Al_{14}O_{33}$), merwinite ($Ca_3Mg(SiO_4)_2$), and lime (CaO). These phases are frequently observed across all 4 slag types.

The logarithm of mineral dissolution rates are typically observed to change linearly as a function of pH, as described in Equation 5.4:

$$log(r) = log(k_0) - n \times pH \tag{5.4}$$

where r (mol^{-1} cm^{-2} s^{-1}) is the dissolution rate, k_0 (mol^{-1} cm^{-2} s^{-1}) is the dissolution rate at pH 0, a_{H^+} is the activity of H^+ ions in solution, and n is the pH term coefficient. The pH term coefficient is generally different in acidic (n_{acid}) and basic (n_{base}) solutions due to changes in the dissolution mechanism from acid to base, and two pH term coefficients are required:

$$0 < pH < 7 : log(r) = log(k_0) - n_{acid} \times pH \tag{5.5}$$

$$7 < pH < 14 : log(r) = log(k)_0 - n_{acid}pH - n_{base}pH \tag{5.6}$$

In the following sections, the dissolution rate of each mineral at pH 13 is either reported from a direct measurement of the dissolution rate at pH 13 or calculated by extrapolating the dissolution rate to pH 13 using pH term coefficients. The lack of dissolution rate data for phases in high pH systems necessitates a flexible approach based on available data. In general, dissolution rates are at far from equilibrium conditions in the absence of other aqueous ions.

RO phase

The RO (reducing oxide) phase of slags consists of a solid solution of Fe, Mg, and Mn. The Fe end-member is known as wüstite, the Mg endmember is known as periclase, and the Mn endmember is known as manganosite. Given the high Fe concentration of steel slags, the RO phase is typically close in composition to wüstite but may contain significant Mg and Mn content. Within this solid solution, phases commonly reported in slag include periclase, wüstite, magnesiowüstite, and ferropericlase. Inhomogeneities during slag solidification may result in multiple phases from this solid solution being reported in a single slag. The hydration of periclase (MgO) to form brucite ($Mg(OH)_2$) is an expansive reaction, similar to the hydration of lime (CaO) to form portlandite ($Ca(OH)_2$). These expansive reactions can result in poor volume stability of concrete due to deleterious expansive reactions. Wüstite does not hydrate quickly and its hydration is not a problematic reaction. Geiseler and Schlösser investigated the hydration characteristics of RO phase as a function of the MgO and FeO content. They reported no mechanical disintegration during hydration of the RO phase at 84°C and 0.53 bar as long as the MgO content of the RO phase is less than 70% [172]. Juckes also discusses the volume stability of MgO and suggests that RO phase crystals with MgO content $> 40\%$ may be capable of hydration [131]. The same trend was observed by Qian et al. in which higher contents of MgO resulted in faster hydration [173]. Juckes highlights potential spatial distributions of MgO and FeO in the RO phase - the higher temperature melting point of MgO may result in a RO phase which is richer in MgO at its core than near the surface due to initial solidification of MgO followed by surrounding FeO.

The dissolution rate of wüstite has been quantified by Jang and Brantley [174]. At 25°C and pH 5.8, wüstite has a dissolution rate of 1.6×10^{-13} mol cm^{-2} s^{-1} ($\log(r) = -12.8$) [174]. It dissolves more quickly under acidic conditions with an acid pH term coefficient of 0.64. This dependence implies slower dissolution rates at higher pH: extrapolation to pH 7 gives a dissolution rate of 2.7×10^{-14} mol cm^{-2} s^{-1} ($\log(r) = -13.6$). The effect of FeO content and pH on RO phase dissolution rate

were qualitatively assessed by Strandkvist et al. [175]. RO phase with > 60 wt% FeO was reported as not dissolving at all at pH 10. Extending the range of studied pH values to 10 is tentative confirmation that the dissolution rate of wüstite continues to decrease at least up to pH 10. Assuming that the base pH term coefficient is the same as the acid pH term coefficient, extrapolation of the pH 7 dissolution rate to pH 13 implies a dissolution rate of 3.9×10^{-18} mol cm^{-2} s^{-1} ($\log(r)= -17.4$).

The dissolution rate of MgO was measured by [176] up to pH 10. Based on the observed trend in basic solution, the base pH term coefficient is estimated to be -0.33. Extrapolating the dissolution rate to pH 13 gives a rate of 1×10^{-12} mol cm^{-2} s^{-1} ($\log(r)= -17.4$), 6 orders of magnitude faster than FeO dissolution.

Magnetite

Magnetite contains iron in both Fe(II) and Fe(III) oxidation states. The mechanism of magnetite dissolution depends on whether aqueous conditions are oxic or anoxic. Dissolution of magnetite proceeds most quickly via a reductive pathway which under anoxic acidic conditions produces maghemite, γ-Fe_2O_3;

$$FeO.Fe_2O_3(magnetite) + 2H^+ \rightarrow \gamma - Fe_2O_3(maghemite) + Fe^{2+} + H_2O \quad (5.7)$$

The dissolution rate of Fe^{2+} from magnetite was investigated by White et al. on 3 different magnetite samples of geological origin in pH 1 - 7 [177]. At pH 7, the average reported dissolution rate for the 3 samples is 3.6×10^{-15} mol cm^{-2} s^{-1} ($\log(r)= -14.5$) with an average pH term coefficient of 0.24. As the dissolution of magnetite proceeds, the surface layer gradually becomes enriched in Fe^{3+} in the form of maghemite, which is less susceptible to solvation. Despite being linear for up to first thirty-six hours, the reaction rate slows and is expected to become diffusion limited due to the formation of a maghemite product layer. Assuming that the dissolution decreases with increasing pH in basic solution at the same rate as in acidic solution, extrapolation of the pH 7 dissolution rate to pH 13 implies a dissolution rate of 1.1×10^{-16} mol cm^{-2} s^{-1} ($\log(r)= -15.9$). Dissolution rates of magnetite as a function of Fe(II) and oxalate

concentration were investigated by [178]. At low concentrations of Fe(II) or oxalate ions, the initial dissolution rate of magnetite was $\sim 1\times10^{-11}$ mol cm^{-2} s^{-1}. The 4 orders of magnitude difference in dissolution rate between these two studies illustrates the large uncertainties in reported dissolution rate experiments.

Brownmillerite

Brownmillerite is a solid solution series of the form $Ca_2Al_xFe_{2-x}O_5$, where x ranges from 0 to 1.4. Brownmillerite and the iron endmember, $Ca_2Fe_2O_5$ (calcium ferrite, or srebodolskite), are commonly found in EAF slag and as a primary component of the ferrite phase in Portland cement although the Portland cement ferrite phase (C_4AF) is an impure form of brownmillerite. Empirical fits of the hydration rate of the ferrite phase are already described for real cementitious systems [179, 7]. Meller et al. measured the hydration rate of Ca_2AlFeO_5 in isolation at 30°C using measured using energy dispersive diffraction (EDD) [180]. A rate constant of 0.015 h^{-1}, equivalent to a reaction rate of 7.8×10^{-12} mol cm^{-2} s^{-1} ($\log(r)= -11.1$), was calculated in the absence of gypsum at a liquid to solid ratio of 0.5. The rate is dependent on the brownmillerite's stoichiometry: a higher Al/Fe ratio appears to increase the hydration rate - the difference in hydration rate between $Ca_2Fe_2O_5$ and Ca_2FeAlO_5 is about 1 order of magnitude [181, 182, 183, 180]. In addition, the rate is increased by the presence of sulfate, which at room temperature causes ettringite ($Ca_6Al_2(SO_4)_3(OH)_{12}\cdot26H_2O$) to form instead of the metastable hydrate [180]. Finally, the rate of dissolution at pH 10 is slower than at pH 7.

γ-Ca_2SiO_4

Calcio-olivine (γ-Ca_2SiO_4) is the calcium end-member of the olivine solid solution series. The dissolution rate of calcio-olivine is comparatively understudied compared to that of the Mg end-member, forsterite. However, extensive dissolution studies of forsterite have revealed a pH term coefficient for olivine minerals of 0.5 in acidic solutions and 0.25 in basic solutions. Westrich et al. determined the dissolution rate of calcio-olivine in acidic solution [6]. Extrapolation of their data to pH 7 implies a pH 7

dissolution rate of 1.5×10^{-11} mol cm^{-2} s^{-1} ($\log(r)= -10.8$). Traynor et al. measured the dissolution rate and pH dependence of calcio-olivine in basic solution [62]. The dissolution rate at pH 13 was recorded as 3.2×10^{-13} mol cm^{-2} s^{-1} ($\log(r)= -12.5$). Extrapolation of their data to pH 7 predicts a pH 7 dissolution rate of 1×10-11 mol cm^{-2} s^{-1} ($\log(r)= -11$), in good agreement with Westrich et al. The pH term coefficient was calculated to be 0.24 over the pH range of interest, 11-13.5.

Fayalite

Fayalite (Fe_2SiO_4) is the iron end-member of the olivine solid solution series. Traynor et al. measured the dissolution rate and pH dependence of both synthetic fayalite and a fayalitic slag in basic solution [62]. The dissolution rate at pH 13 was recorded as 7.9×10^{-14} mol cm^{-2} s^{-1} ($\log(r)= -13.1$). Extrapolation of dissolution rate data for the synthetic fayalite to pH 7 predicts a pH 7 dissolution rate of 1.3×10^{-15} mol cm^{-2} s^{-1} ($\log(r)= -14.9$) and a pH term coefficient of 0.3 over the pH range of interest, 10-13. Dissolution rate measurements for the fayalitic slag are very similar in terms of both the measured dissolution rates and the pH term coefficient.

Pyroxenes

The pyroxene mineral group forms a solid solution of the form (Mg,Fe^{2+},Ca) (Mg,Fe^{2+}) $(Si,Al)_2O_6$. In crystalline slags the presence of a pyroxene phase is identified by the presence of one of the end-members of the solid-solution: diopside ($CaMgSi_2O_6$), wollastonite ($Ca_2Si_2O_6$), enstatite ($Mg_2Si_2O_6$), hedenbergite ($FeCaSi_2O_6$), augite ((Ca,Na) (Mg,Fe,Al,Ti) $(Si,Al)_2O_6$), esseneite ($CaFeAlSiO_6$), and ferrosilite ($Fe_2Si_2O_6$) have all been identified in BOF, LF, or copper slags. The dissolution rate of diopside, wollastonite, enstatite, augite, and hedenbergite have all been studied over a range of pH values, shown in Figure 5-1. Dissolution rate experiments have been preformed predominantly on diopside and wollastonite at near neutral pH. Given the predominance of dissolution rate experiments in near neutral pH conditions and the large discrepancies in reported rates across publications, the dissolution rate at pH 13 is estimated by extrapolating all dissolution rates to pH 13 using the acidic and basic solution pH

term coefficients. This provides a more robust estimate for the dissolution rate by considering more data points. The effect of mineral composition on dissolution rate is also of interest, although this is poorly quantified and difficult to predict in basic solution using existing dissolution rate data.

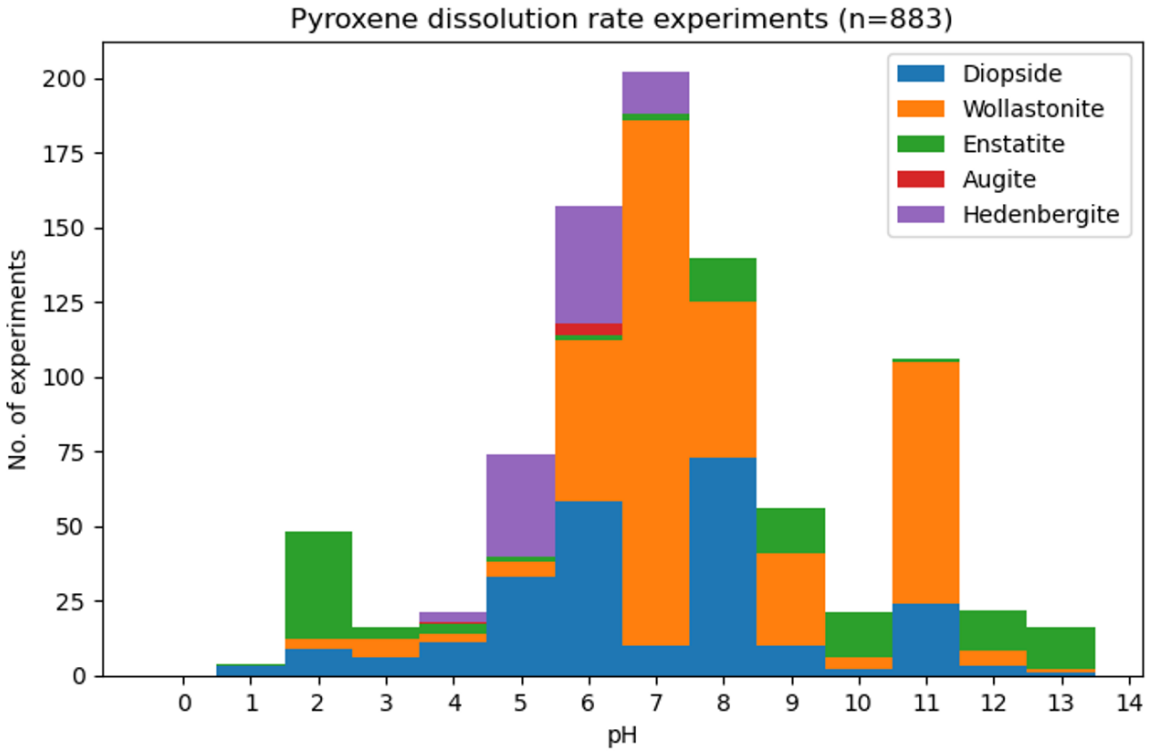

Figure 5-1: Histogram of number of experimental measurements of selected pyroxenes as a function of pH.

Fits of dissolution rate as a function of pH for diopside dissolution are shown in Figure 5-2 [119, 101, 121]. The pH term coefficient is calculated for each publication. For diopside, the pH term coefficient in acidic and basic solution are calculated to be -0.18 and -0.02 respectively. There are 56 diopside dissolution rate experiments which are measured at far from equilibrium conditions in the absence of other aqueous ions (such as organic ligands) and these dissolution rates are extrapolated to pH 7 using the pH term coefficients above [119, 101, 121, 184, 120, 185, 186]. The mean dissolution rate at pH 7 is $5(\pm 6)\times 10^{-16}$ mol cm^{-2} s^{-1} ($\log(r) = -15.3\pm 0.5$), where the uncertainty is the standard deviation of the 56 dissolution rate experiments. The pH 13 dissolution rate is $4(\pm 4)\times 10^{-16}$ mol cm^{-2} s^{-1} ($\log(r) = -15.4\pm 0.5$).

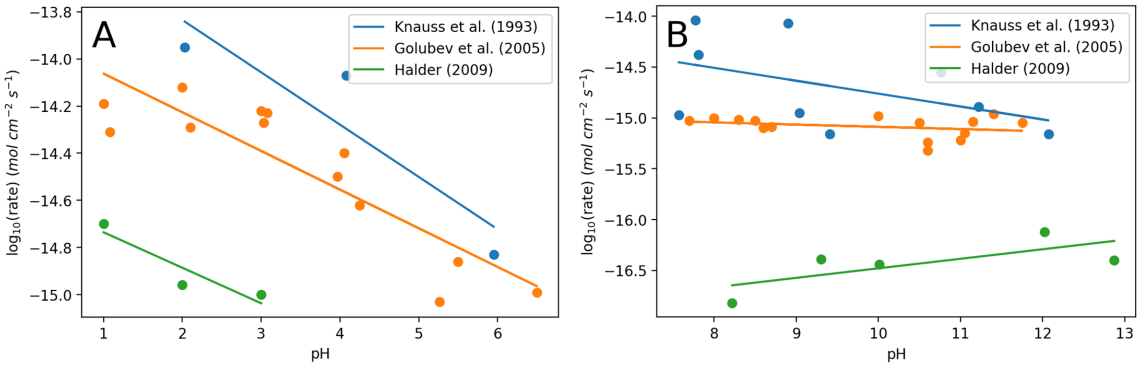

Figure 5-2: Linear of fits of log dissolution rate as a function of pH in: A - acidic solution and B - basic solution

In the case of enstatite, the dissolution rate is measured as a function of pH in 2 separate studies. The dissolution rate of enstatite is measured as a function of pH in both acidic and basic solution at 70°C by Oelkers and Schott [187] and in basic solution by Halder and Walther [188]. The pH term coefficient in acidic solution as determined by regression of the data from [187] is -0.23. The pH term coefficient in basic solution as determined by regression of the data from [188] is -0.02. There are 55 enstatite dissolution rate experiments which are measured at far from equilibrium conditions in the absence of other aqueous ions (such as organic ligands) and these dissolution rates are extrapolated to pH 7 using the pH term coefficients above. The mean dissolution rate at pH 7 is $2(\pm1)\times10^{-14}$ mol cm^{-2} s^{-1} ($\log(r)= -13.6\pm0.3$), where the uncertainty is the standard deviation of the 55 dissolution rate experiments. The small pH term coefficient in basic solution results in the same dissolution rate at pH 13; $2(\pm1)\times10^{-14}$ mol cm^{-2} s^{-1} ($\log(r)= -13.6\pm0.3$).

There are 2 studies that measure the dependence of wollastonite dissolution rate on pH in acidic solution [101, 189] and 3 studies that measure this dependence in basic solution [101, 121, 190]. The average pH term coefficient in acidic solution as determined by regression of the is -0.10. The pH term coefficient in basic solution as determined by regression is -0.22. The mean dissolution rate at pH 7 is $1(\pm1)\times10^{-13}$ mol cm^{-2} s^{-1} ($\log(r)= -12.9\pm0.3$), where the uncertainty is the standard deviation of the 46 dissolution rate experiments. The pH 13 dissolution rate is $6(\pm5)\times10^{-15}$ mol cm^{-2} s^{-1} ($\log(r)= -14.2\pm0.3$). The dissolution rate of hedenbergite is quantified at

Mineral	**Acidic pH term coefficient, n_{acid}**	**Basic pH term coefficient, n_{base}**	**pH 7 dissolution rate (mol cm^{-2} s^{-1})**	**pH 13 dissolution rate (mol cm^{-2} s^{-1})**
Diopside	-0.18	-0.02	$5(\pm6)\times10^{-16}$	$4(\pm4)\times10^{-16}$
Enstatite	-0.23	-0.02	$2(\pm1)\times10^{-14}$	$2(\pm1)\times10^{-14}$
Wollastonite	-0.1	-0.22	$1(\pm1)\times10^{-13}$	$6(\pm5)\times10^{-15}$
Hedenbergite			$6(\pm4)\times10^{-12}$ [a]	$6(\pm4)\times10^{-12}$ [b]

Table 5.9: Dissolution rates and pH term coefficients of selected pyroxenes. Errors are 1 standard deviation. [a]Dissolution rate measured at 23 MPa. [b]Assumes basic pH term coefficient for hedenbergite is 0.

high pressure and high temperature by Zhang et al. [191]. There is not enough data for hedenbergite dissolution rates to determine the pH term coefficient in acidic or basic solution. However, the dissolution rate is measured 36 times at different reactor flow rates in a flow reactor at high pressure – the pressure inside the reactor was 23 MPa for all experiments. The experiments were conduced at a temperature of 25°C and at near neutral pH. This allows the pH 7 dissolution rate to be approximated as $6(\pm4)\times10^{-12}$ mol cm^{-2} s^{-1} ($\log(r)= -11.2\pm0.3$). The pH 13 dissolution rate is $6(\pm4)\times10^{-12}$ mol cm^{-2} s^{-1} ($\log(r)= -11.2\pm0.3$).

Understanding how pyroxene composition affects the dissolution rate at a given pH is not straightforward. Correlations between composition and dissolution rate have been identified for some mineral groups at specific pH values [192, 193, 194]. There are challenges with attempting to transfer these tentative correlations to other mineral groups and different pH ranges: silicate connectivity, solubility of the component ions of the mineral, and the dissolution reaction mechanism at the surface may all be sufficiently different as to render previously identified correlations of little value.

Mayenite

Mayenite ($Ca_{12}Al_{14}O_{33}$, $C_{12}A_7$) hydrates rapidly with dissolution occurring over the first few minutes of hydration [195] and its hydraulic activity is similar to that of C_3A [196], both of which are more reactive than C_3S [197]. The rapid reaction of mayenite is known as "flash-setting" and in the absence of sulfur forms primarily C_2AH_8, in the presence of sulfur forms ettringite and/or monosulfoaluminate, and in

the presence of Cl^- ions forms Friedel's salt [30, 198, 199]. The high concentration of Al ions in solution due to rapid mayenite dissolution creates a sulfate imbalance. Additionally, cement hydration may be retarded due to the adsorption of Al ions onto calcium silicate surfaces [200]. Due to the extremely fast dissolution of mayenite, its dissolution kinetics have not been studied, but they can safely assumed to be at least at fast as the other Portland cement phases, i.e. on the order of 1×10^{-9} mol cm^{-2} s^{-1}.

Merwinite

The kinetics of merwinite dissolution have not been studied. The hydration of merwinite has been described as low, although hydraulic activity can be increased through mechanical and chemical activation (high pH) [72].

Merwinite is a nesosilicate, and its structure consists of isolated silicate tetrahedra - the same connectivity as olivine minerals. Dissolution of nesosilicates does not require the breaking down of a polymerized silicate chain. Therefore, the dissolution rate of nesosilicates is a function of the properties of its component cations. For Ca-Mg olivines, there is a correlation between the Ca/Mg molar ratio and the average bond strength of the metal-oxygen bonds in the mineral (Figure 5-3A). Here, the average bond strength of a given oxide, S_{M-O}, is calculated using classical bond valence models, as defined in Equation 5.8:

$$S_{M-O} = \frac{\sum n_M s_M CN_M}{\sum n_M} \tag{5.8}$$

where n_M, s_M, and CN_M are molar quantity, average bond valence, and average oxygen coordination number of each type of metal cation M (M = Si, Al, Fe, Mg, Ca, and Mn), respectively. The bond valence s_M is a measure of bond strength and commonly described as a function of bond length using Equation 5.9:

$$s_M = s_{0_M} \left(\frac{R_{M-O}}{R_{0_{M-O}}} \right)^{-N_M} \tag{5.9}$$

Metal-oxygen pair	s_{0_M}	$R_{0_{M-O}}$	N_M
Si-O	1	1.605	4
Al-O	0.5	1.888	4.6
Fe(III)-O	0.5	1.981	5.2
Fe(II)-O	0.333	2.128	4.9
Mg-O	0.333	2.076	5.2
Ca-O	0.25	2.437	5.5
Mn-O	0.333	2.165	5.1
Zn-O	0.5	1.946	5.7

Table 5.10: Empirical parameters for calculating bond metal-oxygen strengths from [5].

where R_{M-O} is the $M-O$ bond length, and s_{0_M}, $R_{0_{M-O}}$, and N_M are empirical parameters for each pair of atoms $M-O$, which have been determined by refining the model against accurate crystal structures as has been tabulated in [5], and are shown in Table 5.10. The average bond strength and the dissolution rate have a log-linear relationship for olivine minerals (Figure 5-3B). Given the similarities in structure and composition, the dissolution rate of merwinite is here calculated from this fit. The dissolution rate at pH 2 for merwinite from this log-linear fit is 7.8×10^{-10} mol cm^{-2} s^{-1} ($\log(r)= -9.1$). Translating the pH 2 dissolution rate to pH 13 requires the pH term coefficient in both acidic and basic solutions to be known. This term has not been determined, and here we assume that the dissolution rate pH dependence is the same as the olivines; 0.5 in acidic solutions and 0.25 in basic solutions. This yields a pH 13 dissolution rate of is 4.5×10^{-14} mol cm^{-2} s^{-1} ($\log(r)= -13.4$).

Gehlenite and akermanite

Neither gehlenite ($Ca_2Al(AlSiO_7)$) nor akermanite ($Ca_2Mg(Si_2O_7)$) dissolution kinetics have been measured. However, gehlenite and akermanite are sorosilicates, consisting of isolated pairs of Si or Si and Al tetrahedra surrounded by cations. The dissolution rates of other sorosilicates such as kyanite (Al_2SiO_5) have been reported [203]. At pH 13 the dissolution rate of kyanite is between 1×10^{-14} mol cm^{-2} s^{-1} and 1×10^{-13} mol cm^{-2} s^{-1}. Gehlenite and akermanite contain Ca and Mg cations that are not present in kyanite and the effect this would have on the dissolution rate is not

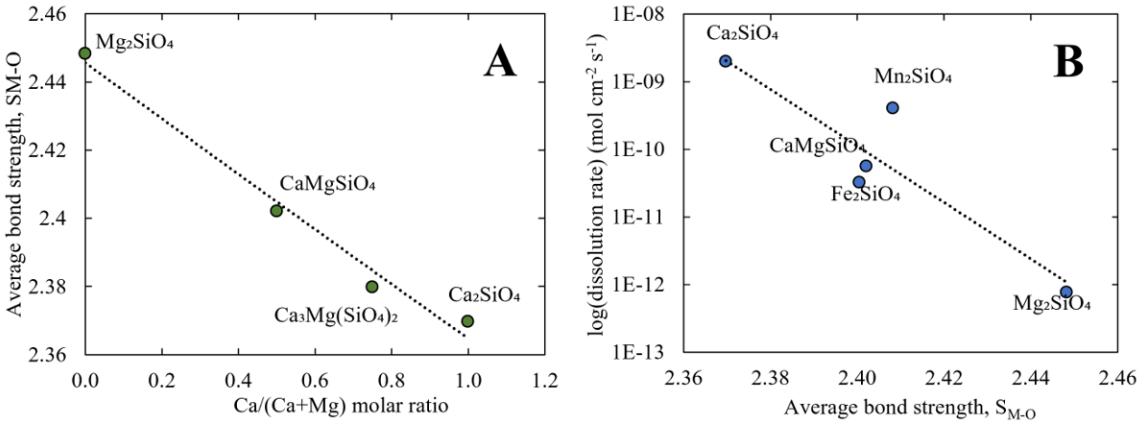

Figure 5-3: A: Average bond strength of selected orthosilicates as a function of Ca/Mg ratio. B: Dissolution rate of selected orthosilicates as a function of average bond strength.

known. Gehlenite and akermanite dissolution kinetics are assumed here to be of the same order of magnitude as kyanite. Studying dissolution kinetics of gehlenite and akermanite is an important future research task (see Section 7.2).

CaO

CaO dissolution is very fast which makes accurate measurements of its dissolution rate experimentally challenging. Despite this, the dissolution rate of CaO has been measured before in acidic solution: the dissolution rate is reported at pH 1 as 1.2×10^{-7} mol cm^{-2} s^{-1} ($\log(r)= -6.9$) and at pH 2 as 6.3×10^{-8} mol cm^{-2} s^{-1} ($\log(r)= -7.2$). This implies a pH term coefficient in acidic solutions of 0.3, but the dependence of dissolution rate on pH has not been explicitly measured. The dissolution rate of CaO was measured at pH 7 and pH 13 by [204] but experimental difficulties in measuring the surface area of the CaO used precludes a surface normalized dissolution rate from being determined. The dissolution rate of CaO was also measured in [205] using a rotating disc. The dissolution rate was found to be sensitive to the speed of rotation of the disc. At the slowest rotation, the dissolution rate of CaO in 0.1 M NaOH is given as 3.9×10^{-9} mol cm^{-2} s^{-1} ($\log(r)= -8.4$).

Mineral	**Metal, CN, Average BL (Å)**	**Metal, CN, Average BL (Å)**	**Metal, CN, Average BL (Å)**	S_{M-O} **(a.u.)**	**pH 2 rate (mol cm^{-2} s^{-1})^a**	**Reference**
Ca_2SiO_4	Ca(M1), 6, 2.351	Ca(M2), 6, 2.392	Si, 4, 1.646	2.3697	2×10^{-9}	[201]
Fe_2SiO_4	Fe(M1), 6, 2.175	Fe(M2), 6, 2.137	Si, 4, 1.666	2.4005	3.2×10^{-11}	Natl. Bur. Stand. (U. S.) Monogr. 25, 20, 59, (1984)
Mg_2SiO_4	Mg(M1), 6, 2.095	Mg(M2), 6, 2.13	Si, 4, 1.638	2.4482	7.6×10^{-13}	Natl. Bur. Stand. (U. S.) Monogr. 25, 20, 71, (1984)
$MgCaSiO_4$	Mg(M1), 6, 2.129	Ca(M2), 6, 2.368	Si, 4, 1.637	2.4021	5.6×10^{-11}	[202]
Mn_2SiO_4	Mn(M1), 6, 2.206	Mn(M2), 6, 2.227	Si, 4, 1.639	2.4083	4×10^{-10}	Natl. Bur. Stand. (U. S.) Monogr. 25, 21, 92, (1985)
$Ca_3Mg(SiO_4)_2$	Ca, 8, 2.561	Mg, 6, 2.065	Si, 4, 1.623	2.3798	7.8×10^{-10} ^{b}	Natl. Bur. Stand. (U. S.) Monogr. 25, 20, 34, (1984)

Table 5.11: Bond lengths, bond strengths, and dissolution rates of selected orthosilicate phases. CN = Coordination number of metal, BL = Bond length. ^{a}Dissolution rates from [6] ^{b}Calculated

Summary

Compilated dissolution rates are summarized in Table 5.12. Only β-C_2S, calcio-olivine, and fayalite have dissolution rates measured at the pH of interest. Periclase, wüstite, magnetite, the pyroxene minerals, and lime dissolution rates are extrapolated from dissolution rates at lower pH. The dissolution rate of merwinite is estimated from the dissolution rate of structurally similar minerals. The dissolution rate of dicalcium ferrite is estimated from a reported hydration rate and is expected to be higher under the more dilute, far-from equilibrium conditions of the other reported dissolution rates. The dissolution kinetics of mayenite, gehlenite, and akermanite have not been studied and are not known, although mayenite is known to hydrate rapidly upon contact with water. Therefore, mayenite is expected to have a very high dissolution rate, similar to that of lime.

There is a notable lack of dissolution rate studies on phases which are not geologically relevant – dissolution rate studies have long been the purview of geologists. Differences in composition between the earth's crust and metallurgical slags are illustrated in Table 5.13. Phases from steel and copper slags are generally enriched in FeO and CaO but lacking in SiO_2 and Al_2O_3 relative to geologically relevant minerals.

Mineral	**Formula**	**pH 13 rate (mol cm^{-2} s^{-1})**	**Method for dissolution rate**	**Ref**
β-C_2S	Ca_2SiO_4	1.7×10^{-9}	Directly reported	[204]
Wüstite	FeO	1.1×10^{-16}	Extrapolated from pH 5.8 rate	[174]
Periclase	MgO	1×10^{-12}	Extrapolated from pH 10 rate	[176]
Calcio-olivine	Ca_2SiO_4	3.2×10^{-13}	Directly reported	[62]
Fayalite	Fe_2SiO_4	7.9×10^{-14}	Directly reported	[62]
Dicalcium ferrite/ brownmillerite	$Ca_2Fe_2O_5$/ $Ca_2(Fe,Al)O_5$	7.8×10^{-12}	From hydration rate of 0.015 h^{-1}	[180]
Magnetite	Fe_3O_4/ $FeCr_2O_4$	3.9×10^{-18}	Extrapolated from pH 7 rate	[177]
Diopside	$CaMgSi_2O_6$	$4(\pm4)\times10^{-16}$	Extrapolated from pH 7 rate	[119, 101, 121, 184, 120, 185, 186]
Enstatite	$Mg_2Si_2O_6$	$2(\pm1)\times10^{-14}$	Extrapolated from pH 7 rate	[187, 188]
Wollastonite	$Ca_2Si_2O_6$	$6(\pm5)\times10^{-15}$	Extrapolated from pH 7 rate	[101, 121, 189, 190]
Hedenbergite	$CaFeSi_2O_6$	$6(\pm4)\times10^{-12}$	Extrapolated from pH 7 rate	[191]
Gehlenite/ akermanite	$Ca_2Al(AlSiO_7)$/ $Ca_2Mg(Si_2O_7)$	1×10^{-14}	Estimated from other sorosilicates	N/A
Mayenite	$Ca_{12}Al_{14}O_{33}$	?	N/A	N/A
Merwinite	$Ca_3Mg(SiO_4)_2$	4.5×10^{-14}	Regressed from other Ca-Mg orthosilicates	[6]
Lime	CaO	3.9×10^{-9}	Extrapolated from pH 2 rate	[205]

Table 5.12: Summary of calculated or reported dissolution rates of selected minerals.

For example, Mg-rich olivines and Ca and Mg-rich pyroxenes have been extensively studied whereas Fe-rich olivines and pyroxenes are rarely studied. This phenomenon of differences in the chemical composition goes some way to explaining the lack of previous research on some key slag phases.

Oxide	**Earth's crust (wt %)**	**Steel slag (wt %)**	**Copper slag (wt %)**
SiO_2	60.6	16.9	35.9
Al_2O_3	15.9	7.5	6.2
FeO	6.7	22.9	33.1
CaO	6.4	34.9	7.1
Na_2O	3.1	0.2	0.5
K_2O	1.8	0.2	1.4
MgO	4.7	7.2	1.8
TiO_2	0.7	0.7	0.4

Table 5.13: Comparison of composition of earth's crust with composition of steel and copper slags

5.3.2 Thermodynamics of dissolution

Dissolution only occurs if the dissolution reaction is thermodynamically favorable. The saturation state of a dissolution reaction is calculated as the difference between the ion activity product (IAP, denoted by Q) and the equilibrium constant (K) for the dissolution reaction. The IAP is calculated using the activities of aqueous ions involved in the dissolution reaction. The IAP and equilibrium constant are related to the Gibbs free energy of the dissolution reaction (ΔG_{diss}) through the law of mass action, shown in Equation 5.10;

$$\Delta G_{diss} = RT \times ln\left(\frac{Q}{K}\right) \tag{5.10}$$

The relationship between dissolution rate and ΔG_{diss}, is non-trivial. However, it is safe to assume that the dissolution rate decreases at more negative values of ΔG_{diss} and reaches zero when ΔG_{diss} is zero. Dissolution is not favored for positive values of ΔG_{diss}.

The mixing of Portland cement and water in concrete results in the rapid increase in concentration of Ca, Si, Na, K, and S ions in the aqueous phase of the binder. As the binder solidifies and hardens, the aqueous phase occupies interstitial pores and is referred to as pore solution. The dissolution rate of any given phase dissolving into the binder pore solution will be a function of the concentration of dissolving ions already in solution. By calculating the equilibrium constant for the dissolution reaction and measuring the concentration of relevant ions in the binder pore solution, the favorability of the dissolution reaction can be determined. In the case of Portland cement pore solution and blended Portland cement pore solution, data on experimentally measured concentrations of various ions as a function of time in the pore solution has been collected by [106]. Additionally, data for alkali activated material (AAM) pore solutions has been collected here [206, 207, 208, 209, 210, 211, 212, 213, 214, 215]. Concentration data for Portland cement, blended Portland cement, and alkali activated material pore solutions is shown in Figure 5-4, with each data point representing a pore solution at a given binder age. The Portland cement concentrations are all for CEM I type Portland cement. The blended Portland cement concentrations are all for CEM I type Portland cement blended with fly ash (FA) in various proportions. AAMs all use ground granulated blast furnace slag (GGBFS) or FA with a NaOH and/or waterglass activator. The emphasis on Na, K, Ca, $SO4^{-2}$, and Si is evident. Na concentrations are higher in alkali activated materials due to the presence of NaOH or sodium silicate activators in most alkali activated materials. Similarly, higher Al concentrations in AAMs are due to the presence of Al in GGBFS and FA. Data for Mg and Fe concentrations are much sparser, possibly due to the fact that the concentrations of these elements are typically below the detection limit of the instrument being used to measure the concentration. The low Fe and Mg concentrations are not due to their absence in Portland cement – Fe_2O_3 is present in C_4AF and Mg is present as an impurity in each of C_3S, C_2S, C_3A, and C_4AF – but rather due to the low solubility of aqueous Fe and Mg species in solution. This topic is revisited in Section 5.5.2. For example, Ca is between 10^4 and 10^5 times more soluble than Mg at pH 13. Calculating reliable ion activity products for the dissolution reactions of Mg

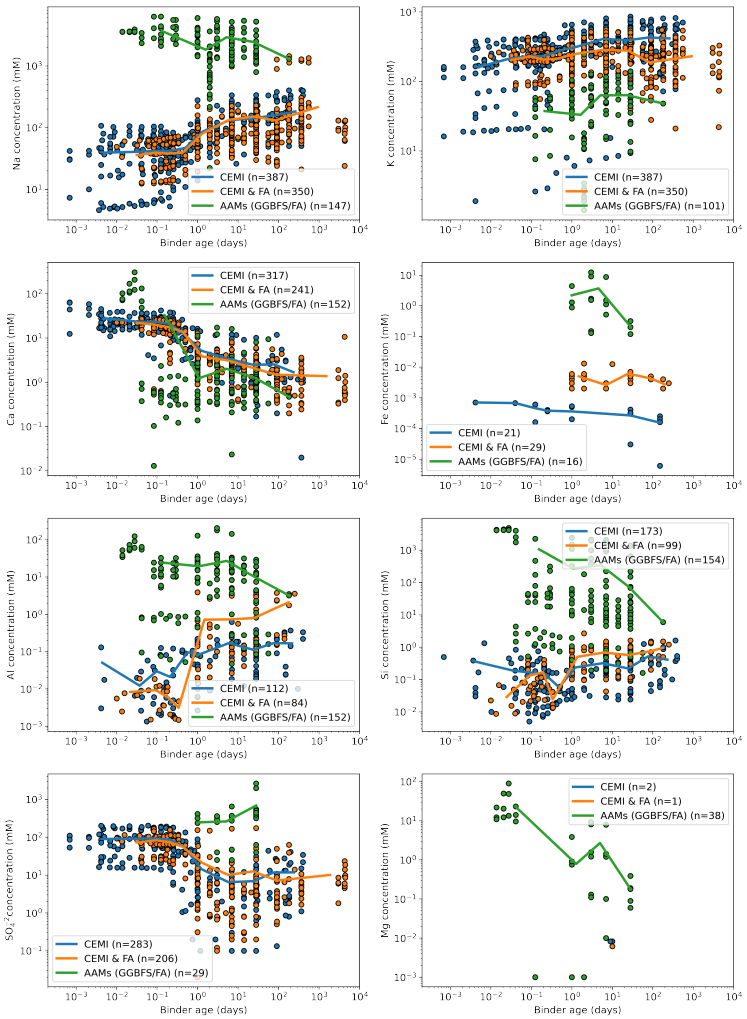

Figure 5-4: Reported concentrations of selected ions in CEM I Portland cement binders, fly ash blended CEM I Portland cement binders, and alkali activated materials. The number of reported concentrations is given in brackets.

and Fe bearing minerals, which are plentiful in steel and copper slags, requires more data for Mg and Fe concentrations. In any case, the dissolution reaction is expected to proceed under conditions close to saturation, except at very early binder ages when ion concentrations and the pH of the pore solution are still low.

For Ca and Si bearing phases, the abundance of experimental data for Ca and Si pore solution concentrations allows the driving force for their dissolution to be calculated. This is shown in Figure 5-5 for all pore solutions for which Ca and Si concentrations are reported, where each individual point represents a single CEM I type Portland cement binder pore solution. The mean value for ΔG_{diss} is shown

in solid black line, with the 5th and 95th percentiles either side. The points for these lines are calculated by taking the average concentration for a range of times by "binning" similar times together. GEM-Selektor v3.3 (http://gems.web.psi.ch/) [9, 10] with PSI-Nagra [4] and Cemdata18 [11] databases were used to calculate ion activity products. The aqueous electrolyte model used to determine the activity of ions in solution was the extended Helgeson form of the Debye-Hückel equation with ion size and extended term parameters of NaOH background electrolyte (å = 3.31 Å and b_γ = 0.098 kg mol^{-1}) [78]. The osmotic coefficient and the Debye-Hückel extended term were used to calculate the activity of water and neutral species respectively. The equilibrium for the dissolution reaction were calculated using the values of the Gibbs free energy of formation for the species involved in the reaction. All Gibbs free energy of formation values were calculated as a function of temperature using the RTParm module in GEM-Selektor v3.3, using the PSI-Nagra and Cemdata18 databases, except for calcio-olivine [216], and β-C_2S and C_3S [204]. No temperature dependence for the Gibbs free energy of formation of β-C_2S and C_3S was calculated. Similar calculations for CEM I blended Portland cement binders are included in the Appendix. Calculations of this type are not possible for AAM binder pore solutions as the aqueous species and reactions products typical of these systems are currently not included in the thermodynamic databases for GEM-Selektor.

Portlandite is supersaturated in most pore solutions across all binder ages. The supersaturation of portlandite at almost all times is expected – portlandite is one of the main reaction products of cement hydration. Similarly, the undersaturation of β-C_2S and C_3S in most or all pore solutions at all times is expected - these are the major phases of Portland cement which dissolve at all binder ages. Values of ΔG_{diss} for γ-C_2S are close to saturation at all binder ages, implying γ-C_2S is a mineral which will dissolve in solution, but is expected to become more easily supersaturated than its more reactive polymorph, β-C_2S. Additionally, γ-C_2S dissolution is more undersaturated at higher temperatures. β-C_2S does not follow this trend due to the fact that the dependence of temperature on the Gibbs free energy of formation of β-C_2S is currently not captured during calculations of the equilibrium constant, K.

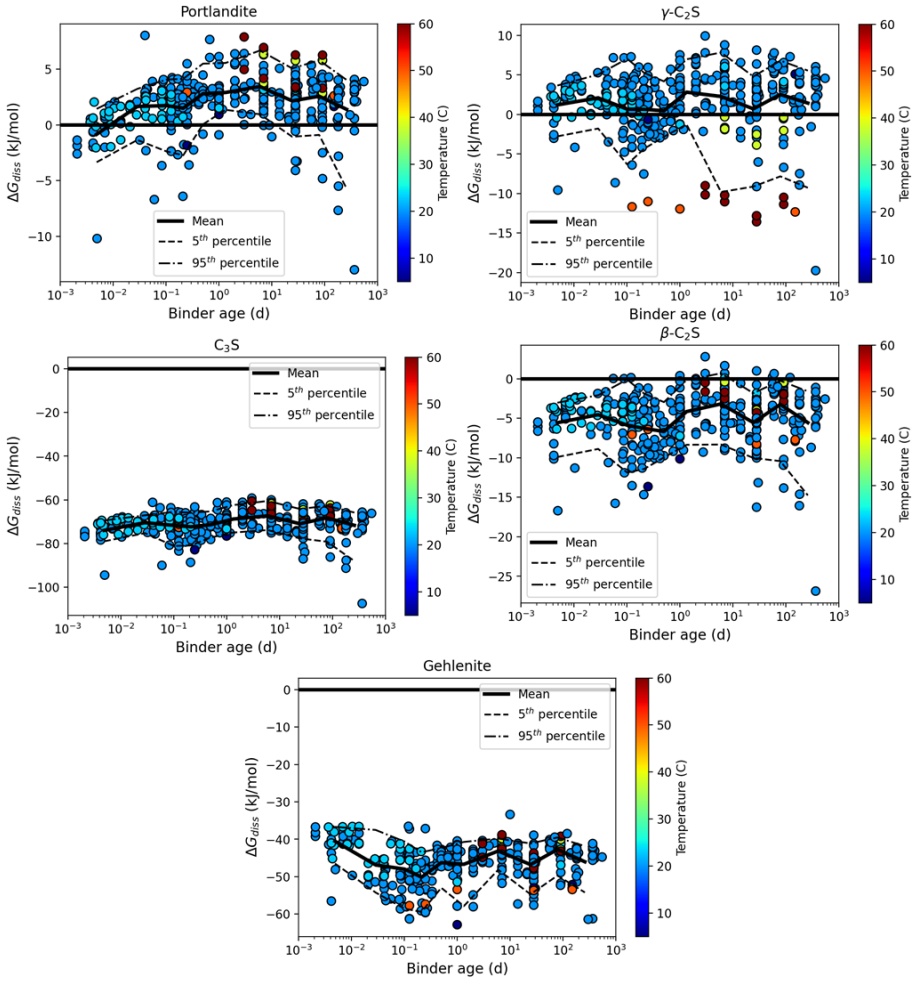

Figure 5-5: Driving force for mineral dissolution reactions in CEM I type Portland cement binders. Each datapoint represents the saturation state of that mineral in a given CEM I type Portland cement binder pore solution for which the concentration of the relevant ions have been experimentally measured.

Beyond the simple criteria of whether ΔG_{diss} is positive or negative, the value of ΔG_{diss} plays a key role in regulating the dissolution rate. Nicoleau et al. measured the dissolution rate of C_3S and β-C_2S as a function of ΔG_{diss} and interpreted their results in the context of C_3S hydration as measured by calorimetry [204]. The dissolution rate of C_3S was found to decrease by 4 orders of magnitude going from ΔG_{diss} of -30 kJ/mol to -3 kJ/mol. In the context of cement hydration, a rapid increase in the concentrations of Ca^{2+}, OH^-, and $H_2SiO_4^-$ leads to a corresponding reduction in the driving force for C_3S dissolution. This is manifested in the calorimetry curve of C_3S hydration, which shows a high rate of heat released at early age, before decaying away

quickly. An understanding of how the dissolution rate of a phase changes as a function of ΔG_{diss} is crucial in devising an accurate model of its dissolution over time in a binder pore solution. In fact, advances in understanding how C_3S dissolution slows as a function of its saturation state in solution has greatly improved our understanding of the induction period of cement hydration.

It is worth noting that the previously derived dissolution rates in Section 5.3.1 were collected under far from equilibrium conditions, and to fully account for their dissolution rates in concrete pore solutions, an understanding of how the dissolution rate changes as a function of saturation state would be required. This concept is returned to in Section 7.2.

5.4 A model for cement and slag hydration

Many of the above ideas - Portland cement hydration models, dissolution kinetics of slag phases, and synergistic reaction product formation - can be illustrated through a simple hydration model that encompasses all three of these aspects. A model of this kind brings us closer to being able to identify appropriate beneficial use concrete applications for a given slag.

The objective of the model outlined in the section is to determine the reaction product assemblage of Portland cement based mortars as a function of mortar age. A model of the evolution of the reaction product assemblage for a given mortar can be a powerful tool – the total volume of reaction products and the porosity of the mortar correlates with compressive strength in certain cases [2]. A model that is capable of describing the reaction product assemblage as a function of time has 2 components. First, the phase composition of the precursors (Portland cement and slag in this case) and a description of the extent of dissolution of all phases in the precursors as a function of mortar age is required. And second, the ability to calculate the thermodynamic equilibrium of a system with given input composition and temperature is necessary. With a database that includes thermodynamic data for all possible reaction products, calculations of the thermodynamic equilibrium of

a system are accurate in determining the phase composition of the resultant aqueous and solid phases. GEMS is a geochemical modeling software which uses a Gibbs free energy minimization approach whereby the total bulk input composition is used to calculate the reaction product assemblage. The reaction product assemblage is identified as the combination of phases which minimizes the total Gibbs free energy of the system while maintaining mass and charge balance of the whole system through the law of mass action. The 2 components of this model will be outline in the following sections.

5.4.1 Dissolution kinetics

As mentioned in the abstract, the framework outline in this chapter will be demonstrated on Portland cement-steel slag mixes. Specifically, the steel slag of interest is EAF Slag C from Table 5.6. This slag was chosen due to its high content of reactive phases, namely mayenite, periclase (RO phase), and β-C_2S. In the following sections, the kinetics of dissolution of the 2 components of the mix, Portland cement and slag, will be described.

Portland cement hydration

For a description of Portland cement hydration, the model of Parrot allows the extent of Portland cement consumption as a function of time to be calculated [3] and has been used successfully by others [8, 179]. Parrot's model is valid for Portland cement mortars within a narrow range of liquid-to-solid ratios and humidity. It assumes that the rate-limiting process is due to one of mass transport, nucleation and growth of reaction products, or the formation of a hydration shell;

Mass transport:

$$R_{1,i,t} = \frac{K_{1,i}}{N_{1,i}}(1-\alpha_{t,i})(-ln(1-\alpha_{t,i}))^{1-N_{1,i}} \tag{5.11}$$

Nucleation and growth:

$$R_{2,i,t} = \frac{K_{2,i}(1-\alpha_{t,i})^{2/3}}{1-(1-\alpha_{t,i})^{1/3}} \tag{5.12}$$

Hydration shell formation:

$$R_{3,i,t} = K_{3,i}(1 - \alpha_{t,i})^{N_{3,i}} \tag{5.13}$$

where $R_{1,i,t}$, $R_{2,i,t}$, and $R_{3,i,t}$ are the rates of each process at time t for phase i, $\alpha_{t,i}$ is the extent of dissolution or consumption of phase i at time t, and $K_{1,i}$, $N_{1,i}$, $K_{2,i}$, $K_{3,i}$, and $N_{3,i}$ are empirical parameters for phase i. Parrot's model was developed to determine the consumption of the 4 major phases of Portland cement: C_3S, C_2S, C_3A, and C_4AF. The extent of hydration of phase i at time t, $\alpha_{t,i}$ is given by the extent of hydration at time $t-1$, $\alpha_{t-1,i}$;

$$\alpha_{t,i} = \alpha_{t-1,i} + \Delta t.min(R_{1,i,t-1}, R_{2,i,t-1}, R_{3,i,t-1}).\beta.\gamma.\frac{A}{A_0} \tag{5.14}$$

where β is the water to cement ratio parameter given by $\beta = \left(1 + \frac{10}{3}(H_i w - \alpha_{t-1,i})\right)^4$ if $\alpha_t > H_i w$, otherwise, $\beta = 1$, where H_i is an empirical parameter for phase i, and w is the water to cement mass ratio. The relative humidity parameter, γ, is given by $\gamma = \left(\frac{RH-0.55}{0.45}\right)^4$, where RH is the relative humidity. The term $\frac{A}{A_0}$ normalizes the surface area of the cement being to used with respect to the cement used by Parrot, where A (m^2/kg) is the Blaine surface area of the cement and A_0 is the reference surface area of cement (385 m^2/kg). The values of the empirical parameters K_1, N_1, K_2, K_3, N_3, and H for all 4 phases are shown in Table 5.14.

	C_3S	**C_32**	**C_3A**	**C_4AF**
K_1	1.5	0.5	1	0.37
N_2	0.7	1.0	0.85	0.7
K_2	0.05	0.006	0.04	0.015
K_3	1.1	0.2	1	0.4
N_3	3.3	5	3.2	3.7
H	1.8	1.35	1.6	1.45

Table 5.14: Empirical parameters for Portland cement hydration. Parameters are from [3, 7]

The extent of dissolution of C_3S, C_2S, C_3A, and C_4AF is determined up to a mortar age of 1000 days using Parrot's model, as shown in Figure 5-6. The composition of

the Portland cement used here is included in the Appendix of this thesis (Table A.5). The minor phases in Portland cement either dissolve instantly upon contact with water (CaO, MgO, gypsum, K_2SO_4, and Na_2SO_4) or are assumed to be impurities in the major Portland cement phases and dissolve at the same rate as the C_3S ($CaCO_3$, Na_2O (C), K_2O (C), MgO (C), and SO_3 (C)). This approach is identical to the one used in [8]. The limitation of this model is inherent in the way it was developed — to match experimental data for specific Portland cement mixes with limited broader use. The model is not valid for major changes to the Portland cement content, relative humidity, temperature, or water to cement mass ratio.

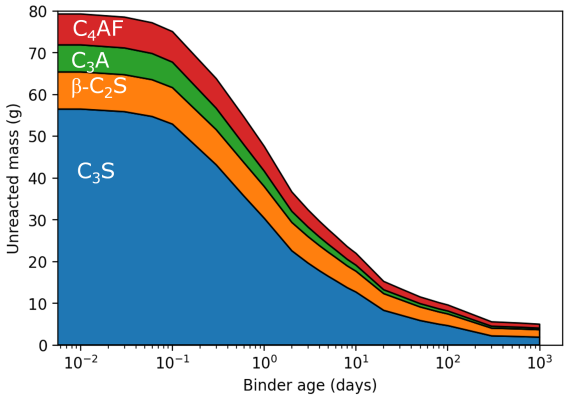

Figure 5-6: Portland cement hydration kinetics calculated using the model from [3], assuming 80 g of cement.

Slag dissolution kinetics

As mentioned above, for demonstration purposes, the slag of interest is EAF Slag C from Table 5.6. Unlike for Portland cement, there exists no empirical model describing the consumption of steel slag in a Portland cement mortar. The dissolution of the phases in the slag of interest are modeled here using their dissolution rates. The extent of dissolution of these phases can be modeled using the total surface area of each phase and the surface area-normalized dissolution rate of that phase. The total quantity of dissolved material can be calculated as a function of mortar age in this way. This approach is subject to several broad assumptions;

- each phase is assumed to be equally available for dissolution,

- each phase has the same particle size distribution as the total slag (log-normal distribution between 1 and 100 μm), the same specific surface area as the total slag, and particles are spherical
- dissolution of each phase is the rate-limiting process
- the dissolution rate of each phase is constant over the lifetime of the binder and is unaffected by the composition of the aqueous environment into which it is dissolving

The first of these assumptions is unlikely to differ much from reality. Some phases may be prevented from dissolving due to being surrounded by other phases. This is particularly true for phases such as wüstite and spinel phases which tend to solidify first and are later surrounding by silicate matrices during slag cooling. The second assumption is also a reasonable assumption, although phases of lower hardness are easier to grind and may possess a smaller particle size than harder phases. Slag particles are not spherical in reality and a roughness factor is used to reconcile the theoretical surface area of spherical slag particles with the experimentally determined surface area of the slag particles. The third assumption is more problematic. Mass transport or nucleation and growth of reaction products are often assumed to be the rate-limiting processes of beyond the early stages (<12 hours) of cement hydration. However, without a detailed description of the evolution of the microstructure of the mortar, it is not possible to quantify the rates of these processes. The fourth and final assumption also represents a sharp divergence from what is expected to occur in reality. Dissolution rates are a function of solution pH, ionic strength, and temperature. The properties of the aqueous phase of Portland cement mortars all evolve over the lifetime of the mortar. Furthermore, the dissolution rate is a function of the thermodynamic driving force for dissolution, as discussed in Section 5.3.2. The saturation state of a dissolution reaction is calculated as the difference between the ion activity product (IAP) and the equilibrium constant (K) for the dissolution reaction. The IAP is calculated using the activities of aqueous ions involved in the dissolution reaction. The IAP and equilibrium constant are related to the Gibbs free

energy of the dissolution reaction through the law of mass action. The relationship between dissolution rate and the saturation state of the solution is non-trivial but is known to strongly affect the dissolution rate of cement phases [204]. However, the relationship between dissolution reaction saturation state and dissolution rate is not well understood and has only been studied for a small a number of phases. For this reason, the dissolution rates of the slag phases are assumed to remain high throughout the lifetime of the mortar, corresponding to dissolution rates measured at far from equilibrium under highly dilute conditions.

Dissolution rates for all relevant phases were compiled in Table 5.12. The evolution of the quantity of each phases as a function of time is shown in Figure 5-7. The extent of dissolution of each phase was calculated at the same time points as were used in Figure 5-6. Of the 0.45 g of RO phase, 0.4 g is assumed to be wüstite and 0.05 g is assumed to be periclase based on typical concentrations of Fe and Mg in RO phase. The dissolution rate of β-C_2S is assumed to be 1×10^{-10} mol cm^{-2} s^{-1}, based on measurements from [204]. The dissolution rate of mayenite is not known, but mayenite is known to induce flash setting in cementitious systems, implying a very fast dissolution rate. The mayenite dissolution rate was assumed to be 1×10^{-9} mol cm^{-2} s^{-1}. Wüstite does not dissolve, while mayenite, β-C_2S, and periclase undergo rapid dissolution. At later ages, the dissolution of calcio-olivine becomes significant.

The dissolution kinetics of Portland cement and the EAF slag indicate the extent of dissolution of all phases present as a function of time. The quantity of dissolved phases can be broken down into their constituent oxides (Na_2O, K_2O, CaO, MgO, FeO, Fe_2O_3, Al_2O_3, and SiO_2), i.e. 1 mole of dissolved C_3S equates to 3 moles of CaO and 1 mole of SiO_2. By comparing the quantity of each available oxide as a function of time, the relative over- or under-abundance of a given oxide relative to pure Portland cement systems can be identified. The CaO/Al_2O_3 and SO_3/Al_2O_3 molar ratios of a 100 % Portland cement mix (PC mix) and an 80% Portland cement, 20% EAF slag mix (PC+EAF mix) can be compared, as shown in 5-8. The PC+EAF mix is enriched in CaO and Al_2O_3 relative to the pure Portland cement binder. The relative enrichment of these oxides is due to the rapid dissolution of mayenite from the

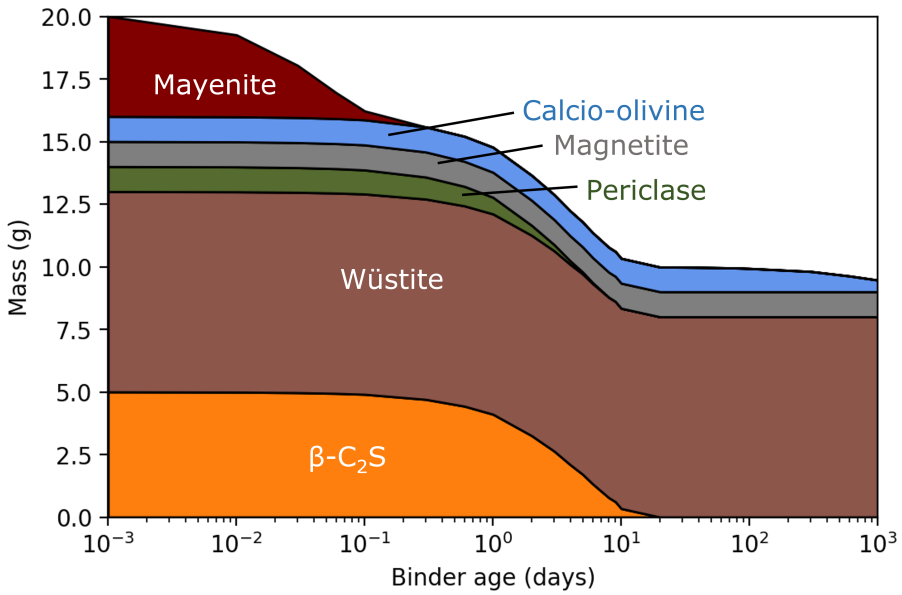

Figure 5-7: Dissolution kinetics of individual phases from EAF Slag C, assuming 20 g of slag.

slag, as shown in 5-7. For this reason, a third mix was proposed. This mix addresses the Al_2O_3 enrichment of the PC+EAF mix by adding gypsum. This mix, entitled PC+EAF+Gyp, consists of 78.7 wt% Portland cement, 19.7 wt% EAF slag, and 1.6 wt% gypsum. This results in a SO_3/Al_2O_3 molar ratio which more closely resembles the Portland cement binder at later ages, as shown in Figure 5-8.

5.4.2 Thermodynamic simulations of reaction product assemblage

The kinetic models outline in the previous section describe the dissolved quantity of each phase as a function of mortar age. The dissolved quantity at a series of timepoints can be used as the input for thermodynamic simulations of the system. In other words, the unreacted quantities of each phase are held apart from the thermodynamic simulations — only the dissolved content is used as input. The thermodynamic simulation determines the combination of solid phases and the composition of the aqueous phase that minimizes the total Gibbs free energy of the system. It is therefore assumed that the aqueous phase is in equilibrium with the solid phases at all times.

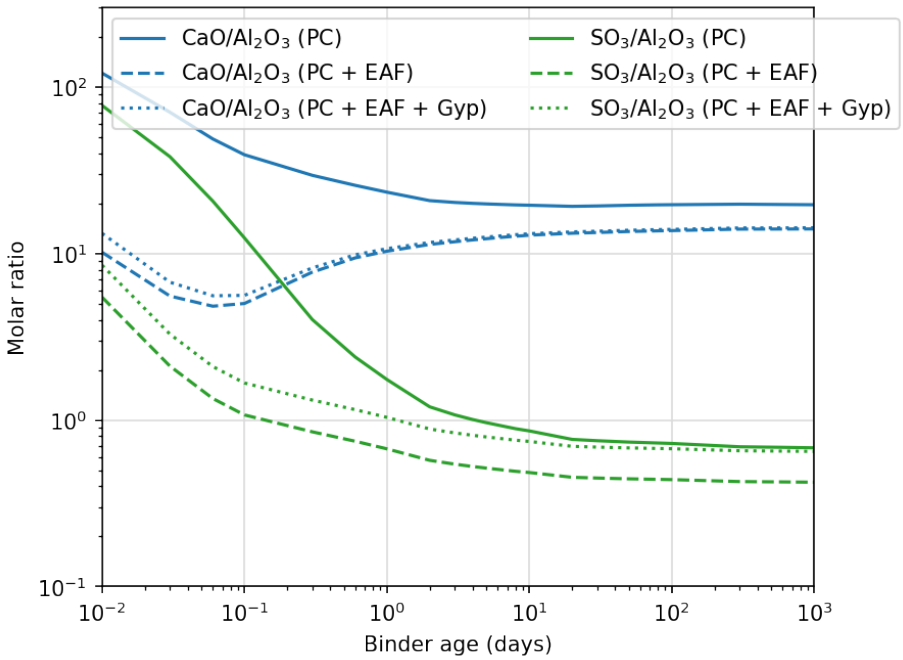

Figure 5-8: Molar ratios for: a 100% Portland cement mix (PC); an 80% Portland cement with 20% EAF slag mix (PC+EAF); and a 78.7 wt% Portland cement, 19.7 wt% EAF slag, and 1.6 wt% gypsum mix (PC+EAF+Gyp). Gypsum was added to more closely match the stoichiometry of the Portland cement mix.

This assumption is not always valid as the aqueous phase is typically oversaturated with respect to hydrate reaction products at early mortar ages. At later mortar ages, solid and aqueous phases approach equilibrium. 24 simulations were performed at time points from 0.01 to 365 days. For each simulation, the input quantities were generated using the models outlined above for Portland cement and slag dissolution. Input quantities for the simulations of the PC, PC+EAF, and PC+EAF+Gyp mixes are included in Appendix A.

The simulations were performed using GEM-Selektor v3.3 (http://gems.web.psi.ch/) [9, 10] with PSI-Nagra [4] and Cemdata18 [11] databases. The aqueous electrolyte model used to determine the activity of ions in solution was the extended Helgeson form of the Debye-Hückel equation with ion size and extended term parameters of NaOH background electrolyte (å = 3.31 Å and $b_\gamma = 0.098$ kg mol^{-1}) [78]. The osmotic coefficient and the Debye-Hückel extended term were used to calculate the activity of water and neutral species respectively. Thermodynamic simulations of this kind are

only valid through judicious choice of which reaction products are typically observed to form in real systems. Certain reaction products may be thermodynamically predicted to be present, but in practice are not observed in real cementitious systems due kinetic constraints. For these simulations, the formation of the following phases was forbidden; quartz, goethite, hematite, thaumasite, C_4AH_{19}, C_4AH_{13}, C_4AH_{11}, gibbsite, monosulph-FeAl, and ettringite-FeAl, as suggested by [11]. Some of these phases were excluded in favor of more disperse counterparts whose inclusion produces simulations which better match experimental observations (e.g. gibbsite) [11].

5.5 Discussion

5.5.1 Reaction product assemblage

The results of the thermodynamic simulations for all 3 mixes are shown in Figure 5-9.

The reaction product assemblage of the 3 binders is similar, although there are notable differences. The volumes of the pore solution and the precursors decrease monotonically. The volume of C-S-H is similar in all binders. The other major phases in all cases are portlandite ($Ca(OH_2)$), hydrotalcite, hydrogarnet, ettringite ($Ca_6Al_2(SO_4)_3(OH)_{12}{\cdot}26H_2O$), and AFm-phases (primarily $Ca_4Al_2SO_{10}(H_2O)_{12}$).

At early age, the PC+EAF and PC+EAF+Gyp mixes show a higher ettringite ($Ca_6Al_2(SO_4)_3(OH)_{12}{\cdot}26H_2O$) content. This reaction is the result of SO_3 from the rapidly dissolving gypsum (Ca_2SO_4) in the Portland cement reacting with Al_2O_3 from the rapidly dissolving mayenite ($Ca_{12}Al_{14}O_{33}$ in the EAF slag. In the PC+EAF+Gyp, there is an even greater extent of ettringite formation at early ages due to the presence of additional gypsum in that mix. At later ages, the PC+EAF mix shows a greater quantity of AFm-phases (primarily $Ca_4Al_2SO_{10}(H_2O)_{12}$) than the PC mix. This is most likely due to the availability of Al in the mixed binder due to mayenite dissolution – AFm-phases have a higher Al content relative to ettringite. The incorporation of additional Ca into these AFm-phases also likely accounts for the lower portlandite content in the mixed binder compared to the Portland cement binder. At later ages,

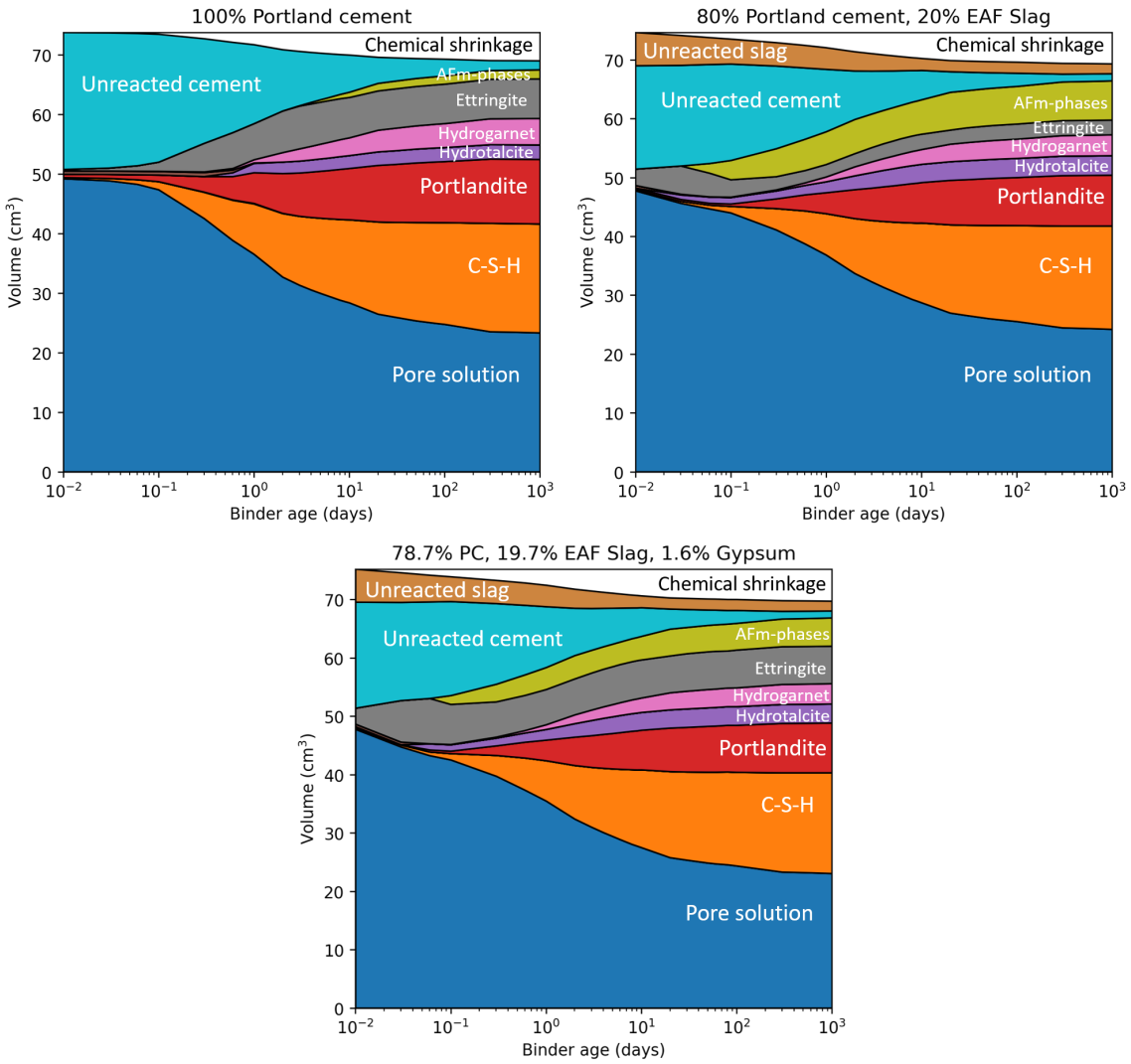

Figure 5-9: Reaction phase assemblage of the PC, PC+EAF, and PC+EAF+Gyp mixes.

the PC+EAF+Gyp mix shows a reduction in the quantity of AFm-phases relative to the PC+EAF mix due to greater quantity of gypsum resulting in a preference for ettringite.

One consequence of differences in the reaction product assemblage is the impact on the porosity of the binder. Porosity is measured by the total pore volume – the volume occupied by the pore solution and by the reduction in the binder volume due to chemical shrinkage. In the case of all 3 binders, the porosity is calculated as the sum of these 2 components. The porosity as a function of time for each mix is shown in Figure 5-10. The porosity of the PC+EAF and PC+EAF+Gyp mixes decreases

much more rapidly at early ages than the PC mix. This is a result of the dissolution of the most reactive EAF slag phases which contribute to early formation of ettringite. This rapid early reduction in porosity is reminiscent of the so-called flash-setting in mayenite containing mortars, in which rapid early reaction product formation can have a deleterious impact on concrete properties. At later ages, the PC binder ultimately achieves a lower porosity and denser microstructure than the PC+EAF mix. This is due to the inert phases of EAF slag remaining unreacted at later ages and not contributing to reaction product formation, unlike the PC mix in which all cement phases continue to react at later binder ages. However, the PC+EAF+Gyp mix does achieve a reduction in porosity similar to the PC mix. The introduction of gypsum into this system allowed the conversion of AFm-phases present in the PC+EAF mix to be converted into the more expansive ettringite, densify the microstructure and reducing the pore volume. Given the correlation between compressive strength and porosity [2], modeling the porosity in this way offers insight into how mix design may ultimately impact the mechanical properties of the concrete. Modeling the kinetics and the thermodynamics of reaction product formation as described above can act as a powerful tool in this regard. It should be noted that the addition of gypsum to Al_2O_3-rich industrial wastes has been demonstrated to result in a binder with good mechanical properties [125].

5.5.2 Identifying reactive slags

The framework developed above was only implemented for 1 slag, EAF Slag C from Table 5.6. However, it is worth exploring how we might expect the other model slags (Tables 5.2, 5.4, 5.6, and 5.8) to perform and to consider more broadly which slags hold the greatest potential for use in concrete. In order for a precursor to contribute to the formation of reaction products, it is necessary that the several conditions be met. First, the precursor must dissolve appreciably. The extent to which this condition is met can be evaluated from the dissolution rates of the constituent phases of the precursor. Second, dissolved ions must be soluble enough in the concrete pore solution such that they can diffuse away from the surface of the dissolving phase and

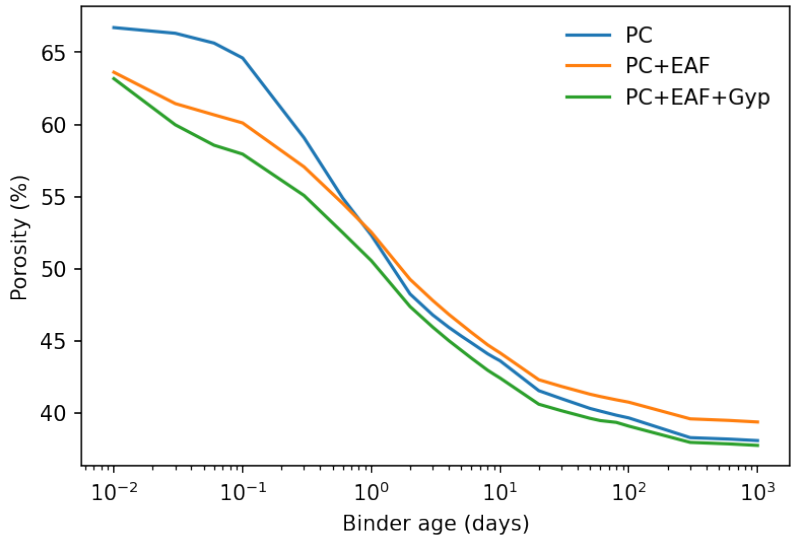

Figure 5-10: Porosity of the PC (100% PC), PC+EAF (80 wt% PC, 20 wt% EAF slag), and PC+EAF+Gyp (78.7 wt% PC, 19.7 wt% EAF slag, 1.6% gypsum) mixes.

form reaction products elsewhere in the concrete. Third, the dissolving ions must be capable of becoming supersaturated in solution with respect to a hydrate reaction product.

The simplest of these conditions to consider is the solubility of the dissolving ions. Portland cement-based concrete has a high pH (>12.5) over the lifetime of the concrete. All steel slags are comprised primarily of 8 oxides – SiO_2, Al_2O_3, Fe_2O_3, FeO, CaO, MgO, MnO, and TiO_2. The solubility of these oxides (with the exception of Ti for which thermodynamic data was not available) is shown in Figure 5-11. The solubility of Mn, Mg, and Fe(III) is low between pH values of 13 and 14. Si, Al, Fe(II), and Ca have higher solubility in this range. This indicates that Si, Al, Fe(II), and Ca bearing phases are more likely to be soluble and capable of contributing to reaction product formation.

In terms of reaction product formation, Si, Al, Fe(II), and Ca all contribute to reaction product formation, particularly Si, Al, and Ca. The solubility of Si, Al, and Ca, as well as their propensity to form reaction products is unsurprising – these elements dominate the chemistry of Portland cement. Fe(II) is a less common species in Portland cement-based concretes and less is known about the final reaction products it will form. Recent studies on inorganic polymers with Fe(II) rich precursors have

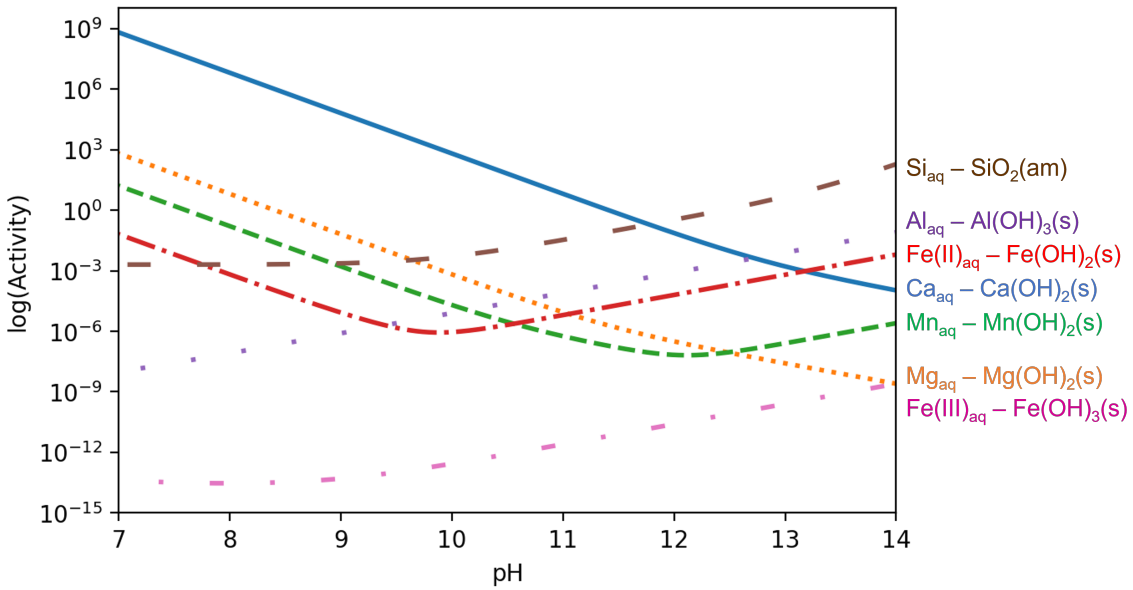

Figure 5-11: Solubility of selected elements between pH 7 and pH 14. Solubility is based on thermodynamic data from [4].

revealed that Fe(II) undergoes oxidation to Fe(III), which is partially incorporated into a silicate network [127]. In general, the reaction product formation potential of Fe(II) is unclear.

Given that Si, Al, Fe(II), and Ca bearing phases are expected to be soluble and to form reaction products, the final criterion to consider is the dissolution rates of these phases. The kinetic models shown earlier in the chapter demonstrate that dissolution rates of at least $1x10^{-12}$ (mol cm^{-2} s^{-1}) are required in order to bring about substantial dissolution of the phase. There is no simple correlation between chemistry and dissolution rate of a phase. For example, the dissolution rates of the polymorphs of Ca_2SiO_2 can vary by several orders of magnitude [62, 204]. However, silicate connectivity is often indicative of the reactivity of a phase. Silicate phases with isolated silica tetrahedra (e.g. β-C_2S, calcio-olivine) are typically more reactive than silicate phases polymerized silica tetrahedra. The silicate cement phases (β-C_2S and C_3S) are reactive for this reason and because they are high temperature polymorphs which are thermodynamically unstable at room temperature, resulting in higher thermodynamic driving forces for dissolution. Stabilizing these phases through the addition of impurities can be an effective strategy in improving overall slag reactivity. For

example, a series of ions that stabilize the more reactive β-C_2S over calcio-olivine have been identified (Ba^{+2}, K^{+}, Sr^{+2}, Cr^{+6}, P^{+5}, and B^{+3}) [217]. Beyond the unstable, cementitious silicates, the only other reactive phases are the simple oxides (CaO, MgO), and the calcium aluminates (mayenite, brownmillerite, and C_3A).

Returning to the aforementioned model slags (Tables 5.2, 5.4, 5.6, and 5.8) is now possible to evaluate usefulness of these slags as a partial cement replacement. Copper slags are dominated by Si and Fe oxides. Fayalite and spinel/magnetite are the most commonly reported phases. These phases both contain Fe(II) and Si but are unreactive. Glass is reported in 75% of copper slags and may react appreciably and the reactivity of a copper slag will likely ultimately depend on its amorphous content. Copper Slags A and C should be considered to be inert but Slag B may contain a high enough glass content to be considered reactive. The presence of β-C_2S, dicalcium ferrite, lime, and C_3S in BOF Slag A, B, and C endow them with cementitious properties. However, there are challenges associated with the expansive formation of $Ca(OH)_2$ due to hydration of CaO. The phase composition of BOF slag is more predictable than other steel slags, and the use of BOF slag in concrete is an area of research that warrants greater attention. EAF slags are more variable in composition than BOF slags. The reactivity of EAF slags is largely dependent on the quantities of reactive calcium aluminates, like mayenite and C_3A. For example, EAF Slags A and B are dominated by RO phase and gehlenite, respectively, making them inert. EAF Slag C contains a 20 wt% mayenite and 25 wt% β-C_2S. Mayenite and β-C_2S are both reactive and EAF Slag C is likely to be cementitious. Finally, LF slags also have highly variable phase composition. Similar to EAF slags, the reactivity of LF slags are largely determined by the content of calcium aluminates. LF Slag A and LF Slag B are dominated by calcio-olivine and quartz, respectively, and and are therefore largely inert. LF Slag C contains the highly reactive mayenite, making it a potentially useful cement replacement.

5.6 Chapter Summary

This chapter contributes towards the development of a framework that estimates the reaction kinetics of both Portland cement and crystalline slags (steel or copper slag) and models reaction product formation. The first research question was answered through a comprehensive review of the phase composition and microstructure of the each slag type. From this review, a subset of the most commonly reported phases were identified and dissolution rates of these minerals were compiled. Dissolution rates were tabulated in various ways: using directly reported rates at the pH of interest; extrapolating rates from lower pH values to the pH of interest; and based on dissolution rates for structurally and chemically similar phases. Finally, this dissolution rate data was combined with a model for cement hydration kinetics to simulate the evolution of the reaction product assemblage. This procedure was carried out for 3 binders; 2 mixed Portland cement-slag binder and a pure Portland cement binder. This framework offers a simple methodology for identifying potential synergy between precursors on the basis of their phase composition.

Chapter 6

pH calibration for alkali solutions

This chapter presents a methodology for calibrating pH meters in highly alkaline solutions such as those relevant to cementitious systems. This methodology uses an extended form of the Debye-Hückel equation to generate a calibration curve of pH vs. the measured electrochemical potential (mV) based on a series of aqueous alkali hydroxide solutions of known concentrations. This methodology is compared with the 'built-in' process of calibration based upon pH 4, 7, and 10 standard solutions. The built-in calibration process underestimates the real pH values by up to 0.3 log units, which is attributed to the alkali error. A spreadsheet for determining the calibration curve and its application to pH meter readings is provided as Supporting Information with [218]. The implications of improperly calibrated pH meters on interpreting solution chemistry in cementitious systems are discussed.

This chapter is adapted from the following publication:

> Brian Traynor, Hugo Uvegi, Elsa Olivetti, Barbara Lothenbach, and Rupert J Myers. Methodology for pH measurement in high alkali cementitious systems. Cement and Concrete Research, 135(May):106122, 2020 [218].

6.1 Introduction

Measurement of pH is a quick, simple and cost-effective technique that is fundamental to analytical chemistry and widely used in cement science. Fresh Portland

cement concrete typically has a pH $>$ 13 [8]. Maintaining such a high pH is essential to ensure passivation of steel in reinforced concrete, thereby preventing structural deterioration [219, 220]. The pH of the activator solution in an alkali-activated material plays a critical role in precursor dissolution [212, 221], and high pH solutions ($>$ 13) are typically employed for this purpose [50]. In both Portland cement and alkali-activated material systems, the formation of reaction products has also been shown to depend on pH [222, 223, 224, 225].

Calibration of a pH meter is necessary for accurate pH measurements. pH meters are typically calibrated using standard solutions with pH values of 4, 7, and 10 - a process we refer to here as the 'built-in' pH meter calibration. Saturated aqueous $Ca(OH)_2$ solution may be used as a pH 12.45 standard (at 25°C) [226]. However, these pH values are below the pH range of most cementitious systems; therefore, using the built-in calibration in cementitious systems will likely lead to systematic pH measurement errors. Through appropriate selection of solutions of known concentration, pH meters can be accurately calibrated to higher pH. Although versions of this methodology have been used for years in analyses of cementitious systems [8, 227, 228, 229, 230, 231, 232], it has been poorly explicitly disseminated and there has been relatively little uptake of it among the broader cement science community. This communication is intended to clarify this methodology to the cement science community at large. As such, a pH calculator for NaOH and KOH solutions as a function of temperature and concentration is included in the Supporting Information and the relevant physical chemistry concepts underpinning these calculations are discussed here.

a_i	Activity of ion i
b_i	Molality (mol kg^{-1}) of ion i
b_0	Standard molality, defined as 1 mol kg^{-1}
γ_i	Activity coefficient of ion i
z_i	Charge on ion i
I	Ionic strength, $= \frac{1}{2}\sum_i b_i z_i^2$ (mol kg^{-1})
$\dot{a}$	Distance of closest approach parameter of interacting ions in Debye-Hückel equation (Å)
b_γ	Semi-empirical parameter in extended Debye-Hückel equation (kg mol^{-1})
A_γ	Electrostatic parameter in Debye-Hückel equation (kg$^{1/2}$ mol$^{-1/2}$)
B_γ	Electrostatic parameter in Debye-Hückel equation (kg$^{1/2}$ mol$^{-1/2}$ Å^{-1})
x_{jw}	Amount of water, parameter in Debye-Hückel equation (mol)
X_w	Total amount of all species in the aqueous phase, parameter in Debye-Hückel equation (mol)
M_i	Molarity (mol L^{-1})

Table 6.1: Nomenclature of terms.

6.2 Background

6.2.1 Activity of non-ideal solutions

We begin the description of our methodology to calibrate pH meters by expressing the acidity of a solution using pH values (Equation 6.1):

$$pH = -log_{10}(a_{H^+}) = -log_{10}\left(\gamma_{H^+}\frac{b_{H^+}}{b_0}\right) \tag{6.1}$$

where a_{H^+} is the activity of aqueous H^+, b_{H^+} is the molality of aqueous H^+ (mol kg^{-1}, i.e., mol of aqueous H^+ per kg of solvent), b_0 is the standard molality which is defined as 1 mol kg^{-1} (included to make the activity dimensionless), and γ_{H^+} is the activity coefficient of aqueous H^+. Activity is a measure of the effective concentration of an ion in solution, accounting for non-idealities that arise in real solutions. Molality is the preferred thermodynamic expression for concentration due to its independence of temperature and pressure, unlike molarity (mol L^{-1}).

Deviations between activity and concentration arise from electrostatic interactions among ions in aqueous ionic solutions. Long range inter-ionic coulombic attractions

affect ion activity predominantly at low concentrations, whereas short-range ion-ion and water-ion solvation interactions have additional effects at higher concentrations. Short-range ion-ion interactions (ion association) decrease ion activity through formation of ion-ion pairs, reducing the effective number of ions in solution. Water-ion solvation interactions (ion hydration) increase activity by effectively reducing the amount of solvent. In highly dilute aqueous environments, the difference between concentration and activity is negligible.

Debye-Hückel (DH) theory [233] was developed to calculate the mean activity coefficients of ions as a function of the concentration of ions in aqueous ionic solutions. DH theory as originally developed is applicable to dilute aqueous ionic solutions, in which short range interactions are ignored by assuming a structureless solvent, and where the primary interactions between ions are long-range Coulombic forces. The theory results in the Debye-Hückel equation (Equation 6.2), which we define here using molalities:

$$log_{10}\gamma_i = \frac{-A_\gamma z_i^2 \sqrt{I}}{1 + \dot{a} B_\gamma \sqrt{I}} + log_{10}\frac{x_{jw}}{X_w} \tag{6.2}$$

where z_i is the charge of ion i in solution, $\dot{a}$ (Å) is the average distance of closest approach of two ions of opposite charge, I (mol kg^{-1}) is the ionic strength (defined in Table 6.1), and A_γ (kg$^{1/2}$ mol$^{-1/2}$) and B_γ (kg$^{1/2}$ mol$^{-1/2}$ Å^{-1}) are parameters dependent on the temperature, density, and relative permittivity of the solvent (see Supporting Information). The average distance of closest approach, $\dot{a}$, does not in reality represent the sum of the ionic radii of the two ions, and in practice is adjusted to provide a best fit for the aqueous ionic solution of interest [78]. The second term in Equation 6.2 contains the amount of water, x_{jw} (mol), and the total amount of species in the aqueous phase, X_w (mol) and changes the units of γ_i from molar fraction to molal fraction, aligning with our definition of activity. A more detailed derivation and explanation of this equation and related terms may be found in [234]. The ionic strength is a measure of the molality of fully dissociated ions in solution, noting that only in very dilute solutions can salts be assumed to be completely dissociated. Equation 6.2 is accurate in solutions up to moderate ionic strength, I $\leq$ 0.1 mol kg^{-1}

[235].

Versions of the Debye-Hückel equation with an extended term have been used by researchers to extend the range of ionic strengths over which Debye-Hückel theory is valid. The Davies' equation is defined in Equation 6.3:

$$log_{10}\gamma_i = -0.5z_i^2\left(\frac{\sqrt{I}}{1+\sqrt{I}} - 0.3I\right) + log_{10}\frac{x_{jw}}{X_w} \tag{6.3}$$

where the symbols have the same definitions as before. Like the DH equation, the Davies' equation calculates a mean activity coefficient for dissociated ions in an aqueous ionic solution. The Davies' equation extends the applicability of the DH equation up to moderate ionic strengths (I $<$ 0.1 mol kg^{-1}) [8]. It is worth noting that the range of ionic strengths over which the various forms of the DH equation is system dependent, with the Davies' equation being valid up to ionic strengths of 0.7 mol kg^{-1} in some cases [8]. Helgeson extended the DH equation with a linear term [78];

$$log_{10}\gamma_i = \frac{-A_\gamma z_i^2\sqrt{I}}{1+\dot{a}B_\gamma\sqrt{I}} + b_\gamma I + log_{10}\frac{x_{jw}}{X_w} \tag{6.4}$$

where b_γ (kg mol^{-1}) is a semi-empirical parameter, known as the extended term. In his model, a common distance of closest approach was assumed by Helgeson for all ions in a given aqueous ionic solution - values of $\dot{a}$ were calculated for various solutions, with $\dot{a}$ taking a common value for all ions in that solution. This assumption makes the Helgeson extension to the DH equation more accurate in solutions in which the primary salt concentration exceeds that of other aqueous ions. Additionally, the effects of short-range water-ion solvation interactions are captured by the extended term, b_γ (kg mol^{-1}). Helgeson described the solvation of an ion in solution using the Born equation [236], as corrected by Bjerrum [237], to calculate values of b_γ for various aqueous ionic solutions. The applicability of the Helgeson form of the Debye-Hückel (H-DH) equation at high ionic strengths depends on the aqueous ionic solution of interest. For aqueous NaOH and KOH solutions, the H-DH equation is accurate up to ionic strengths of 4.5 mol kg^{-1}), determined by Helgeson as the

range of validity for the extended term, b_γ, through comparison of activity coefficients reported in the literature to those computed using the H-DH equation [78]. Two other notable forms of the extended DH equation are the Davies' equation and the Truesdell-Jones equation - these are discussed in the Supporting Information and are applicable at moderate to high ionic strengths, ($I < 0.1$ mol kg^{-1}), and $I < 1$ mol kg^{-1}), respectively) [238, 239].

The Pitzer equations are suitable for high ionic strengths and mixed ion aqueous ionic solutions ($I > 1$ mol kg^{-1})) [240, 241]; however, they require specific interaction parameters between aqueous species to be defined, which are numerous in cementitious systems (Ca^{2+}, $CaOH^{+}$, $SiO(OH)^{3-}$, $SiO2(OH)_2^{2-}$, etc.). Therefore, the Pitzer equations are less pragmatic for application in cementitious systems than the extended forms of the DH equation and are not discussed further here.

6.2.2 pH measurement with a glass combination electrode

While activity cannot be directly measured, electrochemical potential can. pH is most commonly determined indirectly through measurement of an electrochemical potential using a pH meter, which typically consists of a glass combination electrode and a meter. The electrochemical potential of standard solutions with precisely known pH can be measured using a glass combination electrode, and a calibration curve of pH vs. electrochemical potential is generated by the meter. This built-in calibration curve is used to convert electrochemical potentials measured by the glass combination electrode in an analyte to pH. The electrochemical potential measured by the glass combination electrode, E_T, may be written as (Equation 6.5):

$$E_T = \epsilon + E(a_{H^+}) \tag{6.5}$$

where ϵ (mV) is an electrochemical potential due to a combination of smaller potentials that are artifacts of the design of the glass combination electrode, (see Supporting Information), and $E(a_{H^+})$ (mV) is an electrochemical potential that is a function of solution pH. While Equation 6.5 is similar to the Nernst equation ($E =$

$E_0 - 2.303\frac{RT}{F}pH$), Equation 6.5 is more appropriate in this context as the measured electrochemical potential, E_T, is not a linear function over the entire pH scale, as is implied by the Nernst equation. Despite this non-linearity, calibrations performed relating $E(a_{H^+})$ to pH are generally assumed to be linear. This is valid over most of the pH range, but not for highly acidic or alkaline solutions, where linearity between electrochemical potential and pH is lost.

Two relevant contributions to ϵ are the asymmetry potential and the liquid junction potential. An asymmetry potential is generated when identical electrolytes are found on either side of a glass electrode due to differences in the structure of each side of the glass membrane [242]. This potential is on the order of several millivolts [243]. The liquid junction potential arises due to differences in the mobilities of ions diffusing through the junction that separates the reference electrolyte from the analyte (Figure 6-1). Differences in activities between diffusing cations and anions may result in an electrochemical potential across the glass boundary; the separation of positive and negative charges produces a potential. This potential is minimized by use of a highly concentrated aqueous KCl reference electrolyte in which K^+ and Cl^- have similar mobilities [244, 245]. The liquid junction potential for most electrolytes in contact with KCl is on the order of several millivolts [246], but can rise to tens of millivolts in electrolytes of high ionic strength (I $>$ 1 M) [247].

Glass combination electrodes like those shown in Figure S1 typically use an aqueous KCl ionic solution (known as an electrolyte in this context) as the inner buffer solution (Figure 1G), which surrounds an Ag/AgCl coated measuring electrode (Figure S1D). A glass membrane sensitive to H^+ ions (Figure S1F) houses the inner buffer solution and the measuring electrode. The Ag/AgCl reference electrode (Figure S1H) is contained in a KCl reference electrolyte (Figure S1B). The reference electrolyte is separated from the analyte by a porous ceramic junction (Figure S1C) which allows slow transport of ions between the reference electrode and analyte (Figure S1J), completing the electrochemical circuit between the reference and measuring electrode. The whole probe is protected by an outer casing (Figure S1A).

The Ag/AgCl glass combination electrode with ion selective membrane is the most

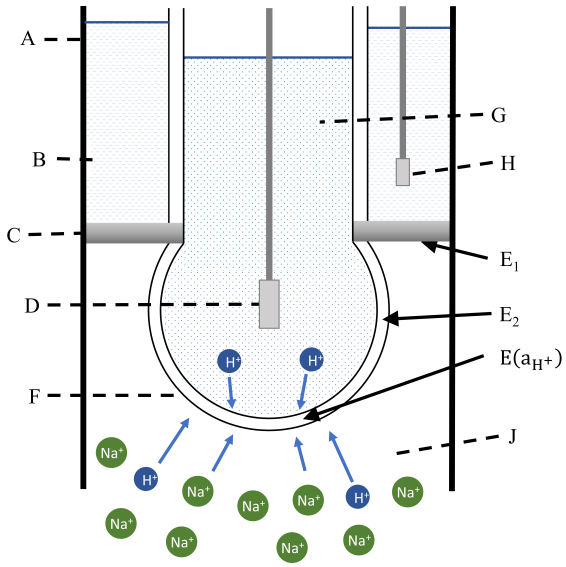

Figure 6-1: Schematic cross-section of a conventional Ag/AgCl glass combination electrode in an aqueous NaOH solution. A - External casing; B - Reference electrolyte; C - Ceramic junction; D - Measuring electrode; F - Ion selective glass membrane; H - Reference electrode; G - Inner buffer electrolyte; J - Analyte electrolyte containing H^+ and Na^+ ions; E_1 - Liquid junction potential; E_2 - Asymmetry potential; $E(a_{H^+})$ - Gel layer potential at glass membrane due to ions in analyte. The reference (B) and inner buffer (G) electrolytes are typically saturated solutions of KCl which surround the reference (H) and measuring (D) electrodes respectively, which are Ag/AgCl coated wires. The ceramic junction (C) completes the electrochemical circuit from the reference to measuring electrodes by allowing a slow, controlled flow of ions from the inner buffer electrolyte to the analyte electrolyte (J), and vice versa. The liquid junction potential (E1) arises in the ceramic junction. The ion selective glass membrane (F) is where the gel layer potential,$E(a_{H^+})$, is generated. The analyte depicted here is a high pH sodium hydroxide solution. Diffusion of alkali ions into the gel layer contributes to $E(a_{H^+})$, reducing measured pH.

common type of electrode used in pH meters. The potential of interest in this paper is the gel layer potential, $E(a_{H^+})$, which occurs at the ion selective membrane of the glass combination electrode. It arises due to the difference between H+ activity in the external analyte electrolyte and the inner buffer electrolyte. The glass membrane is a silicate glass with ion inclusions, typically Ca^{2+}, Na^+, and Li^+, but the exact glass composition depends on the analyte ions towards which the membrane is designed to be selective. The gel layer potential, which is generated across the glass membrane when in contact with the analyte, arises through formation of a charged hydrated gel layer produced on either side of the glass membrane [248, 249].

Although the gel layer potential, $E(a_{H^+})$, is designed to change only as a function of analyte H^+ ion activity (over a wide range of H+ activities and analyte chemistries), no glass membrane is ever wholly selective to one specific ion [250]. In highly alkaline solutions the hydrated gel layer has a negative structural charge and is charge-balanced significantly by aqueous alkali metal complexes (e.g., Na^+) in addition to H+, as described by Baucke [251]. Cheng described the gel layer potential as a capacitor, in which the surface charge density, caused by adsorbed ions (e.g., H^+, OH^-, Na^+), yields a potential across the glass membrane [252]. In any case, the presence of positively charged alkali ions in the gel layer artificially lowers the measured pH as alkali ions, rather than H^+ ions, contribute to the gel layer potential. This phenomenon is known as the alkali error [253, 254, 255]. It arises when measuring pH of highly alkaline aqueous solutions; the effect is relatively weak in the case of K^+, moderate for Na^+, and strong for Li^+. Standard solutions of pH 4, 7, and 10 are thus insufficient to calibrate a pH meter for measurement of highly alkaline aqueous solutions. Calibrating a pH meter with solutions of similar chemistry and ionic strength to the analyte is a means of providing a valid calibration curve by mitigating the systematic errors discussed above, including the alkali error [256].

An illustration of the alkali error is shown in Figure 6-2. Here, data for extracted CEM I Portland cement pore solutions from Vollpracht et al. is used to compare measured pH values with calculated pH values [106]. Measured pH values were reported for a given pore solution at a given time using a pH electrode. Calculated pH values were determined using the reported ion concentrations of the pore solutions as input for the H-DH equation (Equation 6.4). GEM-Selektor v3.3 (http://gems.web.psi.ch/) [9, 10] with PSI-Nagra [4] and Cemdata18 [11] databases were used to calculate ion activities. The osmotic coefficient and the Debye-Hückel extended term were used to calculate the activity of water and neutral species respectively. A discrepancy between measured and calculated pH values is notable. Calculated pH values exceed measured pH values for the majority of pore solutions.

In the context of cement science, the observed discrepancies between measured and actual pH can significantly alter interpretation of experimental results. As discussed

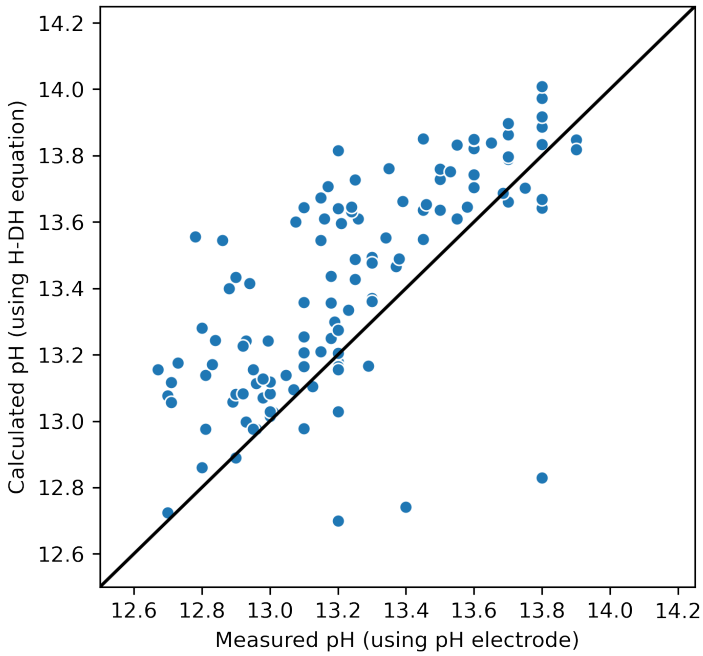

Figure 6-2: pH values of CEM I Portland cement pore solutions measured using a pH electrode compared with calculated pH values using the H-DH equation and the reported ion concentrations of the pore solutions

in the introduction, the evolution of a (solid/liquid) cementitious system depends on the OH- concentration in its aqueous phase. Dissolution rates of a wide range of minerals and cement hydration products have shown strong dependences on pH, with small differences in pH potentially corresponding to large changes in rates of dissolution [257, 87, 258, 259, 260, 261]. Similarly, the rates and distributions of reaction products vary with pH [212, 222]. For example, pH affects silicate speciation in aqueous alkali silicate solutions [262], and the relative stabilities of calcium (alkali) (alumino)silicate hydrate (C-(N-)A-S-H) and portlandite [79], and zeolites and alkali aluminosilicate (hydrate) gel [222, 263, 264, 265]. We draw attention to the fact that misinterpretation of pore solution chemistry of a cementitious system can lead to mischaracterization of its solid phases due to the intrinsic link between solid and liquid phases (e.g., equilibrium phenomena), which is relevant to systems involving pure solid phases, binders, mortar, and concrete. Aqueous solutions of NaOH and KOH are of interest in cementitious systems due to their use in AAMs and the relatively high concentrations of these alkali metals (K especially) in hydrated Portland cement.

The H-DH equation allows calculation of the activity of OH^-, and hence pH, up to ionic strengths of 4.5 mol kg^{-1} for single component aqueous systems [78] or 1-3 mol kg^{-1} in multi-component cementitious systems [79]. For solutions of known molarity, a calibration curve can be constructed through the electrochemical response of the pH meter in solution and the pH determined using the H-DH equation for each solution. By accounting for the alkali error in this way, the pH of an analyte can be accurately determined. We demonstrate the use of this methodology in the following sections of this paper.

6.3 Experimental procedures

6.3.1 NaOH and KOH standards, and LiOH solutions

NaOH and KOH standards were prepared with the following concentrations: 0.0001 M (mol L^{-1}), 0.0005 M, 0.001 M, 0.005 M, 0.01 M, 0.05 M, 0.1 M, 0.2 M, 0.5 M, 1 M, 2 M, and 3 M. NaOH and KOH standards were made by diluting commercial solutions of 3 ($\pm$0.005) M NaOH (BDH Chemicals) and 8 ($\pm$0.005) M KOH (Ricca), respectively. Dilutions were performed by transferring quantities of Na(K)OH commercial solution into volumetric flasks and filling to their marks with high purity water (18.2 MΩ cm, Millipore). The as-ordered Na(K)OH commercial solutions were stored in high-density polyethylene (HDPE) bottles. All prepared solutions were stored in clean HDPE bottles upon preparation.

LiOH solutions (concentrations of 0.0001 M (mol L^{-1}), 0.0005 M, 0.001 M, 0.005 M, 0.01 M, 0.05 M, 0.1 M, 0.2 M, 0.5 M, 1 M, 2 M, and 3 M) were prepared by addition of appropriate quantities of reagent grade lithium hydroxide monohydrate flakes ($>$ 98%, Alfa Aesar) to a 500 mL volumetric flask and filling to the mark with high purity water (18.2 MΩ cm, Millipore) once flakes had completely dissolved. Calibrations used freshly prepared solutions to mitigate effects of carbonation of alkalis. The use of analytical grade salts in the case of LiOH can lead to higher deviations ($\pm$2%) from the target concentrations than the use of standard solutions in the cases of KOH and

NaOH. This has been taken into account in the calculated uncertainties of pH values reported here, resulting in a deviation of <0.001 pH units for the LiOH solutions.

6.3.2 pH measurements

A typical pH meter offers the possibility to read out i) the pH values directly based on the built-in calibration using pH 4, 7, and 10 standard solutions ('built-in calibration') or ii) the mV electrochemical potential (mV). All pH measurements were performed with a Thermo Orion Ag/AgCl combination triode stored in KCl solution with Automatic Thermal Correction probe at 22°C. Between measurement of each analyte, the pH meter was rinsed using water purified by reverse osmosis (18 MΩ cm) (Millipore) and gently dabbed dry using delicate wipes (Kimtech). Approximately 10 mL of prepared aqueous Na(K)OH solution was transferred to a 15 mL polypropylene (PP) centrifuge tube. The solution was gently agitated for a few seconds, and the electrochemical potential was recorded after 2 minutes (when the reading had stabilized). Samples were not stirred during pH measurements [266]. The main sources of error in this study were the accuracy of the pH meter and glass combination electrode in measuring the electrochemical potential (±0.2 mV), and the error in the built-in calibration slope recorded (±0.5%). Errors in the calculated pH values are based on the standard deviation of recorded temperatures (±0.5 °C) during measurement of the pH of solutions. Error propagation calculations are included in the Supporting Information.

6.3.3 Fitted calibration curve calculations

The pH of the solution was calculated from the solution concentrations using the H-DH equation for aqueous NaOH and KOH solutions and known equilibrium constants for Na(K)OH dissociation at the measurement (laboratory) temperature (22°C) from [4]. The calculated pH values were then plotted against the measured electrochemical potentials of prepared Na(K)OH solutions using the pH meter, and the data fitted using a calibration curve ('fitted calibration'). The use of NaOH or KOH solutions

for the fitted calibration directly takes into account the alkali error, as the same alkali error occurs both during the calibration and the measurement accounting for the systematic error. Electrochemical potentials of analytes are also measured using electrochemical potential (mV) readings from the pH meter, and the fitted calibration curve is used to convert the readings to pH. A spreadsheet for the determination of this calibration curve and application to pH meter readings of sample solutions is available as Supporting Information for [218].

6.3.4 Preparation of alkali-activated biomass ash samples

Application of this methodology to a real cementitious system is also demonstrated here. Alkali-activated biomass ash experiments were prepared using 0.5 and 1 molal aqueous NaOH solutions (ACS Reagent grade water, RICCA Chemical Company; NaOH ≥97%, Sigma Aldrich) as activators at a constant liquid/solid ratio of 25 (i.e. 2 g of solid in 50 mL of solution). Solids consisted of highly siliceous biomass ash (sourced from Silverton Pulp & Papers Pvt. Ltd. In Muzzafarnagar, Uttar Pradesh, India) and $Ca(OH)_2$ (≥98%, Macron Fine Chemicals), mixed at a ratio of 1.75 g ash : 0.25 g $Ca(OH)_2$. The composition of the biomass ash, determined by X-ray fluorescence and loss on ignition tests, showed siliceous ash (61 mass% SiO_2) with high unburnt carbon (26 mass%). The phase composition (determined by X-ray diffraction) showed a primarily amorphous ash (90 mass%) with presence of quartz, albite, cristobalite, sylvite and arcanite. The materials and conditions of reaction were chosen to mimic a masonry product previously developed in [267]. Samples were mixed continuously in a tube rotator (Fisherbrand(TM) Multi-Purpose Tube Rotator, Fisher Scientific) to ages of 3 and 28 days to explore dissolution and reaction kinetics.

6.4 pH meter calibration

The linear calibration curve fittings for prepared aqueous NaOH and KOH solutions are respectively shown in Figure 6-3 (A) and (B). The alkali error associated with

measuring the pH of LiOH solutions is also demonstrated (Figure 6-3 (C)). The pH is calculated using the H-DH equation (Equation 6.4) and methodology presented here and in the Supporting Information. The measured built-in pH is based on an extrapolated calibration curve using pH 4, 7, and 10 standard solutions. The divergence at high pH (Figure 6-3A, inset) demonstrates the alkali error and the need to apply the methodology presented here when measuring highly alkaline solutions, i.e., in analysis of cementitious systems. While the calculated pH (H-DH) does trend above the measured pH, the alkali error for pH measurement in aqueous KOH solutions is not statistically significant. In contrast, the alkali error for NaOH is up to 0.5 pH units in 3 M NaOH. The alkali error for LiOH solutions is even greater - the alkali error for 2 M LiOH solutions is 1 pH unit. The extent of the alkali error in LiOH solutions precludes any meaningful direct pH measurements above concentrations of 0.5 M LiOH [268]. This trend is explained in terms of ion size: K^+ ions (internuclear radius in aqueous solution of 2.8 Å [269]) are significantly less mobile through the glass membrane than Na^+ ions (internuclear radius in aqueous solution of 2.3 Å [269]) and Li^+ ions (internuclear radius in aqueous solution of 2.1 Å [269]), due to their smaller ion size [254, 270].

The H-DH equation used above is designed for aqueous NaOH and KOH solutions [78] up to ionic strengths of 4.5 mol kg-1 [78], but in multi-component cementitious systems this range is typically taken as 1-3 mol kg^{-1} [79]. Parameters for the H-DH equation have also been calculated for other aqueous ionic solutions (HCl, LiCl, $MgCl_2$, $SrCl_2$, $CaCl_2$, $BaCl_2$, $AlCl_3$, HBr, LiBr, NaBr, $MgBr_2$, $SrBr_2$, $CaBr_2$, $BaBr_2$, HI, NaI, MgI_2, SrI_2, CaI_2, BaI_2, KF) [78]. The temperature at which the pH is recorded is important for H-DH calculations – the dissociation constants of NaOH, KOH, and H_2O change with temperature [271], affecting the OH^- concentration.

6.5 Application to cementitious systems

To demonstrate the utility of the methodology presented, pH values of filtrates taken from a series of alkali-activated biomass ash samples were measured. In each case,

Initial b_{NaOH} (mol kg^{-1})	**Biomass Ash Mass (g)**	**$Ca(OH)_2$ Mass (g)**	**Curing time (days)**	**Electro-chemical potential (mV)**	**Built-in[1] pH (-)**	**$b_{[OH-]}$ (mol kg^{-1})**	**Fitted[2] pH (-)**
0.5	0	0	3	-372.4	13.33±0.07	0.406	13.62±0.02
0.5	0	0	28	-371.3	13.31±0.07	0.385	13.60±0.02
0.5	2	0	3	-361.9	13.15±0.07	0.244	13.41±0.02
0.5	2	0	28	-352.4	12.97±0.06	0.153	13.22±0.02
0.5	1.75	0.25	3	-365.2	13.21±0.07	0.287	13.48±0.02
0.5	1.75	0.25	28	-356.4	13.04±0.07	0.186	13.30±0.02
1	0	0	3	-381.4	13.49±0.07	0.617	13.80±0.02
1	0	0	28	-380.1	13.46±0.07	0.582	13.77±0.02
1	2	0	3	-372.6	13.32±0.07	0.410	13.62±0.02
1	2	0	28	-369.4	13.26±0.07	0.352	13.56±0.02
1	1.75	0.25	3	-374.9	13.37±0.07	0.457	13.67±0.02
1	1.75	0.25	28	-372.3	13.31±0.07	0.404	13.62±0.02

Table 6.2: OH^- concentrations and pH of samples measured using calibration curve (calculated from H-DH equation, Figure 6-3A, circles) at 22 °C. [1]Obtained directly from the built-in pH meter calibration using pH 4, 7, and 10 standard solutions. The differences from the calculated pH values are due to the alkali error [2]OH^- concentration and fitted pH calculated from fitted calibration curve derived using the H-DH equation

we use the NaOH fitted calibration curve (Figure 6-3A) to convert the measured electrochemical potential to pH. Details on how these samples were made are given in the Section 6.5. The results of the pH measurements and calculations using the methodology presented here are shown in Table 6.2.

Differences between the calculated and measured pH, i.e., the alkali error, are consistently on the order of 0.3 pH units, corresponding to an underestimation of b_{OH^-} by 0.25 mol kg^{-1} if the built-in calibration is used. Samples with higher pH values differ more greatly from the actual pH, as expected. For context, at 22°C the calculated (H-DH) pH values of 1 and 0.5 mol kg^{-1} aqueous NaOH solutions are 13.86 and 13.59, respectively. The difference of 0.27 pH units is similar to the discrepancy caused by the alkali error (0.3 pH units), demonstrating the effect of this phenomenon in analysis of cementitious systems.

6.6 Chapter Summary

A methodology for calibrating pH meters in solutions of high alkali content (pH >13) has been presented. The Helgeson extension to the Debye-Hückel (H-DH) equation was used to calculate the pH of aqueous ionic solutions of known molarity. The H-DH equation was chosen because of its practicality and accuracy at high ionic strengths (approaching 4.5 mol kg^{-1}). We provide a spreadsheet for the determination of this calibration curve and application to pH meter readings of sample solutions as Supporting Information. The value of this methodology was demonstrated for a binder consisting of biomass ash, $Ca(OH)_2$ and aqueous NaOH activator. The discrepancies, caused by the alkali error, between the actual, fitted pH (calculated using the H-DH) and the measured pH (based on the built-in pH 4, 7, 10 standards calibration) were highlighted. The built-in calibration underestimated the real pH values by up to 0.3 pH units in aqueous NaOH solution, which illustrates the importance of a properly calibrated pH meter to prevent erroneous interpretations of the pH of cementitious systems. Discrepancies between built-in calibration and real, fitted pH values were more pronounced for aqueous LiOH solutions compared to aqueous NaOH solutions, but less so for aqueous KOH solutions.

6.7 Acknowledgments

We would like to acknowledge the financial support for this research through the Environmental Solutions Initiative at Massachusetts Institute of Technology (MIT), Cambridge. We also acknowledge support from NSF CAREER #1751925. Funding provided by the Scottish Research Partnership in Engineering Grant #PECRE1718/02 is gratefully acknowledged. The research leading to this publication benefitted from EPSRC funding under grant No. EP/R010161/1 and from support from the UKCRIC Coordination Node, EPSRC grant number EP/R017727/1, which funds UKCRIC's ongoing coordination.

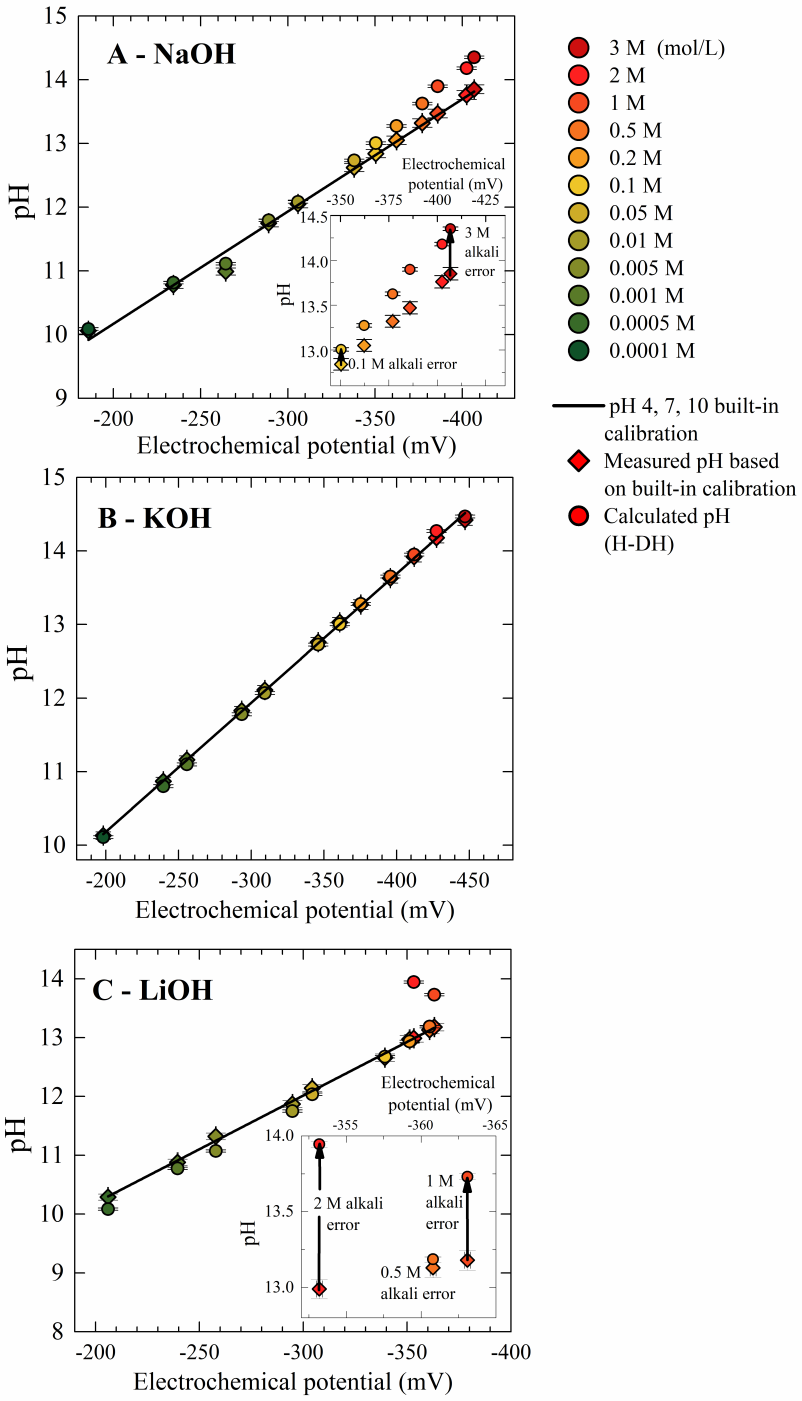

Figure 6-3: Calibration curves for aqueous NaOH (A), KOH (B), and LiOH (C) solutions of known concentration up to 3 M based upon pH values calculated using the H-DH equation (circles) and those measured by the pH meter using standard solutions of pH 4, 7, and 10 (triangles) at 22°C. For LiOH solutions, the pH was calculated using the Davies' equation, as the H-DH equation is not valid for LiOH solutions.

Chapter 7

Summary and Future Work

7.1 Summary

The stated goal of this thesis is to identify beneficial uses for steel and copper slags in building materials. Given the challenges associated with steel and copper slag use, this thesis focused on the understanding the interactions between the crystalline slag phases and the aqueous phase of the concrete - dissolution of ions from the crystalline phases into solution, and precipitation of ions out of solution onto the crystalline phases.

The first of these, dissolution, was investigated in Chapter 3 in which the effect of aqueous chemical environment on the dissolution rate of the minerals γ-C_2S and fayalite was explored. The rates of γ-C_2S dissolution were observed to decrease with higher pH, while fayalite dissolution rates increased with pH, and both relationships were described via empirical functions of the form $R = ka_{H^+}^n$. The contrasting dependence of dissolution rate on pH for both minerals was attributed to the formation of chemically distinct surface layers on both minerals during dissolution. These results have significance for blending of slags with high olivine contents in binders with a range of aqueous chemical environments.

The second of these interactions, namely precipitation of ions out of solution onto the crystalline phases, was investigated in Chapter 4. In Chapter 4, the effect of aggregate surface chemistry on the type, morphology, and rate of reaction product

formation in Portland cement-type systems was investigated. Polished surfaces of limestone, quartz, fayalite, and diopside were exposed to Ca and Si rich solutions and the resultant reaction products were characterized using SEM. The key results of this study indicate that C-S-H nucleation and growth kinetics are accelerated on limestone surfaces relative to quartz, fayalite, and diopside surfaces, although no differences in the morphology of the precipitated C-S-H is observed. Reaction product formation on the surface of an aggregate plays a crucial role in the development of hardened, load-bearing concrete. Measuring rates of reaction product formation on mineral surfaces should be the focus of future work given that there were no observed differences in morphology or reaction product type. In both cases, studies were designed to address gaps in the literature surrounding these phases.

Chapter 5 returned to the central theme of this thesis; how can we best identify beneficial uses for steel and copper slags in building materials? The 2 chapters of the thesis preceding this one serve to improve our understanding of the kinetics distinct processes. In this chapter, a simple model was built that allowed the kinetics of cement hydration and slag phase dissolution to be linked to reaction product formation. This framework, while primitive, represents a powerful strategy for identifying appropriate beneficial uses for steel and copper slags. The tasks within the chapter itself consisted of extensive reviews of the composition and microstructure of relevant slags were performed. Dissolution kinetics for the most commonly observed phases in steel and copper slags were also collected. The thermodynamics of dissolution in cementitious systems for these phases was also considered. Finally, the challenges to the incorporation of these slags into a cement hydration model are discussed.

In Chapter 6, a methodology for calibrating pH meters in highly alkaline solutions such as those relevant to cementitious systems was developed. The relevance of this work stems from the requirement for accurate aqueous phase characterization through the experimental work of this thesis. This methodology uses an extended form of the Debye-Hückel equation to generate a calibration curve of pH vs. the measured electrochemical potential (mV) based on a series of aqueous alkali hydroxide solutions of known concentrations.

7.2 Future Work

This thesis was motivated by a desire to identify uses for slags that enables the design of a concrete with lower environmental impact than existing concretes. The strategy requires the replacement of incumbent materials with waste materials with a lower embodied energy. The approach outlined in this thesis suggests a framework in which the dissolution rates of the precursor components and the nucleation and growth of reaction products be studied in isolation. As mentioned previously, this approach is a departure from much of the case-by-case studies common in the research community.

It may be worth asking; is the approach I have outlined truly more scalable than simply studying individual slag performance on a case-by-case basis? Both of these approaches are experimentally intensive and will yield, in time, suitable concrete mix designs. I believe, however, case-by-case or trial and error strategies miss the larger context and challenges of developing concretes with lower embodied energy. Alternative precursors are not and should not be limited to crystalline slags but should incorporate locally available materials. The environmental and economic costs of transporting raw materials for concrete production may be significant and the development of concretes which use local materials should be the goal of all concrete producers. If a certain precursor is not available, concrete design should be sufficiently flexible to allow the incorporation of local materials, e.g. limestone, clay, metallurgical wastes, or ashes depending on the industrial activity in the region. In each case, the properties of the precursors will vary substantially from the traditional Portland cement. Designing concretes in this way requires some predictive power over how the choice of precursors translates to concrete properties. It is only through studies of the constituent phases of all potential precursors that we can build flexible models that account for precursor variability and allow concretes to be designed efficiently.

As discussed previously, there are two main ways in which a mineral phase can influence concrete hydration; through dissolution of the phase, or by changing the type or kinetics of reaction product formation on surface of the mineral. Given the variability in the composition of these slags, and in the composition of the aqueous

phase of concrete, a more fundamental approach was adopted whereby the properties of the individual phases were investigated in a range of aqueous environments.

There are 2 aspects of precursor dissolution that merit further attention; measuring the far-from equilibrium dissolution rates of understudied mineral phases, and quantifying the changes in dissolution rate of a mineral phase as a function of the saturation state of the dissolution reaction. The former is important in identify which slag phases will be more reactive and will contribute more to the reaction product formation, and the latter is important in understanding how the dissolution rate will evolve over time during cement hydration.

Measuring far-from equilibrium dissolution rates is a reliable way to determine the reactivity of a given phase. As discussed in Section 5.3, there are several mineral phases which are commonly observed in steel and copper slags but remain unstudied. These are typically phases which are common in slags but not in the earth's crust. Gehlenite $Ca_2Al(AlSiO_7)$ and akermanite $Ca_2Mg(Si_2O_7)$ are melilite minerals which are frequently observed in steel slags but have received little research attention. Their crystal structures contain Ca, Al, and Si, elements which are more soluble than Mg or Fe in concrete pore solution, and which may contribute to the formation of C-A-S-H or related reaction products. In fact, gehlenite was calculated to be highly unsaturated in Portland cement and blended Portland cement pore solutions are all ages, suggesting a driving for and high rate of dissolution (see Section 5.3.2. RO phase is a solid solution of Mg, Fe, and Mn oxides which is also prevalent in steel and copper slag. The dissolution rate of RO phase has not been measured as a function of pH in basic solution, or as a function of composition. Given the large differences in the magnitude of the dissolution rate of MgO and FeO, the dissolution rate of RO phase as a function of Fe/Mg atomic ratio demands further enquiry. Finally, the dissolution kinetics of mayenite are also unstudied despite this phase being prevalent in incumbent cements and in steel slags. Mayenite is known to react rapidly and determining its dissolution rate would allow its hydration to be modelled in real cementitious systems.

Changes in the dissolution rate as a function of the saturation state for the disso-

lution reaction are well documented [81, 272]. Given that the activities of ions in the pore solution also change as a function of time, the dissolution rate of any given phase will likely change along with the evolving pore solution. The extent of this change is dependent on the mineral in question, and the function that describes the change in dissolution rate with respect to undersaturation is poorly understood. A better understanding of the dissolution rate dependence on saturation state is a necessary component of modeling the dissolution of slag phases in concrete pore solution over time. For example, great progress in understanding the kinetics of cement hydration have been made through a better understanding of how the dissolution rate of C_3S changes as a function of its solution saturation state. Only with a fundamental understanding of how the dissolution rates of all relevant phases change as a function of the solution saturation state can the cement or slag dissolution kinetics be properly modelled.

Beyond dissolution of the precursors, mass transport, and nucleation and growth of reaction products are the most important processes involved in cement hydration. Rates of mass transport are not dependent on the chemistry of the precursors - mass transport occurs through the aqueous phase or from the precursor surface through existing reaction product. Nucleation and growth kinetics can, however, be impacted by the presence of certain precursors [55]. In this thesis, only the effect of surface chemistry on reaction product type and morphology was investigated, although changes to the nucleation and growth rates of C-S-H on limestone surfaces were observed. Another member of the Olivetti group, Tunahan Aytas, has been designing experiments to measure the rate of nucleation and growth of C-S-H on selected mineral surfaces. Early results of these experiments confirm the accelerated growth of C-S-H on limestone relative to other surfaces.

The framework outlined in Chapter 5 relies on kinetic data for dissolution, mass transport, and nucleation and growth, as discussed above. It also requires thermodynamic data for all possible reaction products. Compared to kinetics data, thermodynamic data for these phases has been carefully tabulated over the years and has been used to accurately model the reaction products of a variety of alternative

cements [11]. Gaps remain however. The zeolite-type reaction products of alkali activated materials and the aqueous species found in high pH solutions typical of alkali activated materials are areas for which further study is required.

As a final note, the future outlook for steel and copper slag production is worth dwelling upon. As discussed in Section 5.5.2, slags with either reactive β-C_2S and C_3S phases or calcium aluminate phases are typically highly reactive and promising cement replacements. EAF and LF slags are often dominated by Ca, Si, and Al and frequently contain reactive calcium aluminates such as mayenite, brownmillerite, and C_3A. These slags also typically avoid the problematic phases present in BOF slags such as free-lime, which undergoes deleterious expansion in concrete. For this reason, EAF and LF slags are a better bet for long term usage in concrete, provided concrete mixes can be appropriately designed to make effective use of the calcium aluminate phases. In this context, the growth in steel making from EAFs in recent years is promising. Growth in the use of EAFs is down to their status as a "green" steel-making process due to the use of electricity as their electricity source. There is a limit to future EAF growth – the supply of steel scrap, which is the primary input. There also exist large differences in the regional production of BOF and EAF slags. For example, in 2019, 90 % of crude steel production in China uses BOFs, whereas 70 % of crude steel production in the US is from EAFs [27]. Developing countries undergoing rapid urbanization tend to rely on BOFs before transitioning to EAFs as the scrap supply increases and reliance on coal diminishes. This regional availability and growth of EAF slags is an important consideration in the development of blended concretes.

Appendix A

Appendix: Supplementary Information for Chapter 5

The following tables represent the full literature review of the crystalline phase content of copper slags, BOF slags, EAF slags, and LF slags in which each row represents a slag reported in the literature.

	Furnace type	**Olivine**	**Pyroxene**	**Glass**	**Other silicates**	**Spinel**	**Sulfur compounds**	**Cu**
[145]	Blast furnace	Fay (M), Mon (M)		Si-Ca-Fe-Al (M)	Mel (M)	Spin (m)	Pyr (m), Sph (m)	
[145]	Reverbatory	Fay (m)		Si-Ca-Fe-Al (M)	Mel (m)	Spin (M)	CFS (m)	(m)
[273]	Blast furnace	Fay (M)		(M)		Spin (M)		(m)
[273]	Pierce-Smith	Fay (M)		(M)		Spin (M)		(m)
[273]	Reverbatory and Pierce-Smith			(M)	Q (m)			(m)
[150]	Reverbatory and Pierce-Smith	Fay (m), Kir (M)	Aug-Hed (M)	(M)	Q (m), Leuc (M)	Mag (M), Spin A (m)	CFS (m)	(m)

[150]	Reverbatory/ Electric arc and Pierce-Smith	Fay (M)	Aug-Hed (M)	(M)	Q (m)	Mag (M)	CFS (m)	(m)
[150]	Electric arc furnace			(M)			CFS (m)	
[274]	Granulated	Fay (M)		(M)		Mag (M)		
[149]	El Teniente process, air-cooled	Fay (52)		(35)		Mag (13)	CFS (m)	
[51]	Shaft furnace	Fay	Ess, Aug-Hed					
[51]	Granulated from electric furnace			(M)				
[151]	Shaft furnace		Diop (M)					
[151]	Granulated from electric furnace			(M)				
[147]	Ausmelt furnace slag	Fay (M)	CP (M)	(M)		Spin B (M)		
[147]	Reverbatory			(M)		Spin B (m)		
[147]	Unknown	Fay (M)	CP (M)	(M)		Spin B (M)		
[275]	Flash smelting	Fay (48.8)		(23.7)		Mag (22.4)	Sph (0.23), CFS (0.35)	0.07
[276]	Flash smelting	Fay (M)				Mag (M)		
[146]	Flash smelting	Fay (M)		(M)		Mag (M)		
[146]	Unknown	Fay (M)		(M)		Mag (M)		
[277]	Unknown	Fay (M)				Mag (M)		
[278]	Unknown	Fay (M)				Mag (M), Spin C (m)		
[279]	Unknown	Fay (15)			Q (20)	Mag (40)	Pyr (15), Jar (15)	

[280]	Unknown	Fay (M)	Fer (m)		Q (m)	Spin D (m)		
[281]	Unknown	Fay (60)		(19)		Mag (4), Spin (4)	Sph (0.5), CFS (1)	
[282]	Unknown	Fay			Q		Jar (Present)	
[283]	Unknown	Fay (73)	Aug-Hed (20)	(20)	Leuc (8)	Mag (4)	Pyr (3)	
[148]	Unknown	Fay		Present		Mag		
		23/28	8/28	21/28		22/28		

Table A.1: Reported mineralogy of copper slags. (m) = minor quantity, (M) = Major quantity, Fay = Fayalite, Mon = Monticellite, Kir = Kirschteinite, Aug-Hed = Augite-hedenbergite solid solution, Ess = Esseneite, Diop = Diopside, Fer = Ferrosilite, CP = Clinopyroxene ($CaFeSi_2O_6$), Mel = Mellilite, Q = Quartz, Leuc = Leucite, Spin = Spinel (unspecified composition), Mag = Magnetite, Spin A = Spinel with composition $Fe(Cr,Al,Fe)_2O_4$, Spin B = Spinel with composition $(Fe^{2+},Mg,Zn)(Fe^{3+},Al,Cr)_2O_4$, Spin C = Spinel with composition $Cu_{0.5}Mn_{0.5}Fe_2O_4$, Spin D = Spinel with composition $FeAl_2O_4$, Pyr = Pyrite, Sph = Sphalerite, CFS = Copper-iron-sulfides, Jar = Jarosite

	Origin	**β-C_2S**	**Di-calcium ferrite**	**Fe^{+2} oxides**	**Ca, Mg oxides**	**Other iron oxides**	**Olivines**	**Pyroxenes**	**Other silicates**	**Other oxides**	**Weathering products**
[161]	France, 2006	(P)	(P)	RO (P)	Lim (P)						Port (P), Cal(P)
[284]	France, 2007	(P)	(P)	RO (P)							Port (P), Cal(P)
[285]	Sweden, 2009	(P)	(P)	wües (P)	Lim (P)						
[157]	Sweden, 2007	(P)	(P)	RO (P)	Lim (P)				C_3S (P)		
[286]	China, 2013	(m)	(9)			Mag (m)			Glass (64), Geh (m), Q (m)		

[131]	Britain, 1987	(25.6)	(14.6)	RO (24)	Lim (8), Per (2.4)				C_3S (11.8)		Port (0.6)
[131]	Britain, 1987	(47)	(15.8)	RO (22.8)	Lim (4.2), Per (0.8)				C_3S (0.6)		Port (0.8)
[131]	Britain, 1987	(31.2)	(14.2)	RO (22)	Lim (10.2), Per (0.4)				C_3S (1.8)		Port (0.4)
[131]	Britain, 1987	(16.2)	(11.8)	RO (18.6)	Lim (13.4), Per (1)				C_3S (2.6)		
[131]	Britain, 1987	(28.6)	(17.4)	RO (14.4)	Lim (15.8), Per (1)						
[141]	Romania, 2007			wües (10.2)	Lim (22.5)	Mag (39), Hem (39)			Geh (28.3)		
[154]	India, 2006	(P)	(P)		Lim (P)						
[155]		(M)	(M)	RO (M)	Lim (m)	Mag (m)			C_3S (m)		
[287]	France, 2009	(P)	(P)	RO (P)	Lim (P)	Mag (P)			C_3S (P)	C4AF (P)	Port (P), Cal(P)
[288]	US, 2015	(P)	(P)	wües (P)	Lim (P)	Mag (P)			C_3S (P)	May (P)	Cal(P)
[289]	China, 2014	(P)		wües (P)			Ca (P)	Woll (P)	C_3S (P)		Cal(P)
[160]	Netherlands, 2020	(P)	(P)	wües (P)	Lim (P)	Mag (P)			Glass (P)		Port (P), Cal(P)
[158]	Britain, 2013	(P)	(P)	wües (P)	Lim (P)						
[290]	Brazil, 2018	(P)	(P)			Mag (P)			Glass (P)		

[291]	China, 2014	(P)	(P)	RO (P)	Lim (P)				C_3S (P)		Port (P), Cal(P)
[292]	Taiwan, 2018	(P)	(P)	wües (P)	Lim (P)	Mag (P)		Woll (P)	Q (P)		Port (P), Bruc (P), Cal(P)
[293]	Romania, 2013	(17.5)	(26.7)	wües (11.3)		Mag (6.4)	Ca (3), Fay (4.7)	Woll(4.6), Ferr(6.1), Enst(6.5)	Glass (4)		Port (3.8), Bruc (2.1)
[293]	Belgium, 2013	(30.8)	(32.3)	wües (6.7)	Lim (8.8), Per (1.1)		Ca (0.8), Fay (3.8)	Woll(2.9), Ferr(2.2), Enst(1.9)			Port (3.1), Bruc (2.4)
[156]	France, 2010	(P)	(P)	wües (P)	Lim (P)						
[294]	China, 2006	(P)		RO (P)					C_3S (P)		
[135]	Mexico, 2018										Port (29.9), Bruc (38.1)
[295]	Netherlands, 2020	(19.9)		wües (3), Mg-W (22.1)		Mag (3.9)			Glass (38.8)	C4AF (12.3)	
[159]	France, 2011	(P)	(P)	wües (P)	Lim (P), Per (P)	Mag (P)			Q (P)		Port (P), Cal(P)
[296]	China, 2013	(P)	(P)	RO (P)					C_3S (P)		
[297]	China, 2015	(P)	(P)	RO (P)		Hem (P)			C_3S (P)		Port (P), Cal(P)
[298]	Spain, 2010	(P)	(P)		Lim (P)	Mag (P), Hem (P)			Q (P)		Port (P), Cal(P)

[133]	Belgium, 2012	(21.5)	(37.2)	wües (1.1)	Lim (10.6), Per (0.7)	Mag (0.8), Hem (4.1)	Ca (7.3), Fay (5.5)	Woll(1.1), Ferr(2.8), Enst(3.8)			
[133]	Belgium, 2012	(22)	(31)	wües (2.2)	Lime (20.6), Per (1.6)	Mag (0.4), Hem (2)	Ca (7.9), Fay (4.2)	Woll(0.7), Ferr(3.6), Enst(1.9)			
[299]	Italy, 2014	(P)	(P)			Mag (P)				Cor (P)	Port (P), Bruc (P), Cal(P)
[132]	Taiwan, 2016	(40)	(30)	Mg-W (20)	Lim (10)						Cal(P)
[300]	Italy, 2016	(P)	(P)	wües (P)							
[301]	Taiwan, 2017	(P)		wües (P), Mg-W (P)							Port (P)
[302]	China, 2016	(P)		wües (P)				Woll (P)	C_3S (P)		Cal(P)
[130]	Britain, 2014	(29)	(12)	RO (32)	Per (8)					Cor (7)	
[138]	China, 2011	(P)	(P)	RO (P)	Lim (P)	Mag (P)			C_3S (P)		Port (P)
[163]	China, 2017	(P)	(P)	RO (P)	Lim (P), Per (P)	Mag (P)	Fay (P)		C_3S (P)	May (P)	Cal(P)
[303]	Taiwan, 2013		(P)		Lim (P)						Cal(P)
[152]		(51.4)	(20.7)	(13.1)	Lim (13.2), Per (1.7)						
		40/43	36/43	36/43	29/43	18/43	6/43	7/43			24/43

Table A.2: Reported mineralogy of BOF slags. RO = RO Phase, wües = wüestite, Mg-W = Mg-wüestite, Lim = Lime, Per = Periclase, Mag = Magnetite, Hem = Hematite, Ca = γ-C_2S, Fay = Fayalite, Woll = Wollastonite, Ferr = Ferrosilite, Enst = Enstatite, C_3S = tricalcium silicate, Geh = Gehlenite ($Ca_2Al(AlSiO_7)$), Q = Quartz, Port = Portlandite, Cal = Calcite, Bruc = Brucite

	Origin	**β-C_2S**	**Fe^{+2} oxides**	**Spinels**	**Olivines**	**Other silicates**	**Other Fe oxides**	**Other oxides**
[285]	Sweden, 2009	(P)	Wüs (P)	$CaFe_2O_4$ (P)				
[166]	Slovenia, 2011	(P)	Wüs (P)	Chr (P)		Geh (P)	Bro (P)	
[170]	India, 2009	(P)					Bro (P)	
[157]	Sweden, 2007			(Mg,Mn) $(Cr,Al,Fe)_2$ O_4 (P)	Cal (P)	Mer (P)		
[157]	Sweden, 2007	(P)	RO (P)				Bro (P), Hem (P)	
[304]	Spain, 2000	(P)		$MgFe_2O_4$ (P), Mag (P)		Geh (P), Bred (P)		Mn (P)
[141]	Romania, 2007	(P)						Mn (P)
[173]	China, 2002	(P)	RO (P)			Mer (P)		
[173]	China, 2002		RO (P)		Kir (P)	Mer (P)		
[173]	China, 2002		RO (P)		Kir (P)			
[137]	US, 2018	(P)	Wüs (P)	Mag (P)		Bred (P)		May (P)
[305]	Spain, 2016		Wüs (P)		Kir (P)	Geh (P)		Mn (P)
[136]	Malaysia, 2016	(21)	Wüs (20.3)			Geh (45.3)		
[169]	France, 1960-2010	(P)	Wüs (P)	(Fe,Mg) $(Fe,Mn,Cr)_2O_2$ (P), $Fe(Cr,Al)O_4$ (P)		Q (P)	Bro (P)	

[135]	Mexico, 2018		Wüs (54.9)			Geh (4.7), Mer (9.2)		
[171]	France, 2016					Ake (P), Mer (P), Cusp (P)		
[164]	Italy, 2016	(P)	Wüs (P)				Bro (P), Hem (P)	
[306]	India, 2010		Wüs (M)			Geh (M), Bred (m)		
[134]	UAE, 2012	(36)	Wüs (51)			Bred (8)		
[307]	Malaysia, 2019	(P)		Mag (P)		Q (P)	Hem (P)	
[308]	Italy, 2013	(P)	Wüs (P)				Bro (P), Hem (P)	May (P), Per (P)
[309]	Italy, 2013			Mag (P)	Cal (P)	Geh (P), Ake (P), Q (P), Cusp (P)		May (P), Per (P)
[138]	China, 2011				Cal (P)	Geh (P), Mer (P)		Per (P)
[139]	Italy, 2010	(P)	Wüs (P)	Mag (P)		Geh (P)		May (P)
		15/24	16/24	9/24	6/24			

Table A.3: Reported mineralogy of EAF slags. Wüs = Wüstite, RO = RO Phase, Chr = Chromite, Mag = Magnetite, Ca = calcio-olivine, Kir = Kirschteinite, Geh = Gehlenite ($Ca_2Al(AlSiO_7)$), Mer = Merwinite, Bred = Bredigite, Q = Quartz, Ake = Akermanite, Cusp = Cuspidine, Bro = Brownmillerite, Hem = Hematite, Mn = Mn oxide, May = Mayenite, Per = Periclase

	Origin	**β-C_2S**	**γ-C_2S**	**Periclase**	**Mayenite**	**C_3A**	**Pyroxene**	**Amorphous**	**Other silicates**	**Salts**	**Spinel**	**Iron oxides**	**Weathering products**
[157]	Sweden, 2007	(P)	(P)	(P)	(P)				Geh (P)				
[141]	Romania, 2007						Woll (38)			CaS (11.3)			

[28]	Spain, 2009	(P)	(P)	(P)	(P)	(P)	Woll (P), Diop (P)		Bre (P), Jas (P)	Flu (P)	$MgAl_2O_4$ (P)	(P)	Port (P)
[28]	Spain, 2009	(P)	(P)	(P)	(P)	(P)	Diop (P)		Mer (P), Jas (P)	Flu (P)		(P)	Port (P)
[28]	Spain, 2009			(P)	(P)	(P)	Diop (P)		Jas (P)	Flu (P)		(P)	Port (P)
[125]	Finland, 2019		(P)	(P)	(P)	(P)							
[29]	Canada, 2002	(m)	(M)						Mer (m), C_3S (m)	Flu (m)			Port (m), Dol (m)
[30]	Sweden, 2011	(5.9)			(11.6)	(8.9)			Q (20.6)			Wüs (6.6)	Dol (3.5)
[310]	Italy, 2013	(m)	(M)		(M)			(M)	Geh (M), Glass (M)	CaS (m)			Port (m), Dol (m)
[126]	Finland, 2019		(21)	(2.1)	(21.9)	(2.3)		4	Glass (4), Q (47.3)				
[137]	US, 2018	(P)			(P)							Wüs (P)	
[285]	Sweden, 2009		(P)	(P)	(P)				Geh (P)				
[305]	Spain, 2016		(P)	(P)									
[311]	Belgium, 2012	(1)	(34)	(15)			Woll (2)	20	Mer (6), Bre (7), Cusp (10), Glass (20)	Flu (2)	$MgCr_2O_4$ (3)		

[140]	Belgium, 2015		(51)	(10)				8	Mer (3), Bre (10), Cusp (15), Glass (8)	Flu (3)			
[312]	Croatia, 2013	(P)	(P)	(P)	(P)	(P)			Geh (P)				
[313]	Czechia, 2013	(P)	(P)	(P)	(P)				C_3S (P)	Flu (P)		Wüs (P)	
[314]	Spain, 2005	(P)	(P)	(5)			Diop (10)	10	Bre (P), C_3S (P), Glass (10)		Al_2MgO_4 (20)		Port (20)
		11/18	14/18	13/18	12/18	7/18	6/18	6/18					

Table A.4: Reported mineralogy of LF slags. Woll = Wollastonite, Diop = Diopside, Geh = Gehlenite ($Ca_2Al(AlSiO_7)$), Bre = Bredigite, Jas = Jasmundite, Mer = Merwinite, C_3S = tricalcium silicate, Q = Quartz, Cusp = Cuspidine, Wüs = Wüstite, Port = Portlandite, Dol = Dolomite

Table A.5 contains the composition of Portland cement used for calculating the extent of consumption from Parrot's model in Section 5.4.

Tables A.6, A.7, and A.8 tabulate the input quantities for the thermodynamic simulations of the 3 mixes of interest (PC, PC+EAF, and PC+EAF+Gyp), as described in Section 5.4.1.

	wt %	**Molar mass (g/mol)**	**Molar vol (cm3/mol)**	**mol/100g cement**
C_3S	65.4	348.5	73.180	0.188
C_2S	10.2	172.2	51.790	0.0592
C_3A	7.5	270.2	89.217	0.0278
C_4AF	8.5	486	130.202	0.0175
MgO	0.9	40.3	NaN	0.0223
CaO	0.93	56.1	NaN	0.0166
$CaCO_3$	0.6	100.1	36.934	0.006
Gypsum	3.1	172.2	74.690	0.018
K_2SO_4	1.3	174.3	65.500	0.00746
Na_2SO_4	0.21	142	53.330	0.00148
Na_2O(C)	0.33	62	NaN	0.00532
K_2O(C)	0.054	94.2	NaN	0.00057
MgO(C)	0.94	40.3	NaN	0.02333
SO_3(C)	0.11	80.1	NaN	0.00137

Table A.5: Portland cement composition for Parrot's hydration model. Composition taken from [8]. Phases with (C) are considered to be part of the C_3S.

Age (days)	C_2S	C_3A	C_3S	C_4AF	$CaCO_3$	CaO	Gypsum	K_2O	K_2SO_4	MgO	Na_2O	Na_2SO_4	SO_3
0.01	0.1	0.3	2.1	0.1	0.1	16.6	18.0	0.01	7.5	22.5	0.05	1.5	0.01
0.03	0.4	0.6	4.1	0.1	0.1	16.6	18.0	0.01	7.5	22.8	0.1	1.5	0.03
0.06	0.7	1.1	7.9	0.2	0.2	16.6	18.0	0.02	7.5	23.2	0.2	1.5	0.05
0.1	1.1	1.9	13.9	0.3	0.4	16.6	18.0	0.04	7.5	23.8	0.3	1.5	0.1
0.3	3.3	6.0	45.9	0.8	1.2	16.6	18.0	0.1	7.5	27.1	1.1	1.5	0.3
0.6	6.0	9.6	70.4	1.8	1.9	16.6	18.0	0.2	7.5	29.7	1.7	1.5	0.4
1	8.7	12.2	87.9	3.5	2.4	16.6	18.0	0.2	7.5	31.8	2.2	1.5	0.6
2	14.1	16.5	113.6	6.6	3.2	16.6	18.0	0.3	7.5	35.0	2.9	1.5	0.7
3	17.1	18.0	123.2	7.8	3.6	16.6	18.0	0.3	7.5	36.2	3.2	1.5	0.8
4	19.3	19.0	129.3	8.6	3.8	16.6	18.0	0.4	7.5	37.0	3.4	1.5	0.9
5	20.9	19.7	133.6	9.2	3.9	16.6	18.0	0.4	7.5	37.6	3.5	1.5	0.9
6	22.3	20.2	137.0	9.6	4.0	16.6	18.0	0.4	7.5	38.1	3.6	1.5	0.9
8	24.5	21.1	142.5	10.3	4.2	16.6	18.0	0.4	7.5	38.8	3.8	1.5	1.0
9	25.3	21.4	144.4	10.6	4.3	16.6	18.0	0.4	7.5	39.0	3.8	1.5	1.0
10	26.1	21.6	146.0	10.8	4.4	16.6	18.0	0.4	7.5	39.3	3.9	1.5	1.0
20	32.6	23.8	160.4	12.8	4.9	16.6	18.0	0.5	7.5	41.2	4.3	1.5	1.1
30	34.8	24.1	163.9	13.3	5.0	16.6	18.0	0.5	7.5	41.7	4.4	1.5	1.1
50	37.6	24.4	168.4	13.7	5.1	16.6	18.0	0.5	7.5	42.3	4.6	1.5	1.2
60	38.4	24.5	169.5	13.8	5.2	16.6	18.0	0.5	7.5	42.5	4.6	1.5	1.2
80	39.7	24.6	171.3	14.0	5.2	16.6	18.0	0.5	7.5	42.7	4.6	1.5	1.2
100	40.6	24.8	172.4	14.1	5.3	16.6	18.0	0.5	7.5	42.9	4.7	1.5	1.2
300	46.9	25.8	180.5	15.0	5.6	16.6	18.0	0.5	7.5	44.0	5.0	1.5	1.3
600	47.1	26.0	181.0	15.2	5.6	16.6	18.0	0.5	7.5	44.1	5.0	1.5	1.3
1000	47.3	26.1	181.5	15.3	5.6	16.6	18.0	0.5	7.5	44.2	5.0	1.5	1.3

Table A.6: Input quantities (units of milli-moles) for calculating reaction product assemblage for OPC hydration using the model of Parrot [3]. GEM-Selektor v3.3 (http:// gems.web.psi.ch/) [9, 10] with PSI-Nagra [4] and Cemdata18 [11] databases was used to calculate reaction product assemblage at each time point. Reaction product assemblage is shown in Figure 5-9.

Age (days)	Al_2O_3	C_2S	C_3A	C_3S	C_4AF	$CaCO_3$	CaO	Fe_2O_3	FeO	Gypsum	K_2O	K_2SO_4	MgO	Na_2O	Na_2SO4	SO_3	SiO_2
0.01	4.6	0.1	0.3	2.1	0.1	0.1	24.6	4E-10	7E-08	18.0	0.01	7.5	22.7	0.05	1.5	0.01	0.1
0.03	12.1	0.4	0.6	4.1	0.1	0.1	37.7	1E-09	2E-07	18.0	0.01	7.5	23.2	0.1	1.5	0.03	0.2
0.06	18.7	0.7	1.1	7.9	0.2	0.2	49.6	2E-09	4E-07	18.0	0.02	7.5	23.9	0.2	1.5	0.05	0.4
0.1	23.0	1.1	1.9	13.9	0.3	0.4	57.4	4E-09	7E-07	18.0	0.04	7.5	25.0	0.3	1.5	0.1	0.7
0.3	25.2	3.3	6.0	45.9	0.8	1.2	64.2	1E-08	2E-06	18.0	0.1	7.5	30.8	1.1	1.5	0.3	2.2
0.6	25.2	6.0	9.6	70.4	1.8	1.9	68.2	2E-08	4E-06	18.0	0.2	7.5	36.6	1.7	1.5	0.4	4.2
1	25.2	8.7	12.2	87.9	3.5	2.4	72.8	3E-08	7E-06	18.0	0.2	7.5	42.2	2.2	1.5	0.6	6.5
2	25.2	14.1	16.5	113.6	6.6	3.2	85.2	7E-08	1E-05	18.0	0.3	7.5	53.5	2.9	1.5	0.7	12.7
3	25.2	17.1	18.0	123.2	7.8	3.6	94.2	1E-07	2E-05	18.0	0.3	7.5	59.6	3.2	1.5	0.8	17.2
4	25.2	19.3	19.0	129.3	8.6	3.8	102.1	1E-07	3E-05	18.0	0.4	7.5	63.7	3.4	1.5	0.9	21.1
5	25.2	20.9	19.7	133.6	9.2	3.9	107.7	2E-07	3E-05	18.0	0.4	7.5	66.1	3.5	1.5	0.9	23.9
6	25.2	22.3	20.2	137.0	9.6	4.0	113.3	2E-07	4E-05	18.0	0.4	7.5	67.9	3.6	1.5	0.9	26.7
8	25.2	24.5	21.1	142.5	10.3	4.2	121.3	3E-07	6E-05	18.0	0.4	7.5	69.6	3.8	1.5	1.0	30.7
9	25.2	25.3	21.4	144.4	10.6	4.3	123.6	3E-07	6E-05	18.0	0.4	7.5	70.0	3.8	1.5	1.0	31.9
10	25.2	26.1	21.6	146.0	10.8	4.4	127.6	4E-07	7E-05	18.0	0.4	7.5	70.3	3.9	1.5	1.0	33.9
20	25.2	32.6	23.8	160.4	12.8	4.9	132.6	7E-07	1E-04	18.0	0.5	7.5	72.2	4.3	1.5	1.1	36.4
30	25.2	34.8	24.1	163.9	13.3	5.0	132.7	1E-06	2E-04	18.0	0.5	7.5	72.7	4.4	1.5	1.1	36.4
50	25.2	37.6	24.4	168.4	13.7	5.1	132.9	2E-06	3E-04	18.0	0.5	7.5	73.3	4.6	1.5	1.2	36.5
60	25.2	38.4	24.5	169.5	13.8	5.2	133.0	2E-06	4E-04	18.0	0.5	7.5	73.5	4.6	1.5	1.2	36.6
80	25.2	39.7	24.6	171.3	14.0	5.2	133.2	3E-06	6E-04	18.0	0.5	7.5	73.7	4.6	1.5	1.2	36.7
100	25.2	40.6	24.8	172.4	14.1	5.3	133.5	4E-06	7E-04	18.0	0.5	7.5	73.9	4.7	1.5	1.2	36.8
300	25.2	46.9	25.8	180.5	15.0	5.6	135.2	1E-05	2E-03	18.0	0.5	7.5	75.1	5.0	1.5	1.3	37.7
600	25.2	47.1	26.0	181.0	15.2	5.6	137.8	2E-05	4E-03	18.0	0.5	7.5	75.1	5.0	1.5	1.3	39.0
1000	25.2	47.3	26.1	181.5	15.3	5.6	140.2	4E-05	7E-03	18.0	0.5	7.5	75.2	5.0	1.5	1.3	40.2

Table A.7: Input quantities (units of milli-moles) for calculating reaction product assemblage for OPC hydration and EAF slag dissolution. GEM-Selektor v3.3 (http:// gems.web.psi.ch/) [9, 10] with PSI-Nagra [4] and Cemdata18 [11] databases was used to calculate reaction product assemblage at each time point. Reaction product assemblage is shown in Figure 5-9.

Age (days)	Al_2O_3	C_2S	C_3A	C_3S	C_4AF	$CaCO_3$	CaO	Fe_2O_3	FeO	Gypsum	K_2O	K_2SO_4	MgO	Na_2O	Na_2SO4	SO_3	SiO_2
0.01	4.6	0.1	0.3	2.1	0.1	0.1	24.6	4E-10	7E-08	33.0	0.01	7.5	22.7	0.05	1.5	0.01	0.1
0.03	12.1	0.4	0.6	4.1	0.1	0.1	37.7	1E-09	2E-07	33.0	0.01	7.5	23.2	0.1	1.5	0.03	0.2
0.06	18.7	0.7	1.1	7.9	0.2	0.2	49.6	2E-09	4E-07	33.0	0.02	7.5	23.9	0.2	1.5	0.05	0.4
0.1	23.0	1.1	1.9	13.9	0.3	0.4	57.4	4E-09	7E-07	33.0	0.04	7.5	25.0	0.3	1.5	0.1	0.7
0.3	25.2	3.3	6.0	45.9	0.8	1.2	64.2	1E-08	2E-06	33.0	0.1	7.5	30.8	1.1	1.5	0.3	2.2
0.6	25.2	6.0	9.6	70.4	1.8	1.9	68.2	2E-08	4E-06	33.0	0.2	7.5	36.6	1.7	1.5	0.4	4.2
1	25.2	8.7	12.2	87.9	3.5	2.4	72.8	3E-08	7E-06	33.0	0.2	7.5	42.2	2.2	1.5	0.6	6.5
2	25.2	14.1	16.5	113.6	6.6	3.2	85.2	7E-08	1E-05	33.0	0.3	7.5	53.5	2.9	1.5	0.7	12.7
3	25.2	17.1	18.0	123.2	7.8	3.6	94.2	1E-07	2E-05	33.0	0.3	7.5	59.6	3.2	1.5	0.8	17.2
4	25.2	19.3	19.0	129.3	8.6	3.8	102.1	1E-07	3E-05	33.0	0.4	7.5	63.7	3.4	1.5	0.9	21.1
5	25.2	20.9	19.7	133.6	9.2	3.9	107.7	2E-07	3E-05	33.0	0.4	7.5	66.1	3.5	1.5	0.9	23.9
6	25.2	22.3	20.2	137.0	9.6	4.0	113.3	2E-07	4E-05	33.0	0.4	7.5	67.9	3.6	1.5	0.9	26.7
8	25.2	24.5	21.1	142.5	10.3	4.2	121.3	3E-07	6E-05	33.0	0.4	7.5	69.6	3.8	1.5	1.0	30.7
9	25.2	25.3	21.4	144.4	10.6	4.3	123.6	3E-07	6E-05	33.0	0.4	7.5	70.0	3.8	1.5	1.0	31.9
10	25.2	26.1	21.6	146.0	10.8	4.4	127.6	4E-07	7E-05	33.0	0.4	7.5	70.3	3.9	1.5	1.0	33.9
20	25.2	32.6	23.8	160.4	12.8	4.9	132.6	7E-07	1E-04	33.0	0.5	7.5	72.2	4.3	1.5	1.1	36.4
30	25.2	34.8	24.1	163.9	13.3	5.0	132.7	1E-06	2E-04	33.0	0.5	7.5	72.7	4.4	1.5	1.1	36.4
50	25.2	37.6	24.4	168.4	13.7	5.1	132.9	2E-06	3E-04	33.0	0.5	7.5	73.3	4.6	1.5	1.2	36.5
60	25.2	38.4	24.5	169.5	13.8	5.2	133.0	2E-06	4E-04	33.0	0.5	7.5	73.5	4.6	1.5	1.2	36.6
80	25.2	39.7	24.6	171.3	14.0	5.2	133.2	3E-06	6E-04	33.0	0.5	7.5	73.7	4.6	1.5	1.2	36.7
100	25.2	40.6	24.8	172.4	14.1	5.3	133.5	4E-06	7E-04	33.0	0.5	7.5	73.9	4.7	1.5	1.2	36.8
300	25.2	46.9	25.8	180.5	15.0	5.6	135.2	1E-05	2E-03	33.0	0.5	7.5	75.1	5.0	1.5	1.3	37.7
600	25.2	47.1	26.0	181.0	15.2	5.6	137.8	2E-05	4E-03	33.0	0.5	7.5	75.1	5.0	1.5	1.3	39.0
1000	25.2	47.3	26.1	181.5	15.3	5.6	140.2	4E-05	7E-03	33.0	0.5	7.5	75.2	5.0	1.5	1.3	40.2

Table A.8: Input quantities (units of milli-moles) for calculating reaction product assemblage for OPC hydration and EAF slag dissolution, with additional gypsum. GEM-Selektor v3.3 (http:// gems.web.psi.ch/) [9, 10] with PSI-Nagra [4] and Cemdata18 [11] databases was used to calculate reaction product assemblage at each time point. Reaction product assemblage is shown in Figure 5-9.

Thermodynamic driving force for dissolution in CEM I blended cements

The saturation state of portlandite, γ-C_2S, C_3S, β-C_2S. and gehlenite are calculated in FA blended Portland cement binders, shown in Figure A-1. Each datapoint represents an individual pore solution. The same trends as before are held - portlandite and γ-C_2S are supersaturated in most pore solutions, while C_3S and β-C_2S are undersaturated in most pore solutions. In this case, the values of ΔG_{diss} for γ-C_2S and β-C_2S pore solutions are merely shifted along the y-axis due to the fact that all pore solutions are at the same temperature (25°C) and the only difference between the two systems is the standard Gibbs free energy of the dissolving mineral.

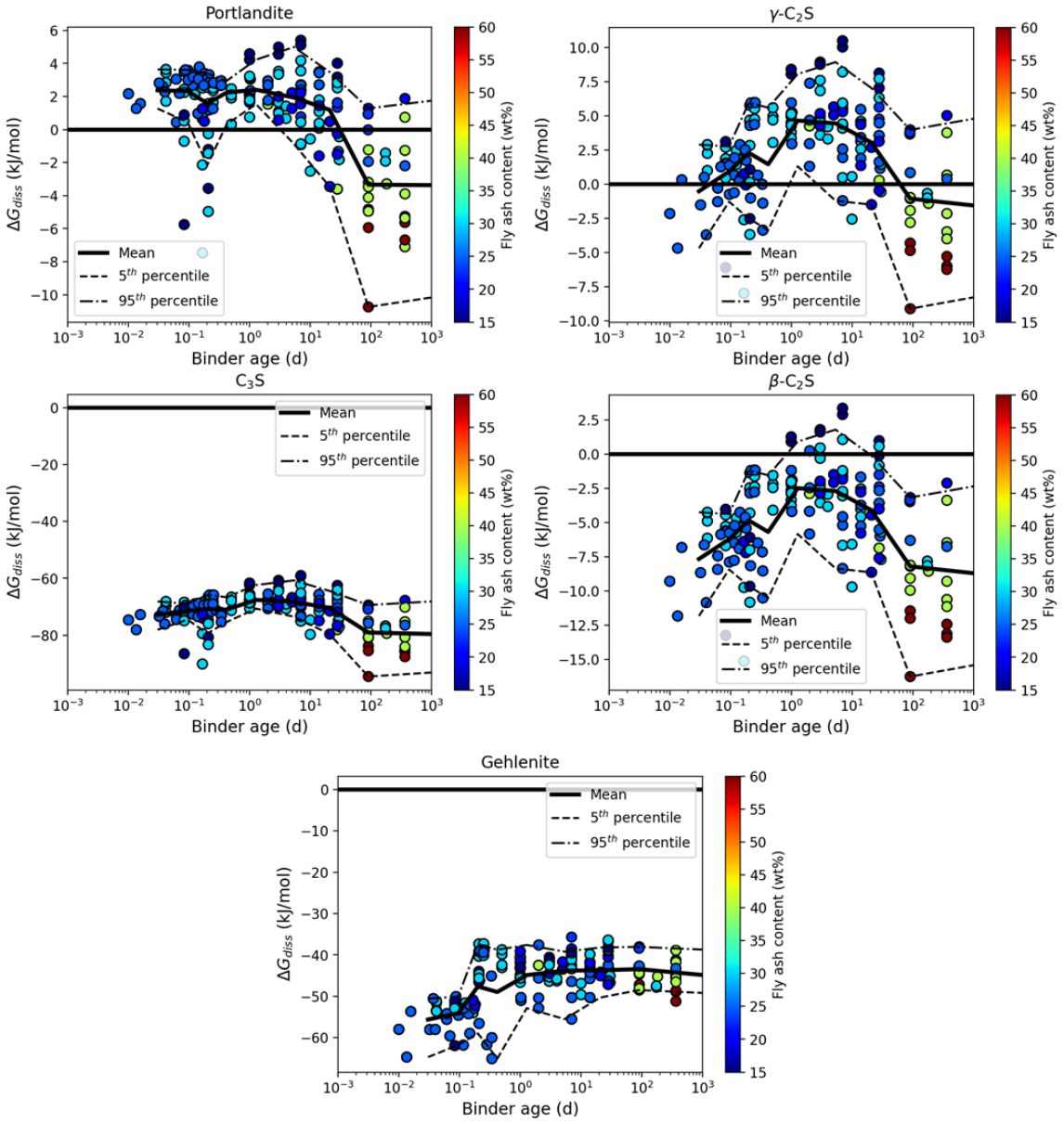

Figure A-1: Driving force for mineral dissolution reactions in FA blended Portland cement binders. All pore solutions are at 25°C. Each datapoint represents the saturation state of that mineral in a given FA blended Portland cement binder pore solution for which the concentration of the relevant ions have been experimentally measured.

Bibliography

[1] Steven J. Davis, Nathan S. Lewis, Matthew Shaner, Sonia Aggarwal, Doug Arent, Inês L. Azevedo, Sally M. Benson, Thomas Bradley, Jack Brouwer, Yet Ming Chiang, Christopher T.M. Clack, Armond Cohen, Stephen Doig, Jae Edmonds, Paul Fennell, Christopher B. Field, Bryan Hannegan, Bri Mathias Hodge, Martin I. Hoffert, Eric Ingersoll, Paulina Jaramillo, Klaus S. Lackner, Katharine J. Mach, Michael Mastrandrea, Joan Ogden, Per F. Peterson, Daniel L. Sanchez, Daniel Sperling, Joseph Stagner, Jessika E. Trancik, Chi Jen Yang, and Ken Caldeira. Net-zero emissions energy systems. *Science*, 360(6396), 2018.

[2] Barbara Lothenbach and Maciej Zajac. Application of thermodynamic modelling to hydrated cements. *Cement and Concrete Research*, 123(May):105779, 2019.

[3] L J Parrot and D C Killoh. Prediction of cement hydration. *British Ceramic Proceedings*, 35:41–53, 1984.

[4] Tres Thoenen, Wolfgang Hummel, Urs R. Berner, and Enzo Curti. The PSI/Nagra Chemical Thermodynamic Database 12/07. Technical Report 14, Villigen PSI, Switzerland, 2014.

[5] I. D. Brown and R. D. Shannon. Empirical bond-strength–bond-length curves for oxides. *Acta Crystallographica Section A*, 29(3):266–282, 1973.

[6] H. R. Westrich, R. T. Cygan, W. H. Casey, C. Zemitis, and G. W. Arnold. The dissolution kinetics of mixed-cation orthosilicate minerals, 1993.

[7] Barbara Lothenbach, Gwenn Le Saout, Emmanuel Gallucci, and Karen Scrivener. Influence of limestone on the hydration of Portland cements. *Cement and Concrete Research*, 38(6):848–860, 2008.

[8] Barbara Lothenbach and Frank Winnefeld. Thermodynamic modelling of the hydration of Portland cement. *Cement and Concrete Research*, 36(2):209–226, 2006.

[9] Dmitrii A Kulik, Thomas Wagner, Svitlana V Dmytrieva, Georg Kosakowski, Ferdinand F Hingerl, Konstantin V Chudnenko, and Urs R Berner. GEM-Selektor geochemical modeling package: revised algorithm and GEMS3K nu-

merical kernel for coupled simulation codes. *Computational Geosciences*, 17(1):1–24, feb 2013.

[10] Thomas Wagner, Dmitrii A Kulik, Ferdinand F Hingerl, and Svitlana V Dmytrieva. GEM-Selektor geochemical modeling package: TSolMod library and data interface for multicomponent phase models. *The Canadian Mineralogist*, 50(5):1173–1195, oct 2012.

[11] B. Lothenbach, D.A. Kulik, T. Matschei, M. Balonis, L. Baquerizo, B.Z. Dilnesa, G.D. Miron, and Myers R. Cemdata18: A chemical thermodynamic database for hydrated Portland cements and alkali-activated materials. *Cement and Concrete Research*, 115(October 2018):472–506, 2018.

[12] M. B. Ali, R. Saidur, and M. S. Hossain. A review on emission analysis in cement industries. *Renewable and Sustainable Energy Reviews*, 15(5):2252–2261, 2011.

[13] Ellis M. Gartner and Donald E. MacPhee. A physico-chemical basis for novel cementitious binders. *Cement and Concrete Research*, 41(7):736–749, 2011.

[14] Karen L. Scrivener, Vanderley M. John, and Ellis M. Gartner. Eco-efficient cements: Potential economically viable solutions for a low-CO2 cement-based materials industry. *Cement and Concrete Research*, 114(June):2–26, 2018.

[15] Ruben Snellings. Assessing, understanding and unlocking supplementary cementitious materials. *RILEM Technical Letters*, 1:50, 2016.

[16] M. J. McCarthy, T. Robl, and L. J. Csetenyi. Recovery, processing, and usage of wet-stored fly ash. In *Coal Combustion Products (CCPs): Characteristics, Utilization and Beneficiation*, pages 343–367. Elsevier Ltd., 2017.

[17] Guoqing Geng, Rupert J. Myers, Jiaqi Li, Roya Maboudian, Carlo Carraro, David A. Shapiro, and Paulo J.M. Monteiro. Aluminum-induced dreierketten chain cross-links increase the mechanical properties of nanocrystalline calcium aluminosilicate hydrate. *Scientific Reports*, 7(March):1–10, 2017.

[18] J. Davidovits. Geopolymers - Inorganic polymeric new materials. *Journal of Thermal Analysis*, 37(8):1633–1656, 1991.

[19] V. D. Glukhovsky. Ancient, modern and future concretes. In *Proceedings of the First International Conference on Alkaline Cements and Concretes*, pages 1–9, 1994.

[20] J. L. Provis, S. L. Yong, and P. Duxson. Nanostructure/microstructure of metakaolin geopolymers. In *Geopolymers: Structure, Processing, Properties and Industrial Applications*, pages 72–88. 2009.

[21] M. C G Juenger, F. Winnefeld, J. L. Provis, and J. H. Ideker. Advances in alternative cementitious binders. *Cement and Concrete Research*, 41(12):1232–1243, 2011.

[22] Maria C.G. Juenger, Ruben Snellings, and Susan A. Bernal. Supplementary cementitious materials: New sources, characterization, and performance insights. *Cement and Concrete Research*, 122(February):257–273, 2019.

[23] Hendrik G. van Oss. Iron and Steel Slag Mineral Commodity Summaries - U.S. Geological Survey. Technical report, 2019.

[24] International Copper Study Group. The World Copper Factbook 2018. Technical report, 2018.

[25] Bipra Gorai, R. K. Jana, and Premchand. Characteristics and utilisation of copper slag - A review. *Resources, Conservation and Recycling*, 39(4):299–313, 2003.

[26] M. Najimi, J. Sobhani, and A. R. Pourkhorshidi. Durability of copper slag contained concrete exposed to sulfate attack. *Construction and Building Materials*, 25(4):1895–1905, 2011.

[27] World Steel Association. World Steel in Figures 2020. Technical report, 2020.

[28] J. Setién, D. Hernández, and J. J. González. Characterization of ladle furnace basic slag for use as a construction material. *Construction and Building Materials*, 23(5):1788–1794, 2009.

[29] Caijun Shi. Characteristics and cementitious properties of ladle slag fines from steel production. *Cement and Concrete Research*, 32(3):459–462, 2002.

[30] Daniel Adolfsson, Ryan Robinson, Fredrik Engström, and Bo Björkman. Influence of mineralogy on the hydraulic properties of ladle slag. *Cement and Concrete Research*, 41(8):865–871, 2011.

[31] Meng Meng Wang, Cong Cong Zhang, and Fu Shen Zhang. An environmental benign process for cobalt and lithium recovery from spent lithium-ion batteries by mechanochemical approach. *Waste Management*, 51:239–244, 2016.

[32] Muhammad Salman, Özlem Cizer, Yiannis Pontikes, Lucie Vandewalle, Bart Blanpain, and Koen Van Balen. Effect of curing temperatures on the alkali activation of crystalline continuous casting stainless steel slag. *Advances in Cement Research*, 71(September):308–316, 2014.

[33] H. Motz and J. Geiseler. Products of steel slags an opportunity to save natural resources. *Waste Management*, 21(3):285–293, 2001.

[34] Huang Yi, Guoping Xu, Huigao Cheng, Junshi Wang, Yinfeng Wan, and Hui Chen. An overview of utilization of steel slag. *Procedia Environmental Sciences*, 16:791–801, 2012.

[35] M Kuhn, P Drissen, J Geiseler, and H Schrey. A new BOF slag treatment technology. In *2nd European Oxygen Steelmaking Congress*, page 445, Taranto, Italy, 1997.

[36] Chunwei Liu, Muxing Guo, Lieven Pandelaers, Bart Blanpain, and Shuigen Huang. Stabilization of free lime in BOF slag by melting and solidification in air. *Metallurgical and Materials Transactions B*, 47(6):3237–3240, 2016.

[37] D. M. Proctor, K. A. Fehling, E. C. Shay, J. L. Wittenborn, J. J. Green, C. Avent, R. D. Bigham, M. Connolly, B. Lee, T. O. Shepker, and M. A. Zak. Physical and chemical characteristics of blast furnace, basic oxygen furnace, and electric arc furnace steel industry slags. *Environmental Science and Technology*, 34(8):1576–1582, 2000.

[38] Nadine M. Piatak, Michael B. Parsons, and Robert R. Seal. *Characteristics and environmental aspects of slag: A review*, volume 57. Elsevier Ltd, 2015.

[39] Nurul Hidayah Roslan, Mohammad Ismail, Nur Hafizah A Khalid, and Bala Muhammad. Properties of concrete containing electric arc furnace steel slag and steel sludge. *Journal of Building Engineering*, 28(July 2019):101060, 2020.

[40] Mark E. Schlesinger, Matthew J. King, Kathryn C. Sole, and William G. Davenport. Matte Smelting Fundamentals. In *Extractive Metallurgy of Copper*, pages 73–88. 5th edition, 2011.

[41] Mark E. Schlesinger, Matthew J. King, Kathryn C. Sole, and William G. Davenport. Flash Smelting. *Extractive Metallurgy of Copper*, pages 89–110, 2011.

[42] Mark E. Schlesinger, Matthew J. King, Kathryn C. Sole, and William G. Davenport. Bath Matte Smelting. *Extractive Metallurgy of Copper*, pages 155–178, 2011.

[43] Mark E. Schlesinger, Matthew J. King, Kathryn C. Sole, and William G. Davenport. Submerged Tuyere Smelting. *Extractive Metallurgy of Copper*, pages 111–125, 2011.

[44] Mark E. Schlesinger, Matthew J. King, Kathryn C. Sole, and William G. Davenport. Converting of Copper Matte. In *Extractive Metallurgy of Copper*, pages 127–153. 5th edition, 2011.

[45] Caijun Shi, Christian Meyer, and Ali Behnood. Utilization of copper slag in cement and concrete. *Resources, Conservation and Recycling*, 52:1115–1120, 2008.

[46] Krishna Murari, Rafat Siddique, and K. K. Jain. Use of waste copper slag, a sustainable material. *Journal of Material Cycles and Waste Management*, 17(1):13–26, 2014.

[47] Khalifa S. Al-Jabri, Makoto Hisada, Salem K. Al-Oraimi, and Abdullah H. Al-Saidy. Copper slag as sand replacement for high performance concrete. *Cement and Concrete Composites*, 31(7):483–488, 2009.

[48] K. S. Al-Jabri, R. A. Taha, A. Al-Hashmi, and A. S. Al-Harthy. Effect of copper slag and cement by-pass dust addition on mechanical properties of concrete. *Construction and Building Materials*, 20(5):322–331, 2006.

[49] Akshaykumar M. Bhoi, Yogesh D. Patil, Hemant S. Patil, and Madhav P. Kadam. Feasibility assessment of incorporating copper slag as a sand substitute to attain sustainable production perspective in concrete. *Advances in Materials Science and Engineering*, 2018(Feasibility assessment of incorporating copper slag as a sand substitute to attain sustainable production perspective in concrete):1–11, 2018.

[50] John L. Provis and Susan A. Bernal. *RILEM State of the Art Report*, volume 13. 2014.

[51] A. Kuterasińska, J.; Król. Mechanical properties of alkali-acivated binders based on copper slag. *Architecture Civil Engineering Environment*, 3:61–67, 2015.

[52] Silviana Onisei, Alexios P. Douvalis, Annelies Malfliet, Arne Peys, and Yiannis Pontikes. Inorganic polymers made of fayalite slag: On the microstructure and behavior of Fe. *Journal of the American Ceramic Society*, 101(6):2245–2257, 2018.

[53] Amin Nazer, Jordi Payá, María Victoria Borrachero, and José Monzó. Use of ancient copper slags in Portland cement and alkali activated cement matrices. *Journal of Environmental Management*, 167:115–123, 2016.

[54] Karen Scrivener, Alexandre Ouzia, Patrick Juilland, and Aslam Kunhi Mohamed. Advances in understanding cement hydration mechanisms. *Cement and Concrete Research*, 124(June):105823, 2019.

[55] Xiaowei Ouyang, D. A. Koleva, Guang Ye, and K. van Breugel. Understanding the adhesion mechanisms between C-S-H and fillers. *Cement and Concrete Research*, 100(July):275–283, 2017.

[56] Karen L. Scrivener, Alison K. Crumbie, and Peter Laugesen. The interfacial transition zone (ITZ) between cement paste and aggregate in concrete. *Interface Science*, 12(4):411–421, 2004.

[57] Shuai Nie, Shuguang Hu, Fazhou Wang, Chuanlin Hu, Xinping Li, and Yaohong Zhu. Pozzolanic reaction of lightweight fine aggregate and its influence on the hydration of cement. *Construction and Building Materials*, 153:165–173, 2017.

[58] Davide Zampini, Surendra P Shah, and Hamlin M Jennings. Early age microstructure of the paste-aggregate interface and its evolution. *Journal of Materials Research*, 13(7):1888–1898, 1998.

[59] H. M. Rietveld. A profile refinement method for nuclear and magnetic structures. *Journal of Applied Crystallography*, 2:65–71, 1969.

[60] Stephen Brunauer, P. H. Emmett, and Edward Teller. Adsorption of gases in multimolecular layers. *Journal of the American Chemical Society*, 60(2):309–319, 1938.

[61] William C. Records, Youngmin Yoon, Jacqueline F. Ohmura, Nicolas Chanut, and Angela M. Belcher. Virus-templated Pt–Ni(OH) 2 nanonetworks for enhanced electrocatalytic reduction of water. *Nano Energy*, 58(December 2018):167–174, 2019.

[62] Brian Traynor, Ciara Mulcahy, Hugo Uvegi, Tunahan Aytas, Nicolas Chanut, and Elsa Olivetti. Dissolution of olivines from steel and copper slags in basic solution. *Cement and Concrete Research*, 133(March):106065, 2020.

[63] Hugo Uvegi, Piyush Chaunsali, Brian Traynor, and Elsa Olivetti. Reactivity of industrial wastes as measured through ICP-OES: A case study on siliceous Indian biomass ash. *Journal of the American Ceramic Society*, (October 2018):1–11, 2019.

[64] Per Aagaard and Harold C Helgeson. Thermodynamic and kinetic constraints on reaction rates among minerals and aqueous solutions. I. Theoretical considerations. *American Journal of Science*, 282:237–285, 1982.

[65] Eric H. Oelkers, Julien Declercq, Giuseppe D. Saldi, Sigurdur R. Gislason, and Jacques Schott. Olivine dissolution rates: A critical review. *Chemical Geology*, 500(June):1–19, 2018.

[66] F.K. Crundwell. The mechanism of dissolution of minerals in acidic and alkaline solutions: Part II Application of a new theory to silicates, aluminosilicates and quartz. *Hydrometallurgy*, 149:265–275, 2014.

[67] J. Donald Rimstidt, Susan L. Brantley, and Amanda A. Olsen. Systematic review of forsterite dissolution rate data. *Geochimica et Cosmochimica Acta*, 99:159–178, 2012.

[68] Roy A. Wogelius and John V. Walther. Olivine dissolution at 25°C: Effects of pH, CO2, and organic acids. *Geochimica et Cosmochimica Acta*, 55(4):943–954, 1991.

[69] Eric H. Oelkers. General kinetic description of multioxide silicate mineral and glass dissolution. *Geochimica et Cosmochimica Acta*, 65(21):3703–3719, 2001.

[70] John Bensted. Gamma-dicalcium silicate and its hydraulicity. *Cement and Concrete Research*, 8:73–76, 1978.

[71] R Trettin, G Oliew, C Stadelmann, and W Wieker. Very early age hydration of dicalcium silicate-polymorphs. *Cement and Concrete Research*, 21:757–764, 1991.

[72] Lubica Kriskova, Yiannis Pontikes, Özlem Cizer, Annelies Malfliet, Jan Dijkmans, Bert Sels, Koenraad Van Balen, and Bart Blanpain. Hydraulic behavior of mechanically and chemically activated synthetic merwinite. *Journal of the American Ceramic Society*, 97(12):3973–3981, 2014.

[73] Roy A. Wogelius and John V. Walther. Olivine dissolution kinetics at near-surface conditions. *Chemical Geology*, 97(1-2):101–112, 1992.

[74] Damien Daval, Denis Testemale, Nadir Recham, Jean Marie Tarascon, Julien Siebert, Isabelle Martinez, and François Guyot. Fayalite (Fe2SiO4) dissolution kinetics determined by X-ray absorption spectroscopy. *Chemical Geology*, 275(3-4):161–175, 2010.

[75] Lara Duro, Fatima El Aamrani, Miquel Rovira, Javier Giménez, Ignasi Casas, Joan De Pablo, and Jordi Bruno. The dissolution of high-FeO olivine rock from the Lovasjärvi intrusion (SE-Finland) at 25°C as a function of pH. *Applied Geochemistry*, 20(7):1284–1291, 2005.

[76] Tor Løveng Olav Sunde, Tor Grande, and M. A. Einarsrud. Modified Pechini synthesis of oxide powders and thin films. In *Handbook of Sol-Gel Science and Technology*, pages 1–30. 2016.

[77] Ian Nettleship, James L. Shull, and Waltraud M. Kriven. Chemical preparation and phase stability of Ca2SiO4 and Sr2SiO4 powders. *Journal of the European Ceramic Society*, 11:291–298, 1993.

[78] Harold C. Helgeson, David H. Kirkham, and George C. Flowers. Theoretical prediction of the thermodynamic behavior of-aqueous electrolytes at high pressures and temperatures: IV. Calculation of activity coefficients, osmotic coefficients, and apparent molal and standard and relative partial molal properties to 600C. *American Journal of Science*, 281:1249–1516, 1981.

[79] Rupert J. Myers, Susan A. Bernal, and John L. Provis. A thermodynamic model for C-(N-)A-S-H gel: CNASH-ss. Derivation and validation. *Cement and Concrete Research*, 66:27–47, 2014.

[80] A. C. Lasaga and A. Luttge. Variation of crystal dissolution rate based on a dissolution stepwave model. *Science*, 291(March):2400–2405, 2001.

[81] K. L. Nagy and A. C. Lasaga. Dissolution and precipitation kinetics of gibbsite at 80°C and pH 3: The dependence on solution saturation state. *Geochimica et Cosmochimica Acta*, 56(8):3093–3111, 1992.

[82] Andreas Luttge, Edward Bolton, and A. C. Lasaga. An interferometric study of the dissolution kinetics of anorthite: The role of reactive surface area. *American Journal of Science*, 299:652–678, 1999.

[83] Oleg S. Pokrovsky and Jacques Schott. Kinetics and mechanism of forsterite dissolution at 25 ° C and pH from 1 to 12. *Geochimica et Cosmochimica Acta*, 64(19):3313–3325, 2000.

[84] Robert A. Berner and Jacques Schott. Mechanism of pyroxene and amphibole weathering II observations of soil grains. *American Journal of Science*, 282:1214–1231, 1982.

[85] M F Jr Hochella and A H Carim. A reassessment of electron escape depths in silicon and thermally grown silicon dioxide thin films. *Surface Science*, 197:260–268, 1988.

[86] V. P. Zakaznova-Herzog, H. W. Nesbitt, G. M. Bancroft, and J. S. Tse. Characterization of leached layers on olivine and pyroxenes using high-resolution XPS and density functional calculations. *Geochimica et Cosmochimica Acta*, 72(1):69–86, 2008.

[87] Patrick V. Brady and John V. Walther. Controls on silicate dissolution rates in neutral and basic pH solutions at 25°C. *Geochimica et Cosmochimica Acta*, 53(11):2823–2830, 1989.

[88] A. Blum and A. C. Lasaga. Role of surface speciation in the low-temperature dissolution of minerals. *Nature*, 331(4):431–433, 1988.

[89] Eric H. Oelkers. An experimental study of forsterite dissolution rates as a function of temperature and aqueous Mg and Si concentrations. *Chemical Geology*, 175(3-4):485–494, 2001.

[90] Oleg S. Pokrovsky and Jacques Schott. Forsterite surface composition in aqueous solutions: A combined potentiometric, electrokinetic, and spectroscopic approach. *Geochimica et Cosmochimica Acta*, 64(19):3299–3312, 2000.

[91] K Fujimoto, K Fukutani, M Tsunoda, H Yamashita, and K Kobayashi. Hydrogen depth profiling using the 1H(15 N, $\alpha\gamma$) 12 C reaction in stainless steel pre-irradiated with helium ions. *Geochemical Journal*, 27:155–162, 1993.

[92] Haruhiko Seyama, Mitsuyuki Soma, and Atsushi Tanaka. Surface characterization of acid-leached olivines by X-ray photoelectron spectroscopy. *Chemical Geology*, 129(3-4):209–216, 1996.

[93] Robert W. Luce, Robert W. Bartlett, and George A. Parks. Dissolution kinetics of magnesium silicates. *Geochimica et Cosmochimica Acta*, 36(1):35–50, 1972.

[94] R. Hellmann, J. M. Penisson, R. L. Hervig, J. H. Thomassin, and M. F. Abrioux. An EFTEM/HRTEM high-resolution study of the near surface of labradorite feldspar altered at acid pH: Evidence for interfacial dissolution-reprecipitation. *Physics and Chemistry of Minerals*, 30(4):192–197, 2003.

[95] Encarnación Ruiz-Agudo, Christine V. Putnis, Carlos Rodriguez-Navarro, and Andrew Putnis. Mechanism of leached layer formation during chemical weathering of silicate minerals. *Geology*, 40(10):947–950, 2012.

[96] E. Ruiz-Agudo, C. V. Putnis, and A. Putnis. Coupled dissolution and precipitation at mineral-fluid interfaces. *Chemical Geology*, 383:132–146, 2014.

[97] Roland Hellmann, Richard Wirth, Damien Daval, Jean Paul Barnes, Jean Michel Penisson, Delphine Tisserand, Thierry Epicier, Brigitte Florin, and Richard L. Hervig. Unifying natural and laboratory chemical weathering with interfacial dissolution-reprecipitation: A study based on the nanometer-scale chemistry of fluid-silicate interfaces. *Chemical Geology*, 294-295:203–216, 2012.

[98] Alexander S. Brand, Justin M. Gorham, and Jeffrey W. Bullard. Dissolution rate spectra of β-dicalcium silicate in water of varying activity. *Cement and Concrete Research*, 118(February):69–83, 2019.

[99] Kate Maher, Natalie C. Johnson, Ariel Jackson, Laura N. Lammers, Abe B. Torchinsky, Karrie L. Weaver, Dennis K. Bird, and Gordon E. Brown. A spatially resolved surface kinetic model for forsterite dissolution. *Geochimica et Cosmochimica Acta*, 174:313–334, 2016.

[100] A P Grosvenor, B A Kobe, M C Biesinger, and N S Mcintyre. Investigation of multiplet splitting of Fe 2p XPS spectra and bonding in iron compounds. *Surface and Interface Analysis*, 36:1564–1574, 2004.

[101] Sergey V. Golubev, Oleg S. Pokrovsky, and Jacques Schott. Experimental determination of the effect of dissolved CO2 on the dissolution kinetics of Mg and Ca silicates at 25 °C. *Chemical Geology*, 217(3-4 SPEC. ISS.):227–238, 2005.

[102] Jacques Schott and Robert A. Berner. X-ray photoelectron studies of the mechanism of iron silicate dissolution during weathering. *Geochimica et Cosmochimica Acta*, 47(12):2233–2240, 1983.

[103] Jacques Schott and Robert A. Berner. Dissolution mechanisms of pyroxenes and olivines during weathering. In *The Chemistry of Weathering*, pages 35–53. 1985.

[104] Sylvie Pourchet, Isabelle Pochard, Fabrice Brunel, and Danièle Perrey. Chemistry of the calcite/water interface: Influence of sulfate ions and consequences in terms of cohesion forces. *Cement and Concrete Research*, 52:22–30, 2013.

[105] Thomas Foxall, Gordon C. Peterson, Henry M. Rendall, and Alec L. Smith. Charge determination at calcium salt/aqueous solution interface. *Journal of the Chemical Society, Faraday Transactions 1: Physical Chemistry in Condensed Phases*, 75(2):1034–1039, 1979.

[106] Anya Vollpracht, Barbara Lothenbach, Ruben Snellings, and Johannes Haufe. The pore solution of blended cements: a review. *Materials and Structures*, 49(8):3341–3367, 2016.

[107] Xin Chen, Shuaifei Wei, Qianqian Wang, Mingliang Tang, Xiaodong Shen, Xin Zou, Yusheng Shen, and Bing Ma. Morphology prediction of portlandite: Atomistic simulations and experimental research. *Applied Surface Science*, 502(September 2019):144296, 2020.

[108] Sandra Galmarini, Anne Aimable, Nicolas Ruffray, and Paul Bowen. Changes in portlandite morphology with solvent composition: Atomistic simulations and experiment. *Cement and Concrete Research*, 41(12):1330–1338, 2011.

[109] Sidney Diamond. Cement past microstructure - an overview at several levels. In *Hydraulic cement pastes: their structure and properties*, pages 2–30, 1976.

[110] Zhidong Zhang, George W. Scherer, and Alexandre Bauer. Morphology of cementitious material during early hydration. *Cement and Concrete Research*, 107(January):85–100, 2018.

[111] Wieslaw Kurdowski. *Cement and Concrete Chemistry*. Springer, 2014.

[112] Warda Ashraf and Jan Olek. Carbonation behavior of hydraulic and non-hydraulic calcium silicates: potential of utilizing low-lime calcium silicates in cement-based materials. *Journal of Materials Science*, 51(13):6173–6191, 2016.

[113] Yongjia He, Xiaogang Zhao, Linnu Lu, Leslie J. Struble, and Shuguang Hu. Effect of C/S ratio on morphology and structure of hydrothermally synthesized calcium silicate hydrate. *Journal Wuhan University of Technology, Materials Science Edition*, 26(4):770–773, 2011.

[114] Riccardo Maddalena, Kefei Li, Philip A. Chater, Stefan Michalik, and Andrea Hamilton. Direct synthesis of a solid calcium-silicate-hydrate (C-S-H). *Construction and Building Materials*, 223:554–565, 2019.

[115] Chilakala Ramakrishna, Thriveni Thenepalli, and Ji Whan Ahn. A brief review of aragonite precipitated calcium carbonate (PCC) synthesis methods and its applications-. *Korean Chemical Engineering Research*, 55(4):443–455, 2017.

[116] Jinyang Jiang, Qi Zheng, Dongshuai Hou, Yiru Yan, Heng Chen, Wei She, Shengping Wu, Dong Guo, and Wei Sun. Calcite crystallization in the cement system: Morphological diversity, growth mechanism and shape evolution. *Physical Chemistry Chemical Physics*, 20(20):14174–14181, 2018.

[117] Pablo Cubillas, K Stephan, Manuel Prieto, Claire Chairat, and Eric H Oelkers. Experimental determination of the dissolution rates of calcite, aragonite, and bivalves. *Chemical Geology*, 216:59–77, 2005.

[118] Nicolas C.M. Marty, Francis Claret, Arnault Lassin, Joachim Tremosa, Philippe Blanc, Benoit Madé, Eric Giffaut, Benoit Cochepin, and Christophe Tournassat. A database of dissolution and precipitation rates for clay-rocks minerals. *Applied Geochemistry*, 55:108–118, 2015.

[119] Kevin G. Knauss, Son N. Nguyen, and Homer C. Weed. Diopside dissolution kinetics as a function of pH, CO2, temperature, and time. *Geochimica et Cosmochimica Acta*, 57(2):285–294, 1993.

[120] Sergey V Golubev and Oleg S Pokrovsky. Experimental study of the effect of organic ligands on diopside dissolution kinetics. 235:377–389, 2006.

[121] Sougata Halder. *Experimental determination of the dissolution mechanism of Ca and Mg pyroxenes/pyroxenoids in alkaline solutions*. PhD thesis, Southern Methodist University, 2009.

[122] Octave Levenspiel. Chapter 25: Fluid-Particle Reactions: Kinetics. In *Chemical Reaction Engineering*. 1999.

[123] Franco Zunino and Karen Scrivener. The reaction between metakaolin and limestone and its effect in porosity refinement and mechanical properties. *Cement and Concrete Research*, 140:106307, 2021.

[124] John L. Provis. Alkali-activated materials. *Cement and Concrete Research*, 2016.

[125] Hoang Nguyen, Elijah Adesanya, Katja Ohenoja, Lubica Kriskova, Yiannis Pontikes, Paivo Kinnunen, and Mirja Illikainen. Byproduct-based ettringite binder – A synergy between ladle slag and gypsum. *Construction and Building Materials*, 197:143–151, 2019.

[126] Katrijn Gijbels, Hoang Nguyen, Paivo Kinnunen, Wouter Schroeyers, Yiannis Pontikes, Sonja Schreurs, and Mirja Illikainen. Feasibility of incorporating phosphogypsum in ettringite-based binder from ladle slag. *Journal of Cleaner Production*, 237:117793, 2019.

[127] Arne Peys, Alexios P. Douvalis, Vincent Hallet, Hubert Rahier, Bart Blanpain, and Yiannis Pontikes. Inorganic Polymers From CaO-FeOx-SiO2 Slag: The Start of Oxidation of Fe and the Formation of a Mixed Valence Binder. *Frontiers in Materials*, 6(August):1–10, 2019.

[128] R. C. Kaze, L. M. Beleuk à Moungam, M. L. Fonkwe Djouka, A. Nana, E. Kamseu, U. F. Chinje Melo, and C. Leonelli. The corrosion of kaolinite by iron minerals and the effects on geopolymerization. *Applied Clay Science*, 138:48–62, 2017.

[129] Kelly Cristiane Gomes, G. S.T. Lima, Sandro Marden Torres, Silvio De Barros, Igor Frota Vasconcelos, and Normando Perazzo Barbosa. Iron distribution

in geopolymer with ferromagnetic rich precursor. *Materials Science Forum*, 643(December):131–138, 2010.

[130] C. Hall, D. J. Large, B. Adderley, and H. M. West. Calcium leaching from waste steelmaking slag: Significance of leachate chemistry and effects on slag grain mineralogy. *Minerals Engineering*, 65:156–162, 2014.

[131] L M Juckes. The volume stability of modern steelmaking slags. *Mineral Processing and Extractive Metallurgy*, 112(3):177–197, 2003.

[132] Tung Hsin Su, Huai Jen Yang, Yen Hong Shau, Eiichi Takazawa, and Yu Chen Lee. CO2 sequestration utilizing basic-oxygen furnace slag: Controlling factors, reaction mechanisms and V-Cr concerns. *Journal of Environmental Sciences (China)*, 41:99–111, 2016.

[133] Rafael M. Santos, Da Ling, Amin Sarvaramini, Muxing Guo, Jan Elsen, Faïçal Larachi, Georges Beaudoin, Bart Blanpain, and Tom Van Gerven. Stabilization of basic oxygen furnace slag by hot-stage carbonation treatment. *Chemical Engineering Journal*, 203:239–250, 2012.

[134] Samir I. Abu-Eishah, Amr S. El-Dieb, and Mostafa S. Bedir. Performance of concrete mixtures made with electric arc furnace (EAF) steel slag aggregate produced in the Arabian Gulf region. *Construction and Building Materials*, 34:249–256, 2012.

[135] Rafael Schouwenaars and María Rosa Ramírez Zamora. Microscopic analysis of iron and steel slag used as a source of cationic precipitation agents in water treatment. In *The Second International Conference on Materials Chemistry and Environmental Protection (MEEP 2018)*, pages 297–300, 2018.

[136] Pao Ter Teo, Anasyida Abu Seman, Projjal Basu, and Nurulakmal Mohd Sharif. Chemical, thermal and phase analysis of malaysia's Electric Arc Furnace (EAF) slag waste. *Materials Science Forum*, 840:399–403, 2016.

[137] Alexander S. Brand and Jeffery R. Roesler. Interfacial transition zone of cement composites with steel furnace slag aggregates. *Cement and Concrete Composites*, 86:117–129, 2018.

[138] Jianxin Li, Qijun Yu, Jiangxiong Wei, and Tongsheng Zhang. Structural characteristics and hydration kinetics of modified steel slag. *Cement and Concrete Research*, 41(3):324–329, 2011.

[139] M Gelfi, G Cornacchia, and R Roberti. Investigations on leaching behavior of EAF steel slags. *Euroslag 2010*, pages 1–12, 2010.

[140] Muhammad Salman, Ozlem Cizer, Yiannis Pontikes, Ruben Snellings, Lucie Vandewalle, Bart Blanpain, and Koen Van Balen. Cementitious binders from activated stainless steel refining slag and the effect of alkali solutions. *Journal of Hazardous Materials*, 286:211–219, 2015.

[141] Maria Nicolae, Irina Vîlciu, and Florian Zaman. X-ray diffraction analysis of steel slag and blast furnace slag viewing their use for road construction. *UPB Sci. Bull.*, 69(2), 2007.

[142] Corey A Myers, Takao Nakagaki, and Kosei Akutsu. Quantification of the CO2 mineralization potential of ironmaking and steelmaking slags under direct gas-solid reactions in flue gas. *International Journal of Greenhouse Gas Control*, 87(December 2018):100–111, 2019.

[143] Martina Vítková, Vojtěch Ettler, Martin Mihaljevič, and Ondřej Šebek. Effect of sample preparation on contaminant leaching from copper smelting slag. *Journal of Hazardous Materials*, 197:417–423, 2011.

[144] Bartosz Mikoda, Harry Kucha, Anna Potysz, and Ewa Kmiecik. Metallurgical slags from Cu production and Pb recovery in Poland – Their environmental stability and resource potential. *Applied Geochemistry*, 98(September):459–472, 2018.

[145] Vojtěch Ettler, Zdenek Johan, Bohdan Kříbek, Ondřej Šebek, and Martin Mihaljevič. Mineralogy and environmental stability of slags from the Tsumeb smelter, Namibia. *Applied Geochemistry*, 24(1):1–15, 2009.

[146] I Mihailova and D Mehandjiev. Characterization of fayalite from copper slags. *Journal of the University of Chemical Technology and Metallurgy*, 45(3):317–326, 2010.

[147] Alice Jarosikova, V Ettler, Martin Mihaljevic, Bohdan Kribek, and Ben Mapani. The pH-dependent leaching behavior of slags from various stages of a copper smelting process: Environmental implications. *Journal of Environmental Management*, 187:178–186, 2017.

[148] Sandeep Panda, Srabani Mishra, Danda Srinivas Rao, Nilotpala Pradhan, Umaballava Mohapatra, Shivakumar Angadi, and Barada Kanta Mishra. Extraction of copper from copper slag: Mineralogical insights, physical beneficiation and bioleaching studies. *Korean Journal of Chemical Engineering*, 32(4):667–676, 2015.

[149] X Wang, D Geysen, S V Padilla Tinoco, N D Hoker, T Van Gerven, X Wang, D Geysen, S V Padilla Tinoco, N D Hoker, T Van Gerven, and B Blanpain. Characterisation of copper slag in view of metal recovery. *Mineral Processing and Extractive Metallurgy*, 124(2):83–87, 2015.

[150] M. Vítková, V. Ettler, Z. Johan, B. Kříbek, O. Šebek, and M. Mihaljevič. Primary and secondary phases in copper-cobalt smelting slags from the Copperbelt Province, Zambia. *Mineralogical Magazine*, 74(4):581–600, 2010.

[151] Anna Potysz, Jakub Kierczak, Yves Fuchs, Malgorzata Grybos, Piet N L Lens, and Eric D Van Hullebusch. Characterization and pH-dependent leaching behaviour of historical and modern copper slags. *Journal of Geochemical Exploration*, 160:1–15, 2015.

[152] Mathieu Gautier, Jacques Poirier, Francoise Bodenan, Gilles Franceschini, and Emmanuel Veron. Basic Oxygen Furnace (BOF) slag cooling: Laboratory characteristics and prediction calculations. *International Journal of Mineral Processing*, 94:93–101, 2013.

[153] Min woo Choi and Sung Mo Jung. Crystallization behavior of melted BOF slag during non-isothermal constant cooling process. *Journal of Non-Crystalline Solids*, 468(February):105–112, 2017.

[154] A Srinivasa Reddy, R K Pradhan, and Sanjay Chandra. Utilization of Basic Oxygen Furnace (BOF) slag in the production of a hydraulic cement binder. *International Journal of Mineral Processing*, 79:98–105, 2006.

[155] DC Goldring and LM Juckes. Petrology and stability of LD slag. *lronmaking & Steelmaking*, 24:447–456, 1997.

[156] J Waligora, D Bulteel, P Degrugilliers, D Damidot, J L Potdevin, and M Measson. Chemical and mineralogical characterizations of LD converter steel slags: A multi-analytical techniques approach. *Materials Characterization*, 61:39–48, 2010.

[157] M. Tossavainen, F. Engstrom, Q. Yang, N. Menad, M. Lidstrom Larsson, and B. Bjorkman. Characteristics of steel slag under different cooling conditions. *Waste Management*, 27(10):1335–1344, 2007.

[158] Andrew J Hobson, Douglas I Stewart, Andrew W Bray, Robert J G Mortimer, William M Mayes, Michael Rogerson, and Ian T Burke. Mechanism of vanadium leaching during surface weathering of basic oxygen furnace steel slag blocks: A microfocus x-ray absorption spectroscopy and electron microscopy study. *Environmental Science & Technology*, 51:78237830, 2017.

[159] Essia Belhadj, Cécile Diliberto, and André Lecomte. Characterization and activation of Basic Oxygen Furnace slag. *Cement and Concrete Composites*, 34(1):34–40, 2012.

[160] A M Kaja, K Schollbach, S Melzer, S R Van Der Laan, H J H Brouwers, and Qingliang Yu. Hydration of potassium citrate-activated BOF slag. *Cement and Concrete Research*, 140(November 2020):106291, 2021.

[161] Perrine Chaurand, Jérôme Rose, Jérémie Domas, and Jean Yves Bottero. Speciation of Cr and V within BOF steel slag reused in road constructions. *Journal of Geochemical Exploration*, 88(1-3 SPEC. ISS.):10–14, 2006.

[162] Raghavendra Ragipani, Sankar Bhattacharya, and Akkihebbal K. Suresh. Kinetics of steel slag dissolution: From experiments to modelling. *Proceedings of the Royal Society A: Mathematical, Physical and Engineering Sciences*, 475(2224), 2019.

[163] Jihui Zhao, Peiyu Yan, and Dongmin Wang. Research on mineral characteristics of converter steel slag and its comprehensive utilization of internal and external recycle. *Journal of Cleaner Production*, 156:50–61, 2017.

[164] G. Cornacchia, S. Agnelli, M. Gelfi, G. Ramorino, and R. Roberti. Reuse of EAF Slag as Reinforcing Filler for Polypropylene Matrix Composites. *Jom*, 67(6):1370–1378, 2015.

[165] D. Mombelli, C. Mapelli, S. Barella, C. Di Cecca, G. Le Saout, and E. Garcia-Diaz. The effect of microstructure on the leaching behaviour of electric arc furnace (EAF) carbon steel slag. *Process Safety and Environmental Protection*, 102:810–821, 2016.

[166] Radmila Milačič, Tea Zuliani, Tina Oblak, Ana Mladenovič, and Janez Ščančar. Environmental Impacts of Asphalt Mixes with Electric Arc Furnace Steel Slag. *Journal of Environmental Quality*, 40(4):1153–1161, 2011.

[167] Simone Neuhold, David Algermissen, Peter Drissen, Burkart Adamczyk, Peter Presoly, Klaus P. Sedlazeck, Johannes Schenk, Johann G. Raith, Roland Pomberger, and Daniel Vollprecht. Tailoring the FeO/SiO2 ratio in electric arc furnace slags to minimize the leaching of vanadium and chromium. *Applied Sciences (Switzerland)*, 10(7), 2020.

[168] Idoia Arribas, Amaia Santamaría, Estela Ruiz, Vanesa Ortega-López, and Juan M. Manso. Electric arc furnace slag and its use in hydraulic concrete. *Construction and Building Materials*, 90:68–79, 2015.

[169] Maud Herbelin, Jerome Bascou, Veronique Lavastre, Damien Guillaume, Mhammed Benbakkar, Steve Peuble, and Jean-Philippe Baron. Steel slag characterisation—benefit of coupling chemical, mineralogical and magnetic techniques. *Minerals*, 10(705):1–19, 2010.

[170] Luckman Muhmood, Satish Vitta, and D. Venkateswaran. Cementitious and pozzolanic behavior of electric arc furnace steel slags. *Cement and Concrete Research*, 39(2):102–109, 2009.

[171] G. Adegoloye, A. L. Beaucour, S. Ortola, and A. Noumowe. Mineralogical composition of EAF slag and stabilised AOD slag aggregates and dimensional stability of slag aggregate concretes. *Construction and Building Materials*, 115:171–178, 2016.

[172] Jurgen Geiseler, Ruth Schlosser, Rudiger Scheel, Klaus Koch, and Dieter Janke. Untersuchungen zum hydratationsverhalten von synthetischen magnesiowustiten. *Steel Research*, 58(5):210–214, 1987.

[173] G R Qian, D D Sun, J H Tay, and Z Y Lai. Hydrothermal reaction and autoclave stability of Mg bearing RO phase in steel slag. *British Ceramic Transactions*, 101(4):159–164, 2002.

[174] J. E.Hun Jang and Susan L. Brantley. Investigation of wüstite (FeO) dissolution: Implications for reductive dissolution of ferric oxides. *Environmental Science and Technology*, 43(4):1086–1090, 2009.

[175] Ida Strandkvist, Ake Sandström, and Fredrik Engström. Effect of FeO/MgO ratio on dissolution and leaching of magnesiowüstite. *Steel Research International*, 88:1600322, 2017.

[176] David A Vermilyea. The Dissolution of MgO and Mg(OH)2 in aqueous solutions. *Journal of The Electrochemical Society*, 116:1179–1183, 1969.

[177] Art F White, Maria L Peterson, and Michael F Hochella. Electrochemistry and dissolution kinetics of magnetite and ilmenite. *Geochim. Cosmochim. Acta*, 58(8):1859–1875, 1994.

[178] Miguel A Blesa, Horacio A Marinovich, Erwin C Baumgartner, and Alberto J G Maroto. Mechanism of dissolution of magnetite by oxalic acid-ferrous ion solutions. *Inorganic Chemistry*, 26:3713–3717, 1987.

[179] Yogarajah Elakneswaran, Eiji Owaki, Shigeyoshi Miyahara, Masataka Ogino, Tsuyoshi Maruya, and Toyoharu Nawa. Hydration study of slag-blended cement based on thermodynamic considerations. *Construction and Building Materials*, 124:615–625, 2016.

[180] Nicola Meller, Christopher Hall, Andrew C Jupe, Sally L Colston, Simon D M Jacques, and Jonathan Phipps. The paste hydration of brownmillerite with and without gypsum : a time resolved synchrotron diffraction study at 30 , 70 , 100 and 150 u C. *Journal of Materials Chemistry*, 14:428–435, 2004.

[181] Xiao Huang, Fazhou Wang, Shuguang Hu, Yang Lu, Meijuan Rao, and Yuandong Mu. Brownmillerite hydration in the presence of gypsum: The effect of Al/Fe ratio and sulfate ions. *Journal of American Ceramic Society*, 102(9):5545–5554, 2019.

[182] Elmer T Carlson. Properties of the Calcium Aluminoferrite Hydrates. Technical report, 1966.

[183] Ida Strandkvist. *Minimisation of Chromium Leaching from Low-Alloy Electric Arc Furnace Slag by Mineral Modifications*. PhD thesis, 2020.

[184] Charity M Phillips-Lander, Andrew S Elwood Madden, Elisabeth M Hausrath, and Megan E Elwood Madden. Aqueous alteration of pyroxene in sulfate, chloride, and perchlorate brines: Implications for post-Noachian aqueous alteration on Mars. *Geochimica et Cosmochimica Acta*, 257:336–353, 2019.

[185] Suvasis Dixit and Susan A. Carroll. Effect of solution saturation state and temperature on diopside dissolution. *Geochemical Transactions*, 8:1–14, 2007.

[186] Gabrielle J. Stockmann, Domenik Wolff-Boenisch, Sigurdur R. Gislason, and Eric H. Oelkers. Do carbonate precipitates affect dissolution kinetics? 2: Diopside. *Chemical Geology*, 337-338:56–66, 2013.

[187] Eric H. Oelkers and Jacques Schott. An experimental study of enstatite dissolution rates as function of pH, temperature, and aqueous Mg and Si concentration, and the mechanism of pyroxene/pyroxenoid dissolution. *Geochimica et Cosmochimica Acta*, 65(8):1219–1231, 2001.

[188] Sougata Halder and John V Walther. Far from equilibrium enstatite dissolution rates in alkaline solutions at earth surface conditions. *Geochimica et Cosmochimica Acta*, 75:7486–7493, 2011.

[189] Erich J Weissbart and Donald J Rimstidt. Wollastonite: Incongruent dissolution and leached layer formation. *Geochimica et Cosmochimica Acta*, 64(23):4007–4016, 2000.

[190] O. S. Pokrovsky, L. S. Shirokova, P. Bénézeth, J. Schott, and S. V. Golubev. Effect of organic ligands and heterotrophic bacteria on wollastonite dissolution kinetics. *American Journal of Science*, 309(8):731–772, 2009.

[191] Ronghua Zhang, Xuetong Zhang, Bernard Guy, Shumin Hu, Dominique De Ligny, and Jacques Moutte. Experimental study of dissolution rates of hedenbergitic clinopyroxene at high temperatures: dissolution in water from 25 °C to 374 °C. *European Journal of Mineralogy*, 25(3):353–372, 2013.

[192] A. R. Hoch, M. M. Reddy, and J. I. Drever. The effect of iron content and dissolved O2 on dissolution rates of clinopyroxene at pH 5.8 and 25°C: Preliminary results. *Chemical Geology*, 132(1-4 SPEC. ISS.):151–156, 1996.

[193] C André Ohlin, Eric M Villa, James R Rustad, and William H Casey. Dissolution of insulating oxide materials at the molecular scale. *Nature Materials*, 9:11–19, 2010.

[194] William H Casey and Henry R Westricht. Control of dissolution rates of orthosilicate minerals by divalent metal-oxygen bonds. *Nature*, 355(January):157–159, 1992.

[195] Mohsen Ben Haha, Frank Winnefeld, and Alexander Pisch. Advances in understanding ye'elimite-rich cements. *Cement and Concrete Research*, 123(July):105778, 2019.

[196] F. Engström, D. Adolfsson, C. Samuelsson, Å Sandström, and B. Björkman. A study of the solubility of pure slag minerals. *Minerals Engineering*, 41:46–52, 2013.

[197] C M George. Industrial aluminous cements. In *Structure and Performance of Cements*, pages 415–470. 1983.

[198] Hae-geun Park, Sang-kyoung Sung, Chan-gi Park, and Jong-pil Won. Influence of a C12A7 mineral-based accelerator on the strength and durability of shotcrete. *Cement and Concrete Research*, 38:379–385, 2008.

[199] Ying Wang, Wen Ni, and Prannoy Suraneni. Use of ladle furnace slag and other industrial by-products to encapsulate chloride in municipal. *Materials*, 12(925):1–14, 2019.

[200] Ying Wang and Prannoy Suraneni. Experimental methods to determine the feasibility of steel slags as supplementary cementitious materials. *Construction and Building Materials*, 204:458–467, 2019.

[201] N Yannaquis. No Title. *Rev. Mater. Constr.*, 480(213), 1955.

[202] George A Lager and E P Meagher. High-temperature structural study of six olivines. *American Mineralogist*, 63:365–377, 1978.

[203] Yilun Zhang, Donald J Rimstidt, Yi Huang, and Chen Zhu. Kyanite far from equilibrium dissolution rate at 0 – 22 ° C and pH. *Acta Geochimica*, 38(4):472–480, 2019.

[204] L. Nicoleau, A. Nonat, and D. Perrey. The di- and tricalcium silicate dissolutions. *Cement and Concrete Research*, 47:14–30, 2013.

[205] Ian M Ritchie and X U Bing-An. The kinetics of lime slaking. *Hydrometallurgy*, 23:377–396, 1990.

[206] F. Puertas, A. Fernández-Jiménez, and M. T. Blanco-Varela. Pore solution in alkali-activated slag cement pastes. Relation to the composition and structure of calcium silicate hydrate. *Cement and Concrete Research*, 34(1):139–148, 2004.

[207] Astrid Gruskovnjak, Barbara Lothenbach, Lorenz Holzer, Renato Figi, and Frank Winnefeld. Hydration of alkali-activated slag: Comparison with ordinary Portland cement. *EMPA Activities*, (2006):34, 2006.

[208] Redmond R. Lloyd, John L. Provis, and Jannie S.J. Van Deventer. Pore solution composition and alkali diffusion in inorganic polymer cement. *Cement and Concrete Research*, 40(9):1386–1392, 2010.

[209] Wenrui Wang, Huisu Chen, Xiangyu Li, and Zhigang Zhu. Corrosion behavior of steel bars immersed in simulated pore solutions of alkali-activated slag mortar. *Construction and Building Materials*, 143:289–297, 2017.

[210] Yibing Zuo, Marija Nedeljković, and Guang Ye. Pore solution composition of alkali-activated slag/fly ash pastes. *Cement and Concrete Research*, 115(January 2018):230–250, 2019.

[211] Marija Nedeljkovic, Kamel Arbi, Yibing Zuo, and Guang Ye. Physical properties and pore solution analysis of alkali activated fly ash-slag pastes. In *International RILEM Conference on Materials, Systems and Structures in Civil Engineering Conference segment on Concrete with Supplementary Cementitious materials*, number August, 2016.

[212] Sujin Song and Hamlin M. Jennings. Pore solution chemistry of alkali-activated ground granulated blast-furnace slag. *Cement and Concrete Research*, 29(2):159–170, 1999.

[213] Yibing Zuo, Marija Nedeljkovic, and Guang Ye. Coupled thermodynamic modelling and experimental study of sodium hydroxide activated slag. *Construction and Building Materials*, 188:262–279, 2018.

[214] Xiaodi Dai, Serdar Aydin, Mert Yücel Yardimci, Karel Lesage, and Geert de Schutter. Influence of water to binder ratio on the rheology and structural Build-up of Alkali-Activated Slag/Fly ash mixtures. *Construction and Building Materials*, 264:120253, 2020.

[215] Ce Sun, Jianwei Sun, and Dongmin Wang. Effect of tartaric acid on the early hydration of NaOH-activated slag paste. *Journal of Thermal Analysis and Calorimetry*, (0123456789), 2020.

[216] A.R. Robie and B.S. Hemingway. Thermodynamic Properties of Minerals and Related Substances at 298.15 K and 1 Bar (105 Pascals) Pressure and at Higher Temperatures. Technical report, USGS, 1995.

[217] L. Kriskova, M. Eroli, R.I. Iacobescu, S. Onisei, F. Vecchiocattivi, and Y. Pontikes. Transformation of stainless steel slag toward a reactive cementitious binder. *Journal of the American Ceramic Society*, 101(4), 2018.

[218] Brian Traynor, Hugo Uvegi, Elsa Olivetti, Barbara Lothenbach, and Rupert J Myers. Methodology for pH measurement in high alkali cementitious systems. *Cement and Concrete Research*, 135(May):106122, 2020.

[219] Alexander M. Vaysburd and Peter H. Emmons. Corrosion inhibitors and other protective systems in concrete repair: Concepts or misconcepts. *Cement and Concrete Composites*, 26(3):255–263, 2004.

[220] C. L. Page and K. W. J. Treadaway. Aspects of the electrochemistry of steel in concrete. *Nature*, 297:109–115, 1982.

[221] Seishi Goto, Kiyoshi Akawaza, and Masaki Daimon. Solubility of silica-alumina gels in different pH solutions. *Cement and Concrete Research*, 22:1216–1223, 1992.

[222] C. K. Yip, G. C. Lukey, and J. S J Van Deventer. The coexistence of geopolymeric gel and calcium silicate hydrate at the early stage of alkaline activation. *Cement and Concrete Research*, 35(9):1688–1697, 2005.

[223] J. G.S. Van Jaarsveld and J. S.J. Van Deventer. Effect of the alkali metal activator on the properties of fly ash-based geopolymers. *Industrial and Engineering Chemistry Research*, 38(10):3932–3941, 1999.

[224] B. Mota, T. Matschei, and K. Scrivener. Impact of NaOH and Na2SO4 on the kinetics and microstructural development of white cement hydration. *Cement and Concrete Research*, 108(February):172–185, 2018.

[225] E. L'Hôpital, B. Lothenbach, K. Scrivener, and D. A. Kulik. Alkali uptake in calcium alumina silicate hydrate (C-A-S-H). *Cement and Concrete Research*, 85:122–136, 2016.

[226] Roger G. Bates, Vincent E. Bower, and Edgar R. Smith. Calcium hydroxide as a highly alkaline pH standard. *Journal of Research of the National Bureau of Standards*, 56(6):305–312, 1956.

[227] Rupert J. Myers, Emilie L'Hôpital, John L. Provis, and Barbara Lothenbach. Effect of temperature and aluminium on calcium (alumino)silicate hydrate chemistry under equilibrium conditions. *Cement and Concrete Research*, 68:83–93, 2015.

[228] Donald E. MacPhee, Karen Luke, Fred P Glasser, and Eric E Lachowski. Solubility and aging of calcium silicate hydrates in alkaline solutions at 25°C. *Journal of American Ceramic Society*, 72(4):646–654, 1989.

[229] David Rothstein, Jeffrey J Thomas, Bruce J Christensen, and Hamlin M Jennings. Solubility behavior of Ca-, S-, Al-, and Si-bearing solid phases in Portland cement pore solutions as a function of hydration time. *Cement and Concrete Research*, 32:1663–1671, 2002.

[230] Aditya Kumar, Shashank Bishnoi, and Karen L. Scrivener. Modelling early age hydration kinetics of alite. *Cement and Concrete Research*, 42(7):903–918, 2012.

[231] Gartner, Fulvio J Tang, and Stuart J Weiss. Saturation factors for calcium hydroxide and calcium sulfates in fresh Portland cement pastes. *Journal of the American Ceramic Society*, 68(12):667–673, 1985.

[232] G. Plusquellec, M. R. Geiker, J. Lindgård, J. Duchesne, B. Fournier, and K. De Weerdt. Determination of the pH and the free alkali metal content in the pore solution of concrete: Review and experimental comparison. *Cement and Concrete Research*, 96:13–26, 2017.

[233] P Debye and E Huckel. Zur Theorie der Elektrolyte. *Z. Phys.*, 24:185–206, 1923.

[234] Margaret Robson Wright. Chapter 10: Concepts and Theory of Non-Ideality. In *An Introduction to Aqueous Electrolyte Solutions*, pages 349–420. Wiley, 2007.

[235] Joseph F Zemaitis, Diane M Clark, Marshall Rafal, and Noel C Scrivner. *Handbook of Aqueous Electrolyte Thermodynamics*. 1986.

[236] Max Born. Volumen und hydratationswärme der ionen. *Zeitschrift für Physik*, 1(1):45–48, 1920.

[237] Niels Bjerrum. Neuere Anschauungen über Elektrolyte. *Berichte der deutschen chemischen Gesellschaft*, 62(5):1091–1103, 1929.

[238] C W Davies. *Ion Association*. Butterworth and Co, 1962.

[239] Alfred H. Truesdell and Blair F. Jones. WATEQ: A computer program for calculating chemical equilibria of natural waters. *Jour. Research US Geol. Survey*, 2(2):233–248, 1974.

[240] Kenneth S. Pitzer. Thermodynamics of electrolytes. I. Theoretical basis and general equations. *Journal of Physical Chemistry*, 77(2):268–277, 1973.

[241] R P Buck, S Rondini, A K Covington, F G K Baucke, C M A Brett, M J T Milton, T Mussini, R Naumann, K W Pratt, P Spitzer, and G S Wilson. Measurement of pH: Definition, Standards, and Procedures (IUPAC Recommendations 2002). *Pure and Applied Chemistry*, 74(11):2169–2200, 2002.

[242] By A K Covington and J E Prue. Precise measurements with the glass electrode. Part I. The cell: glass electrode HCl AgCl Ag. *Journal of the Chemical Society*, pages 3696–3700, 1955.

[243] Duncan A. MacInnes and Donald Belcher. A Durable Glass Electrode. *Industrial & Engineering Chemistry Analytical Edition*, 5(3):199–200, 1933.

[244] Friedrich Kohlrausch. Ueber das leitungsvermögen einiger electrolyte in äusserst verdünnter wässeriger lösung. *Annalen der Physik*, 262(10):161–226, 1885.

[245] Takashi Kakiuchi. Salt bridge in electroanalytical chemistry: Past, present, and future. *Journal of Solid State Electrochemistry*, 15(7-8):1661–1671, 2011.

[246] R G Picknett. Liquid junction potential between dilute electrolytes and saturated potassium chloride. *Transactions of the Faraday Society*, 64:1059–1069, 1968.

[247] John Bagg. Computer calculation of liquid-junction potentials - III. temperature-dependence of junction potentials. *Electrochimica Acta*, 37(4):719–723, 1992.

[248] M Cremer. Uber die ursache der elektromotorischen eigenschaften der gewebe zugleich ein beitrag zur lehre von den polyphasischen elektrolytketten. *Z Biol*, 47:562–608, 1906.

[249] Douglas A Skoog and Donald M West. *Fundamentals of Analytical Chemistry*. 3rd edition, 1976.

[250] B. P. Nicolsky, M. M. Shultz, A. A. Belijustin, and A. A. Lev. Chapter 6: Ion exchange theory of the glass electrodes. In G Eisenman, editor, *Glass Electrodes for Hydrogen and other cations*, pages 174–222. 1967.

[251] F. G.K. Baucke. The modern understanding of the glass electrode response. *Fresenius' Journal of Analytical Chemistry*, 349(8-9):582–596, 1994.

[252] K. L. Cheng. Capacitor theory for nonfaradaic potentiometry. *Microchemical Journal*, 42:5–24, 1990.

[253] Roger G. Bates. Determination of pH. page 365. Wiley, New York, 2nd edition, 1973.

[254] Károly Oláh. On the theory of the alkaline error of the glass electrode. *Periodica Polytechnica Chemical Engineering*, 4(2):141–156, 1960.

[255] B. P. Nicolsky. Theory of the glass electrode. I. *Zh Fis Khim*, 10:495, 1937.

[256] Andrew D Wiesner, Lynn E Katz, and Chia-chen Chen. The impact of ionic strength and background electrolyte on pH measurements in metal ion adsorption experiments. *Journal of Colloid and Interface Science*, 301:329–332, 2006.

[257] J. Schott, O. S. Pokrovsky, and E. H. Oelkers. The link between mineral dissolution/precipitation kinetics and solution chemistry. *Reviews in Mineralogy and Geochemistry*, 70(1):207–258, 2009.

[258] Eric H. Oelkers, Jacques Schott, and Jean-Luc Devidal. The effect of aluminum, pH, and chemical affinity on the rates of aluminosilicate dissolution reactions. *Geochimica et Cosmochimica Acta*, 58(9):2011–2024, 1994.

[259] Isabel Baur, Peter Keller, Denis Mavrocordatos, Bernhard Wehrli, and C. Annette Johnson. Dissolution-precipitation behaviour of ettringite, monosulfate, and calcium silicate hydrate. *Cement and Concrete Research*, 34(2):341–348, 2004.

[260] A. Gabrisová, J. Havlica, and S. Sahu. Stability of calcium sulphoaluminate hydrates in water solutions with various pH values. *Cement and Concrete Research*, 21(6):1023–1027, 1991.

[261] Patrick Juilland, Emmanuel Gallucci, Robert Flatt, and Karen Scrivener. Dissolution theory applied to the induction period in alite hydration. *Cement and Concrete Research*, 40:831–844, 2010.

[262] John L. Provis, Peter Duxson, Grant C. Lukey, Frances Separovic, Waltraud M. Kriven, and Jannie S.J. Van Deventer. Modeling speciation in highly concentrated alkaline silicate solutions. *Industrial and Engineering Chemistry Research*, 44(23):8899–8908, 2005.

[263] H. Matsuyama and J. F. Young. Effects of pH on precipitation of quasi-crystalline calcium silicate hydrate in aqueous solution. *Advances in Cement Research*, 12(1):29–33, 2000.

[264] I. García Lodeiro, D.E. Macphee, A. Palomo, and A. Fernández-Jiménez. Effect of alkalis on fresh C–S–H gels. FTIR analysis. *Cement and Concrete Research*, 39(3):147–153, mar 2009.

[265] Barbara Lothenbach, Ellina Bernard, and Urs Mäder. Zeolite formation in the presence of cement hydrates and albite. *Physics and Chemistry of the Earth*, 99:77–94, 2017.

[266] K. L. Cheng and Da Ming Zhu. On calibration of pH meters. *Sensors*, 5(4-5):209–219, 2005.

[267] Thomas Poinot, Michael E. Laracy, Cecilio Aponte, Hamlin M. Jennings, John A. Ochsendorf, and Elsa A. Olivetti. Beneficial use of boiler ash in alkali-activated bricks. *Resources, Conservation and Recycling*, 128(September 2017):1–10, 2018.

[268] Stuart Licht. pH Measurement in Concentrated Alkaline Solutions. *Analytical Chemistry*, 57(2):514–519, 1985.

[269] Y. Marcus. Ionic radii in aqueous solutions. *Journal of Solution Chemistry*, 12(4):271–275, 1983.

[270] Malcolm Dole and B Z Wiener. The theory of the glass electrode. IV. Temperature studies of the glass electrode error. *Transactions of The Electrochemical Society*, 72(1):107–127, 1937.

[271] G.M. Anderson and D.A. Crerar. *Thermodynamics in Geochemistry*. Oxford University Press, 1993.

[272] Damien Daval, Roland Hellmann, Jérôme Corvisier, Delphine Tisserand, Isabelle Martinez, and François Guyot. Dissolution kinetics of diopside as a function of solution saturation state: Macroscopic measurements and implications for modeling of geological storage of CO2. *Geochimica et Cosmochimica Acta*, 74(9):2615–2633, 2010.

[273] Nadine M. Piatak, Robert R. Seal, and Jane M. Hammarstrom. Mineralogical and geochemical controls on the release of trace elements from slag produced by base- and precious-metal smelting at abandoned mine sites. *Applied Geochemistry*, 19(7):1039–1064, 2004.

[274] Yan Feng, Jakob Kero, Qixing Yang, Qiusong Chen, Fredrik Engström, Caisa Samuelsson, and Chongchong Qi. Mechanical activation of granulated copper slag and its influence on hydration heat and compressive strength of blended cement. *Materials*, 12(5), 2019.

[275] Anna H Kaksonen, Silja Särkijärvi, Esa Peuraniemi, Saku Junnikkala, Jaakko A Puhakka, and Olli H Tuovinen. Metal biorecovery in acid solutions from a copper smelter slag. *Hydrometallurgy*, 168:135–140, 2016.

[276] Zongliang Zuo, Qingbo Yu, Siyi Luo, Jingkui Zhang, and Enze Zhou. Effects of CaO on two-step reduction characteristics of copper slag using biochar as reducer: thermodynamic and kinetics. *Energy and Fuels*, 34:491500, 2020.

[277] Paivi Kinnunen, Jarno Makinen, Marja Salo, Ratana Soth, and Konstantinos Komnitsas. Efficiency of chemical and biological leaching of copper slag for the recovery of metals and valorisation of the leach residue as raw material in. *Minerals*, 10(654), 2020.

[278] Mohammad M. Ali, Satish K. Agarwal, and Ashwani Pahuja. Potentials of copper slag utilisation in the manufacture of ordinary Portland cement. *Advances in Cement Research*, 25(4):208–216, 2013.

[279] A. M. Álvarez-Valero, R. Pérez-López, J. Matos, M. A. Capitán, J. M. Nieto, R. Sáez, J. Delgado, and M. Caraballo. Potential environmental impact at São Domingos mining district (Iberian Pyrite Belt, SW Iberian Peninsula): Evidence from a chemical and mineralogical characterization. *Environmental Geology*, 55(8):1797–1809, 2008.

[280] Jakub Kierczak and Anna Pietranik. Mineralogy and composition of historical Cu slags from the rudawy janowickie mountains, Southwestern Poland. *Canadian Mineralogist*, 49(5):1281–1296, 2011.

[281] Michael B. Parsons, Dennis K. Bird, Marco T. Einaudi, and Charles N. Alpers. Geochemical and mineralogical controls on trace element release from the Penn Mine base-metal slag dump, California. *Applied Geochemistry*, 16(14):1567–1593, 2001.

[282] L Rosado, C Morais, A E Candeias, A P Pinto, F Guimaraes, and J Mirao. Weathering of S. Domingos (Iberian Pyritic Belt) abandoned mine slags. *Mineralogical Magazine*, 72(1):489–494, 2008.

[283] A V Tatarinov. Metallurgical slags with spinifex textures. *Geochemistry International*, 40(11):1075–1082, 2002.

[284] Perrine Chaurand, Jerome Rose, Luca Olivi, Jean-louis Hazemann, and Olivier Proux. Environmental impacts of steel slag reused in road construction: A crystallographic and molecular (XANES) approach. *Journal of Hazardous Materials*, 139:537–542, 2007.

[285] Chandra Sekhar Gahan, Maria Lucelinda Cunha, and Åke Sandström. Comparative study on different steel slags as neutralising agent in bioleaching. *Hydrometallurgy*, 95(3-4):190–197, 2009.

[286] Laura A. Wendling, Monique T. Binet, Zheng Yuan, Francesca Gissi, Darren J. Koppel, and Merrin S. Adams. Geochemical and ecotoxicological assessment of iron- and steel-making slags for potential use in environmental applications. *Environmental Toxicology and Chemistry*, 32(11):2602–2610, 2013.

[287] P Mahieux, J Aubert, and G Escadeillas. Utilization of weathered basic oxygen furnace slag in the production of hydraulic road binders. *Construction and Building Materials*, 23:742–747, 2009.

[288] Alexander S. Brand and Jeffery R. Roesler. Steel furnace slag aggregate expansion and hardened concrete properties. *Cement and Concrete Composites*, 60:1–9, 2015.

[289] Zongwu Chen, Jun Xie, Yue Xiao, Juyong Chen, and Shaopeng Wu. Characteristics of bonding behavior between basic oxygen furnace slag and asphalt binder. *Construction and Building Materials*, 64:60–66, 2014.

[290] S Z Carvalho, F Vernilli, B Almeida, M D Oliveira, and S N Silva. Reducing environmental impacts: The use of basic oxygen furnace slag in portland cement. *Journal of Cleaner Production*, 172:385–390, 2018.

[291] Yi Yang, Yujia Min, and Young Shin Jun. Effects of Al/Si ordering on feldspar dissolution: Part II. The pH dependence of plagioclases' dissolution rates. *Geochimica et Cosmochimica Acta*, 126:595–613, 2014.

[292] Bao Lu, Caijun Shi, and Guihua Hou. Strength and microstructure of CO2 cured low-calcium clinker. *Construction and Building Materials*, 188:417–423, 2018.

[293] M Arius Bodor, R Afael M Santos, L Ubica Kriskova, J A N Elsen, M Aria Vlad, and T Van Gerven. Susceptibility of mineral phases of steel slags towards carbonation: mineralogical , morphological and chemical assessment. *European Journal of Mineralogy*, 25:533–549, 2013.

[294] Yongjie Xue, Shaopeng Wu, Haobo Hou, and Jin Zha. Experimental investigation of basic oxygen furnace slag used as aggregate in asphalt mixture. *Journal of Hazardous Materials*, 138:261–268, 2006.

[295] Julian Léon Stapper. Development of a sustainable cementitious binder based on incineration bottom ash and converter steel slag. 2020.

[296] Qiang Wang, Peiyu Yan, Jianwei Yang, and Bo Zhang. Influence of steel slag on mechanical properties and durability of concrete. *Construction and Building Materials*, 47:1414–1420, 2013.

[297] Fanghui Han, Zengqi Zhang, Dongmin Wang, and Peiyu Yan. Hydration heat evolution and kinetics of blended cement containing steel slag at different temperatures. *Thermochimica Acta*, 605:43–51, 2015.

[298] Carla Navarro, Mario Díaz, María A Villa García, and S Page. Physico-chemical Characterization of Steel Slag. Study of its Behaviour under Simulated Environmental Conditions. 44(14):1–13, 2010.

[299] Milena Morone, Giulia Costa, Alessandra Polettini, Raffaella Pomi, and Renato Baciocchi. Valorization of steel slag by a combined carbonation and granulation treatment. *Minerals Engineering*, 59:82–90, 2014.

[300] Alessandra Polettini, Raffaella Pomi, and Alessio Stramazzo. CO2 sequestration through aqueous accelerated carbonation of BOF slag: A factorial study of parameters effects. *Journal of Environmental Management*, 167:185–195, 2016.

[301] Yung Chin Ding, Ta Wui Cheng, Ping Chun Liu, and Wei Hao Lee. Study on the treatment of BOF slag to replace fine aggregate in concrete. *Construction and Building Materials*, 146:644–651, 2017.

[302] Jia-chen Xi, Xiao-dong Xiang, and Can-hua Li. Process Improvement on the Gradation Uniformity of Steel Slag Asphalt Concrete Aggregate. *Procedia Environmental Sciences*, 31:627–634, 2016.

[303] E. E. Chang, An Chia Chiu, Shu Yuan Pan, Yi Hung Chen, Chung Sung Tan, and Pen Chi Chiang. Carbonation of basic oxygen furnace slag with metalworking wastewater in a slurry reactor. *International Journal of Greenhouse Gas Control*, 12:382–389, 2013.

[304] M P Luxan, R Sotolongo, F Dorrego, and E Herrero. Characteristics of the slags produced in the fusion of scrap steel by electric arc furnace. *Cement and Concrete Research*, 30:517–519, 2000.

[305] Amaia Santamaría, Eduardo Rojí, Marta Skaf, Ignacio Marcos, and Javier J. González. The use of steelmaking slags and fly ash in structural mortars. *Construction and Building Materials*, 106:364–373, 2016.

[306] Ritwik Sarkar, Nar Singh, and Swapan Kumar Das. Utilization of steel melting electric arc furnace slag for development of vitreous ceramic tiles. *Bulletin of Materials Science*, 33(3):293–298, 2010.

[307] Lime Jay Sern, Chee Ban Cheah, and Mahyuddin B. Ramli. The setting behavior, mechanical properties and drying shrinkage of ternary blended concrete containing granite quarry dust and processed steel slag aggregate. *Construction and Building Materials*, 215:447–461, 2019.

[308] Carlo Pellegrino, Paolo Cavagnis, Flora Faleschini, and Katya Brunelli. Properties of concretes with black/oxidizing electric arc furnace slag aggregate. *Cement and Concrete Composites*, 37(1):232–240, 2013.

[309] R. Baciocchi, G. Costa, M. Di Gianfilippo, A. Polettini, R. Pomi, and A. Stramazzo. Thin-film versus slurry-phase carbonation of steel slag: CO2 uptake and effects on mineralogy. *Journal of Hazardous Materials*, 283:302–313, 2015.

[310] Maria Chiara Bignozzi, Stefania Manzi, Isabella Lancellotti, Elie Kamseu, Luisa Barbieri, and Cristina Leonelli. Mix-design and characterization of alkali activated materials based on metakaolin and ladle slag. *Applied Clay Science*, 73:78–85, 2013.

[311] Lubica Kriskova, Yiannis Pontikes, Ozlem Cizer, Gilles Mertens, Wout Veulemans, Daneel Geysen, Peter Tom Jones, Lucie Vandewalle, Koen Van Balen, and Bart Blanpain. Effect of mechanical activation on the hydraulic properties of stainless steel slags. *Cement and Concrete Research*, 42(6):778–788, 2012.

[312] Ankica Radenovic, Malina Jadranka, and Tahir Sofili. Characterization of ladle furnace slag from carbon steel production as a potential adsorbent. *Advances in Materials Science and Engineering*, (198240), 2013.

[313] J. Vlcek, V. Tomkova, H. Ovcacikova, F. Ovcacik, M. Topinkova, and V. Matejka. Slags from steel production: Properties and their utilization. *Metalurgija*, 52(3):329–333, 2013.

[314] Juan M. Manso, Milagros Losañez, Juan A. Polanco, and Javier J. Gonzalez. Ladle Furnace Slag in Construction. *Journal of Materials in Civil Engineering*, 17(5):513–518, 2005.